

12-2003

A Mass Balance Study of the West Antarctic Ice Sheet

Vandy Blue Spikes

Follow this and additional works at: <http://digitalcommons.library.umaine.edu/etd>



Part of the [Geology Commons](#), and the [Glaciology Commons](#)

Recommended Citation

Spikes, Vandy Blue, "A Mass Balance Study of the West Antarctic Ice Sheet" (2003). *Electronic Theses and Dissertations*. 595.
<http://digitalcommons.library.umaine.edu/etd/595>

This Open-Access Dissertation is brought to you for free and open access by DigitalCommons@UMaine. It has been accepted for inclusion in Electronic Theses and Dissertations by an authorized administrator of DigitalCommons@UMaine.

**A MASS BALANCE STUDY OF THE
WEST ANTARCTIC ICE SHEET**

By

Vandy Blue Spikes

B.S. Emporia State University, 1997

M.S. The Ohio State University, 2000

A THESIS

Submitted in Partial Fulfillment of the

Requirements for the Degree of

Doctor of Philosophy

(in Geological Sciences)

The Graduate School

The University of Maine

December, 2003

Advisory Committee:

Gordon Hamilton, Research Assistant Professor of the Climate
Change Institute, Advisor

Steven Arcone, U.S. Army ERDC CRREL

James Fastook, Professor of Computer Science and the Climate
Change Institute

Peter Koons, Assistant Professor of Earth Sciences

Karl Kreutz, Assistant Professor of Earth Sciences and the Climate
Change Institute

© 2003 Vandy Blue Spikes
All Rights Reserved

**A MASS BALANCE STUDY OF THE
WEST ANTARCTIC ICE SHEET**

By Vandy Blue Spikes

Thesis Advisor: Dr. Gordon Hamilton

An Abstract of the Thesis Presented
in Partial Fulfillment of the Requirements for the
Degree of Doctor of Philosophy
(in Geological Sciences)
December, 2003

The present state of the West Antarctic ice sheet (WAIS) is a prime concern of science, but its large size and remote location have limited the amount of reliable data that are available for mass balance calculations. The spatial pattern of mass balance for a 100-km² portion of the WAIS is estimated by calculating the residual flux of ice through 1-km grid cells organized into a geographical information system (GIS). The input data used for this estimate include continent-scale compilations of ice thickness and snow accumulation rate measurements, and ground-based measurements of snow accumulation rate and ice velocity. The calculation was performed using different combinations of input data so that error sources could be identified. The largest sources of error were associated with the continent-scale compilations of accumulation rate and ice thickness. These errors are greatly reduced when using snow accumulation rates derived from ground-penetrating radar (GPR) surveys. The best results, which agree with two previous estimates, suggest that this area is nearly in balance. Results also indicate that the mass balance varies within this 100-km² grid. In some portions of the grid, local variations in mass balance correspond with measured changes in ice velocity and snow accumulation

rate. In other parts of the grid, the apparent spatial variability is attributed to errors in the ice thickness data.

The results show that the demonstrated accuracy and spatial resolution of this high-resolution sampling approach are needed to understand the response of the entire West Antarctic ice sheet to recent changes in climate. However, the accuracy of the data compilations discussed above are examined using continuous, simultaneously recorded, ground-based measurements of ice-sheet surface topography, ice thickness, and snow accumulation rate that extend for hundreds of km beyond the grid at Byrd Station. Results from these analyses suggest that each of the compilations have larger errors than previously reported and therefore need to be improved before they are incorporated into estimates of WAIS mass balance.

DEDICATION

In memory of my first graduate advisor, Dr. Ian Whillans,
who inspired this research.

ACKNOWLEDGEMENTS

I would like to thank Dr. Gordon Hamilton for his encouragement, assistance, guidance, and friendship over the past several years. I would also like to give special thanks to Dr. Steven Arcone for helping me to better understand radar geophysics, and for his thoughtful comments regarding this dissertation. Thanks also to Dr. James Fastook, Dr. Karl Kreutz, and Dr. Peter Koons for serving on my advisory committee. I must also thank my family for once again supporting my efforts, and for constantly reminding me that hard work and diligence are the keys to success.

The funding for this research was provided through a grant from the National Science Foundation (OPP-0196441) to Gordon Hamilton. My personal funds (tuition, stipend, etc.) were provided through a National Aeronautics and Space Administration Earth System Science Fellowship (NGT5-30426).

TABLE OF CONTENTS

DEDICATION.....	iii
ACKNOWLEDGEMENTS.....	iv
LIST OF TABLES.....	viii
LIST OF FIGURES.....	ix

Chapter

1. INTRODUCTION.....	1
2. REVIEW OF METHODS FOR ESTIMATING ICE SHEET	
MASS BALANCE.....	6
2.1 Submergence Velocity Stations.....	6
2.2 Repeat Altimeter Measurements.....	8
2.3 Flux Calculations Along Flow Lines.....	10
2.4 Flux Calculations for Drainage Basins.....	11
2.5 Flux Calculations for Grid Cells.....	12
2.6 Choosing a Mass Balance Approach.....	14
3. THE GIS APPROACH.....	15
3.1 The Geographical Information System.....	15
3.2 The Residual Flux Calculation.....	16
4. LAYERS IN THE GIS.....	19
4.1 Introduction.....	19
4.2 Ice Sheet Surface Topography.....	22

4.2.1 Static Positioning of GPS Reference Station.....	23
4.2.2 Kinematic Positioning Along Survey Lines.....	26
4.2.3 High-resolution Mapping of Three-dimensional Grids.....	27
4.2.4 Evaluation of the RAMP DEM.....	30
4.2.5 Discussion.....	37
4.2.6 Conclusions.....	38
4.3 Ice Thickness.....	38
4.3.1 Maps of Bedrock Topography and Ice Thickness.....	39
4.3.2 Evaluation of BEDMAP.....	42
4.3.3 Conclusions.....	43
4.4 Snow Accumulation Rates.....	46
4.4.1 Isochronal Nature of Continuous Radar Reflections.....	47
4.4.1.1 Simplifying the Radar Pulse.....	48
4.4.1.2 Defining the Depth-age Relationship.....	50
4.4.1.3 Tests of Isochronal Accuracy.....	52
4.4.2 Accumulation Rates from GPR Profiling.....	53
4.4.2.1 Continuous Versus Point Measurements.....	55
4.4.2.2 Topographic Influence.....	55
4.4.2.3 Resolving Climatic Influence.....	58
4.4.2.4 Accumulation Rates Near Byrd Station.....	61
4.4.3 Tests of a Widely Used Compilation of Antarctic Accumulation Rates.....	67
4.4.4 Conclusions.....	70

4.5 Ice Velocity.....	71
4.5.1 Surface Velocities at Byrd Station.....	72
4.5.2 Depth-averaged Velocities at Byrd Station.....	75
5. ESTIMATING ICE SHEET MASS BALANCE FOR THE BYRD STATION GRID.....	79
5.1 Results.....	79
5.2 Error Estimates.....	81
5.3 Discussion.....	84
5.4 Applying the Uncertainties to the West Antarctic Ice Sheet.....	85
6. CONCLUSIONS.....	87
REFERENCES.....	90
BIOGRAPHY OF THE AUTHOR.....	98

LIST OF TABLES

Table 2.1 Mass balance results from the numbered SV stations in Figure 2.1	8
Table 4.1 Correlation between along-track gradients in accumulation rate and surface slope.....	58
Table 4.2 Multi-decadal accumulation rates expressed as the 100-km mean for each interval, and the percent difference between the interval mean and the long-term regional mean.....	60

LIST OF FIGURES

Figure 2.1 Shaded-relief map of Antarctica showing the locations where accurate estimates of mass balance are available.....	7
Figure 3.1 Schematic of the flux, Q , through a GIS grid cell at grid point (x,y)	15
Figure 3.2 Diagram of a column through the ice thickness showing how mass flux can change with depth.....	18
Figure 4.1 Map of US ITASE traverse routes superimposed on surface contours created using a 1-km version of the RAMP DEM.....	20
Figure 4.2 Example of the daily trend in the vertical coordinate for the Byrd base station during the 2002-2003 field season.....	25
Figure 4.3 Tracks of GPS surveys around Byrd Station and 02-3.....	28
Figure 4.4 Interpolated contours of ice sheet surface topography around Byrd Station and 02-3.....	29
Figure 4.5 Distribution of uncertainties in the elevation component of GPS positions around Byrd Station and 02-3.....	30
Figure 4.6 Differences between GPS and RAMP DEM along two-dimensional profiles.....	33
Figure 4.7 Differences between GPS and RAMP DEM in the vicinity of Byrd Station.....	36
Figure 4.8 Map of ice sheet thickness for West Antarctica and the South Pole region.....	40

Figure 4.9 Map of bedrock topography for West Antarctica and portions of East Antarctica	41
Figure 4.10 Maps of bedrock topography and ice thickness for the 100-km ² grid centered on Byrd Station	42
Figure 4.11 WAIS cross-section between Byrd Station and 01-5	44
Figure 4.12 WAIS cross-section along profile a' – a'' in Figures 4.10 and 4.11	45
Figure 4.13 Location maps and ice core data	49
Figure 4.14 Radar data collected between US ITASE sites 00-4 and 00-5	51
Figure 4.15 Spatial variability of accumulation rates from ice cores and GPR profiling	56
Figure 4.16 Temporal variability in accumulation rates from ice cores and GPR profiling	59
Figure 4.17 Geophysical surveys conducted within the 100-km ² grid centered on Byrd Station	62
Figure 4.18 Radar profile collected along the three-dimensional survey lines around Byrd Station	63
Figure 4.19 Snow accumulation rates from three-dimensional GPR profiling around Byrd Station	65
Figure 4.20 Map of accumulation rates for the 100-km ² grid centered on Byrd Station	66
Figure 4.21 West Antarctic accumulation rates from the Vaughan <i>et al.</i> (1999a) compilation	68

Figure 4.22 Test of the Vaughan <i>et al.</i> (1999a) compilation near Byrd Station.....	69
Figure 4.23 Contoured map of ice surface speed for the 100-km ² grid centered on Byrd Station.....	74
Figure 4.24 The horizontal velocity profile at Byrd Station.....	77
Figure 4.25 Contoured maps of bed and depth-averaged velocities for the 100-km ² grid centered on Byrd Station.....	78
Figure 5.1 Calculated mass balance of the 100-km ² grid centered on Byrd Station.....	80
Figure 5.2 Mass balance variables used to interpret thickness change estimates within the 100-km ² grid centered on Byrd Station.....	83

Chapter 1

INTRODUCTION

Ice sheets play an important role in Earth's climate system and water budget. Ice sheets influence and respond to changes in climate by modification of atmospheric circulation and through albedo dynamics. Sea level is modulated in part by the storage and release of water from ice sheets. The most recent report from the Intergovernmental Panel on Climate Change (IPCC; Church *et al.*, 2001) shows that globally averaged atmospheric temperatures on Earth are increasing and in response, sea level is rising at a rate of 1 to 2 mm a⁻¹. This is due primarily to expansion of sea water, which may account for half of the current rate of sea level rise (s.l.r.), and melting of glaciers, ice caps, and ice sheets, whose contributions are still inadequately understood (Church *et al.*, 2001). The response of an ice sheet to climate changes and its contribution to the current rate of global sea level rise can be assessed by determining whether the ice sheet is gaining or losing mass.

Approaches used to calculate the net mass balance of an ice mass, defined as the rate at which the volume of that mass is changing, range from direct measurements using submergence velocity (SV) stations (Hamilton *et al.*, 1998) and repeat altimeter surveys (e.g. Wingham *et al.*, 1998; Spikes *et al.*, 2003a,b), to regional-scale mass flux calculations based on ground (e.g. Whillans, 1977; Whillans and Bindschadler, 1988; Bindschadler *et al.*, 1993), airborne (e.g. Joughin *et al.*, 1999; Shabtaie and Bentley, 1987), and satellite (e.g. Joughin and Tulaczyk, 2002; Rignot and Thomas, 2002)

measurements. The uncertainty associated with each of these approaches varies according to the quality of the input data. SV stations rely on precise ground-based measurements and therefore provide results with small uncertainties that can be unambiguously interpreted as long-term changes, but these are point measurements and are limited in spatial extent (Hamilton *et al.*, 1998). Repeat altimeter measurements of surface elevation over large regions can provide reliable results of short-term changes (Krabill *et al.*, 2000), but spatial and temporal accumulation variability complicates their interpretation (McConnell *et al.*, 2000; Spikes *et al.*, 2003a). Mass flux calculations provide spatially extensive estimates of mass balance (Shabtaie and Bentley, 1987; Joughin and Tulaczyk, 2002; Rignot and Thomas, 2002), but these studies incorporate continent-scale compilations of ice thickness (e.g. Lythe *et al.*, 2000) and accumulation rate (e.g. Vaughan *et al.*, 1999a; Giovinetto and Zwally, 2000), which can contribute large uncertainties.

According to recent estimates, the ice sheets in Greenland and Antarctica are both slowly losing mass. The estimates for Greenland (Krabill *et al.*, 1999; Krabill *et al.*, 2000) were derived from repeat altimeter measurements of surface elevations and showed that the ice sheet margins are thinning while the central portion is in balance. Overall, the Greenland ice sheet was reported to be contributing $\sim 0.13 \text{ mm a}^{-1}$ or 7 – 13% of the current rate of sea level rise (Krabill *et al.*, 2000). A re-analysis by McConnell *et al.* (2000) has since shown that much of the observed change in Greenland can be attributed to short-term (~ 10 years) changes in snowfall rates. Estimates for the grounded portion of the Antarctic ice sheet also suggest rapid thinning near the margins, which is balanced to some degree by thickening in the ice sheet interior. Repeat altimeter studies have shown that the entire ice sheet is slowly thinning ($< 0.01 \text{ m a}^{-1}$) (Wingham *et al.*, 1998), while

fast-moving outlet glaciers and ice streams are rapidly thinning ($>1 \text{ m a}^{-1}$) (Shepherd *et al.*, 2002; Spikes *et al.*, 2003a). Results from basin-wide flux calculations based largely on ice velocities measured using synthetic aperture radar (SAR) interferometry, suggest thickening in the west (Joughin and Tulaczyk, 2002) and possibly slow thinning overall (Rignot and Thomas, 2002). Although there is general agreement among these estimates, the data used to calculate each of these results were collected over short time intervals. Therefore, these results may represent changes that do not indicate long-term responses to changes in climate (Kostecka and Whillans, 1988; Van der Veen, 1993; Van der Veen and Bolzan, 1999; Wingham *et al.*, 1998; Wingham, 2000; McConnell *et al.*, 2000; Cuffey, 2001).

In recent decades, a large amount of interest has been focused on the West Antarctic ice sheet (WAIS). A key concern is that a large percentage of the grounded ice mass is already below sea level, making it especially sensitive to small increases in ocean heights (Thomas, 1979). Two recent studies by Bindschadler *et al.* (2003) and Anandakrishnan *et al.* (2003) suggest that oceanic tidal oscillations control the daily ice motions of several West Antarctic ice streams. These results appear to confirm that this ice sheet is inherently unstable and could respond catastrophically if sea level continues to rise. If this ice sheet were to completely disintegrate, global sea level would rise by 5 to 6 m (Alley and Bindschadler, 2001). It is therefore important to understand the current configuration and mass balance changes underway in West Antarctica. The mass balance of the WAIS is the focus of this dissertation.

The objective of this thesis is to show that local sampling of mass balance based on intensive ground-based measurements produces only a small uncertainty, reveals

larger uncertainties in more spatially extensive approaches, and is therefore a viable way to approach the mass balance of West Antarctica. The approach requires the calculation of the residual flux through columns of ice that extend from the surface to the bed, and which are commonly referenced to a stationary grid. The coordinates and spacing of the stationary grid define a geographical information system (GIS). The necessary variables of ice thickness, ice velocity, and snow accumulation rate are directly measured to determine residual flux. A fourth characteristic that is important for interpretations of mass balance results is ice-sheet surface topography. Each of these boundary conditions is evaluated in this dissertation.

Each of these mass balance characteristics is known to vary spatially, which can contribute large uncertainties to mass balance estimates using the GIS approach. With the exception of ice velocity, continent-scale compilations of each of these characteristics are currently available for Antarctica. However, the ability of these compilations to accurately portray the spatial variability of each of these characteristics is unclear. For this reason, much of this dissertation is devoted to the presentation and discussion of ground-based measurements of each of these variables recorded throughout West Antarctica. The global positioning system (GPS) was used to map ice-sheet surface topography, high-frequency ground-penetrating radar (GPR) was used to track stratigraphic layers which are coupled with ice core density and depth-age profiles to calculate historical snow accumulation rates, and 3-MHz radar soundings were used to measure ice thickness. In addition, submergence velocity stations were installed at each of the ice core sites to provide ice velocities and direct estimates of mass balance. Overall, these data cover ~5000 km (linear distance) of the WAIS.

These ground-based data are used to characterize the spatial variability of surface elevations, ice thicknesses, and snow accumulation rates, and they are used to determine the accuracy and spatial resolution of the leading continent-scale compilations of ice surface topography (Liu *et al.*, 1999), ice thickness (Lythe *et al.*, 2000), and snow accumulation rate (Vaughan *et al.*, 1999a). The results of these analyses reveal a high degree of spatial variability in each of the measured variables, and that this variability is not present in the compilations. As a result, each of these compilations was found to have large uncertainties. Therefore, the GIS approach is not applied to all of West Antarctica. Instead, it is tested and applied to a small portion of this ice sheet where sufficiently accurate data are available.

This dissertation is presented in the following order. Chapter 2 reviews different approaches for calculating ice sheet mass balance and summarizes recent results. Chapter 3 describes the GIS approach to estimating mass balance used in this dissertation. In Chapter 4, each GIS layer is described in detail. In Chapter 5, the GIS approach is tested on a 100-km² grid centered on Byrd Station, West Antarctica using the new data presented in Chapter 4. The conclusions and a summary of results are presented in Chapter 6.

Chapter 2

REVIEW OF METHODS FOR ESTIMATING ICE SHEET MASS BALANCE

There are several techniques for estimating the mass balance of ice sheets. The most commonly used methods are described in detail in this chapter. Recent results from each of these methods are also discussed.

2.1 Submergence Velocity Stations

Submergence velocity (SV) stations provide point estimates of mass balance that have small uncertainties and can be unambiguously interpreted as long-term changes (e.g. Hulbe and Whillans, 1994; Hamilton *et al.*, 1998). For mass balance, the downward motion of the ice sheet is balanced by snow accumulation at the surface. The technique entails comparison of the vertical component of ice velocity, derived from repeat GPS surveys of markers, with the local long term accumulation rate, derived from ice core stratigraphy. Small adjustments are made for firm compaction beneath the markers, using density profiles derived from ice cores, and along-slope flow, using surface topography from differential kinematic GPS surveys. Results from SV stations are reported as the water equivalent (w.e.) net thickness change per year.

While SV stations provide the most reliable mass balance estimates on ice sheets, their results are spatially limited and logistical constraints limit the number of sites where the technique can be applied. To date, 35 SV stations have been installed on the Antarctic

ice sheet (Figure 2.1), although many of these stations have not yet been resurveyed. The mass balance results presented in Table 2.1 are from SV stations in West Antarctica, with the exception of South Pole, which is in East Antarctica.

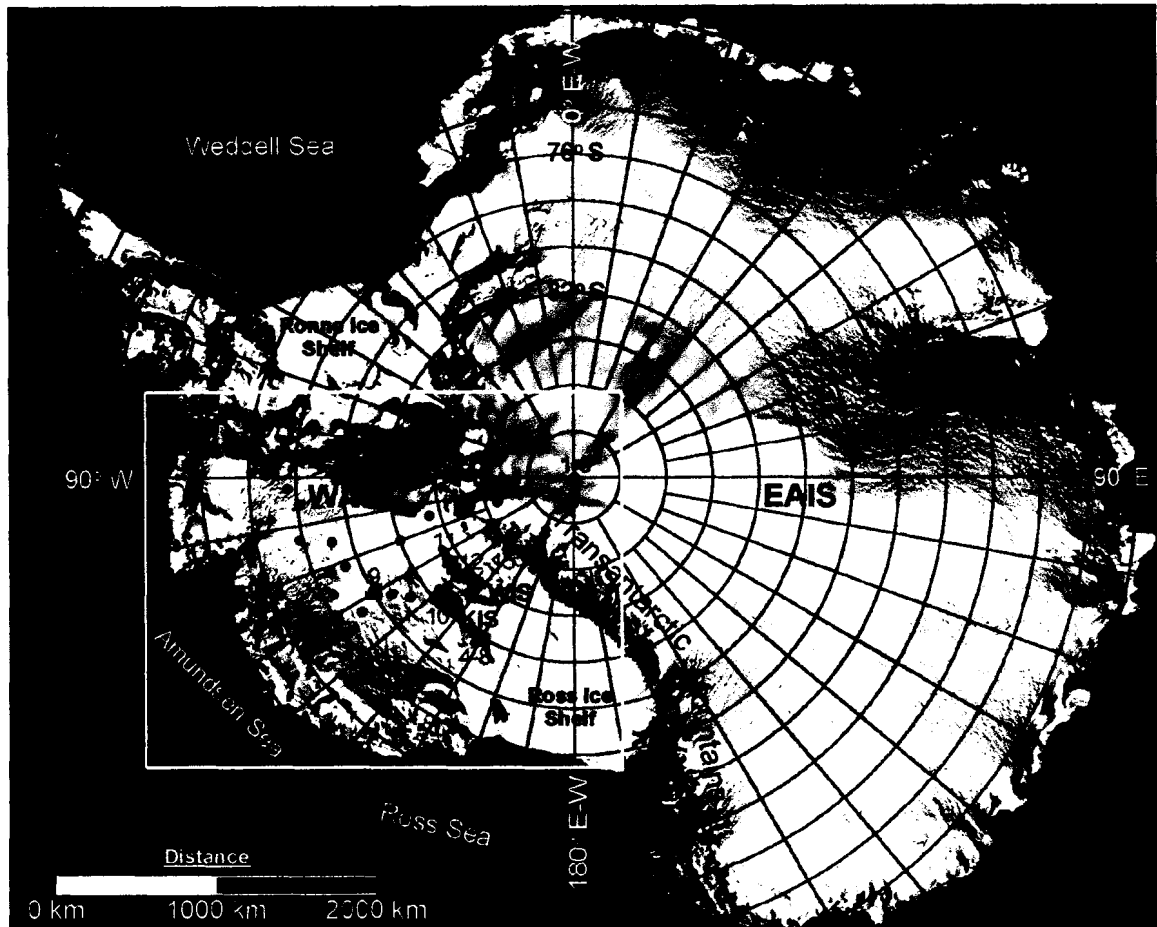


Figure 2.1 Shaded-relief map of Antarctica (5-km version; Liu *et al.*, 1999) showing the locations where accurate estimates of mass balance are available. The white box indicates the portions of Antarctica considered in this dissertation. Red circles indicate SV stations (Hamilton *et al.*, 1998; Spikes *et al.*, 2003a). Results from numbered SV stations are presented in Table 2.1 Blue lines indicate airborne laser altimeter surveys over Whillans (WIS) and Kamb (KIS) Ice Streams (Spikes *et al.*, 2003a,b) (Chapter 2.2). Green rectangles indicate GLAS CV sites (Spikes and Hamilton, 2003) (Chapters 2.2 and 4.2.3). Yellow line indicates the Byrd surface strain network (BSSN) (Whillans, 1977, 1979) (Chapters 2.3 and 4.5.1).

Table 2.1 Mass balance results from the numbered SV stations shown in Figure 2.1. Subscripts indicate the source of information as follows: ¹unpublished data from G.S. Hamilton; ²Hamilton, 2002; ³Hamilton *et al.*, 1998; ⁴Spikes *et al.*, 2003a.

Location (SV station name) ^{reference}	Accumulation Rate (m a ⁻¹ w.e.)	Ice Velocity (m a ⁻¹)	Mass Balance (m a ⁻¹ w.e.)
1. South Pole (SP) ¹	0.08	10.14	+0.018 ± 0.02
2. South Pole (SB) ¹	0.10	9.69	+0.021 ± 0.018
3. South Pole (Farfield) ¹	0.09	9.58	+0.032 ± 0.024
4. Siple Dome (A) ²	0.16	8.25	-0.047 ± 0.026
5. Siple Dome (C) ²	0.14	1.34	-0.021 ± 0.033
6. Siple Dome (E) ²	0.12	0.38	-0.014 ± 0.023
7. Siple Dome (F) ²	0.12	0.05	-0.016 ± 0.023
8. Siple Dome (H) ²	0.09	1.48	-0.023 ± 0.024
9. Byrd Station (Byrd) ³	0.11	11.83	-0.004 ± 0.022
10. Kamb IS (Up-C) ⁴	0.09	13.14	0.559 ± 0.019
11. Whillans IS (Catchment-B) ⁴	0.11	11.32	0.019 ± 0.021
12. Whillans IS (Up-B) ⁴	0.08	416.13	-1.316 ± 0.085
13. Unicorn (Dragon) ³	0.06	1.98	-0.096 ± 0.044
14. Engelhard IR (Snake) ¹	0.08	12.7	-0.189 ± 0.024
15. Engelhard IR (BBC) ¹	0.08	12.24	-0.164 ± 0.024

2.2 Repeat Altimeter Measurements

Repeat radar and laser altimeter measurements from satellites or aircraft can be used to track time changes in the elevation of ice sheet surfaces (e.g. Garvin and Williams, 1993; Krabill *et al.*, 1995; Csatho *et al.*, 1996; Wingham *et al.*, 1998; Krabill *et al.*, 1999, 2000; Christensen *et al.*, 2000; Zwally *et al.*, 2002; Spikes *et al.*, 2003a). Advantages of this remote sensing approach are spatial continuity and relatively small errors. A key issue with repeat altimetry is placing measurements of surface elevation change made over short timescales (~5 years) in the context of longer-term geophysical ice sheet behavior. Ice-sheet surface elevations change according to several processes: ice velocity changes (e.g. Whillans and Bindschadler, 1988; Joughin *et al.*, 1999; Price *et al.*,

2001); spatial and temporal variations in the rate of snowfall and firn densification (e.g. Kostecka and Whillans, 1988; Van der Veen, 1993; Wingham *et al.*, 1998; Van der Veen and Bolzan, 1999; McConnell *et al.*, 2000; Wingham, 2000; Cuffey, 2001); and vertical bedrock motions (e.g. James and Ivins, 1998). While the effects of bedrock motions and firn compaction are negligible in most cases ($< 0.01 \text{ m a}^{-1}$ each; James and Ivins, 1998; Wingham, 2000; Spikes *et al.*, 2003a), the effects of short-term changes of accumulation rate and velocity may contribute large uncertainties to mass balance estimates based on repeat radar and laser altimeter measurements (e.g. Van der Veen, 1993; Wingham *et al.*, 1998; Van der Veen and Bolzan, 1999; McConnell *et al.*, 2000; Cuffey, 2001; Spikes *et al.*, 2003a).

In West Antarctica, radar and laser altimeters have been used to measure elevation changes (Wingham *et al.*, 1998; Spikes *et al.*, 2003a). Using repeat satellite radar altimeter measurements, Wingham *et al.* (1998) found that the elevation of the West Antarctic ice sheet fell at an average rate of $0.035 \pm 0.05 \text{ m a}^{-1}$ during the period from 1992 to 1996, although much of this change was attributed to a possible decrease in snow accumulation over the past century. Shepherd *et al.* (2002) used satellite radar altimetry coupled with interferometry to show that the major drainage features feeding into the Amundsen Sea are thinning at an average rate of $0.09 \pm 0.02 \text{ m a}^{-1}$. Elevation changes measured with airborne laser altimetry demonstrated that portions of two Whillans Ice Stream (WIS was formerly known as Ice Stream B) tributaries (Figure 2.1) were thinning at average rates of 0.57 m a^{-1} (Whillans-1) and 0.64 m a^{-1} (Whillans-2) and Kamb Ice Stream (KIS was formerly known as Ice Stream C) was thickening at an average rate of 0.12 m a^{-1} over the period from 1997 to 1999 (Spikes *et al.*, 2003a).

The Geoscience Laser Altimeter System (GLAS), which is part of the National Aeronautics and Space Administration (NASA) Ice Cloud and Land Elevation Satellite (ICESat), is expected to provide a high-spatial resolution (70-m footprint) dataset of ice sheet surface elevations with unrivaled accuracy and spatial coverage (Zwally *et al.*, 2002). Over a 3-5 year period the satellite is also expected to measure changes in elevation that will be used to determine the mass balance of the Antarctic ice sheet. One of the goals of the research described here is to determine the accuracy of GLAS measurements using ground-based measurements of ice sheet surface topography, snow accumulation rates, and mass balance. ICESat was successfully launched on January 12, 2003, and elevation data will be released to the science community in late 2003 (Jay Zwally, pers. comm.)

2.3 Flux Calculations Along Flow Lines

The concept of mass continuity has been applied in many ice sheet studies (e.g. Thomas, 1976; Whillans, 1977; Kostecka and Whillans, 1988). The equation of continuity states that the time-rate of change of a volume element is balanced by a net movement into or out of the element (Paterson, 1994). For areas where ice velocity measurements are lacking but surface mass balance measurements are available, this concept can be used to calculate steady-state balance velocities. In areas where ice velocity and surface mass balance measurements are available, continuity can be used to calculate the rate of ice thickness change. Rates of ice thickness change are obtained by comparing measured surface velocities with calculated balance velocities along a flow line. Whillans (1977) used this approach to determine that the ice sheet at Byrd Station

was slowly thinning at a rate of 0.03 m a^{-1} . The Whillans (1977) study included measurements of surface velocity and accumulation data collected along the 162-km Byrd surface strain network (BSSN) (Figure 2.1) that started at the ice divide and ended at Byrd Station. Results from the Byrd SV station (Table 2.1) (Hamilton *et al.*, 1998) confirmed that this region is slowly thinning.

2.4 Flux Calculations for Drainage Basins

A widely used approach for calculating the mass balance of the WAIS involves flux calculations for entire drainage basins (Shabtaie and Bentley, 1987; Whillans and Bindshadler, 1988; Jacobs, 1992; Joughin and Tulaczyk, 2002; Rignot and Thomas, 2002). This approach compares mass input integrated throughout a catchment with the mass flux through a defined gate. The calculation requires estimates of accumulation rate, ice thickness, ice velocity, and catchment boundaries. A number of factors simplify this approach, including the use of an average accumulation rate for the entire catchment, assumption of zero flux through regions where there is no gate, and that ice thickness and ice velocity measurements are only necessary for points in the immediate vicinity of gates. To further simplify this calculation, fast-moving ice streams and outlet glaciers are typically used as gates, because at these locations ice flow is perpendicular to the gate and the depth-averaged velocity is approximately equal to the surface velocity. A limiting factor of this approach is that the spatial resolution is very low. For example, a basin that is in balance may be thickening at the divide and thinning at the margin, but this approach does not provide an opportunity to distinguish between these spatial contrasts.

Shabtaie and Bentley (1987) applied this calculation to the entire Ross Ice Stream region in West Antarctica. They found that the region was losing mass at a rate of 20 Gt a⁻¹ (360 Gt of water ~1 mm s.l.r). Using improved estimates of ice thickness, ice velocity, accumulation rate, and updated catchment boundaries, Joughin and Tulaczyk (2002) reevaluated the mass balance of this region, and found that it is gaining mass at an average rate of 26 Gt a⁻¹. A third study by Rignot and Thomas (2002) used the same technique to determine that other portions of West Antarctica were thinning rapidly. When combined, the Joughin and Tulaczyk (2002) and Rignot and Thomas (2002) results suggest that the WAIS is slowly losing mass at a rate of ~44 Gt a⁻¹.

2.5 Flux Calculations for Grid Cells

An alternative to catchment-scale studies is to calculate mass balance for small (1-5 km) grid cells (Bindschadler *et al.*, 1993; Joughin *et al.*, 1999). This high-resolution approach can reveal the spatial distribution of mass balance changes throughout a region and can be tuned to account for changes in flow style as well as convergence and divergence. The net mass balance for each grid cell is equal to the residual fluxes through each of the four vertical faces divided by the surface area (top) of each cell, plus the residual rate of accumulation/ablation for each grid cell. A drawback of this approach is that it is very sensitive to the quality of the input data because the relative changes in mass for each cell are small (typically on the order of 10⁸ kg a⁻¹) compared to flux of material that is passing through each cell (typically on the order of 10¹¹ kg a⁻¹). The required input data are ice thickness, ice velocity, net surface mass balance, and the rate of basal melting/accretion.

Using this approach, Bindschadler *et al.* (1993) and Joughin *et al.* (1999) estimated the mass balance of two different portions of the Siple Coast Ice Stream region. To derive an average thickening rate of $0.13 \pm 0.05 \text{ m a}^{-1}$ for the Whillans Ice Plain, Bindschadler *et al.* (1993) relied on widely spaced measurements of ice thickness, ice surface velocity, and accumulation rate and assumed that there was no change in velocity with depth and no flux through the ice/bed interface. The standard error for each of their grid cells is 6.7 m a^{-1} , which is roughly 15 times the average rate of change for each grid cell. Bindschadler *et al.* (1993) reduced the standard error of their grid cells to 0.22 m a^{-1} by applying a 31 km x 31 km running-average filter to their mass balance results.

Joughin *et al.* (1999) used the same approach, but incorporated regularly spaced measurements of ice thickness from airborne radar soundings and ice velocity from satellite-based synthetic aperture radar (SAR) interferometry. This study covered nearly the same area of KIS that was surveyed using airborne laser altimetry (Spikes *et al.*, 2003a), but misses the SV station on KIS (Table 2.1). Joughin *et al.* (1999) report a spatially-variable pattern of thickness change ranging from 0.0 to 0.7 m a^{-1} , which is significantly less than the -0.6 to 2.0 m a^{-1} range found using laser altimetry (Spikes *et al.*, 2003a). Also, the Joughin *et al.* (1999) average thickening rate of 0.49 m a^{-1} is four times higher than the 0.12 m a^{-1} average reported in Spikes *et al.* (2003a). The uncertainties (0.36 to 0.67 m a^{-1}) associated with the Joughin *et al.* (1999) study may be attributed to a few key assumptions. One is the assumption that remotely-sensed ice surface velocities are equal to depth-averaged velocities. This assumption may be valid for ice streams with well-lubricated beds (e.g. Whillans and Van der Veen, 1993; Whillans and Bindschadler, 1988), but KIS stopped streaming ~150 years ago due to a

loss of till dilatency (Retzlaff and Bentley, 1993). As a result, basal friction should have increased the amount of vertical shearing so that depth-averaged velocities are somewhat less than surface velocities. Second, they used a uniform accumulation rate (0.09 m a^{-1}) for the entire KIS region. The issue of spatial variation of accumulation rates is discussed in detail in Chapter 4.4.2.

2.6 Choosing a Mass Balance Approach

The ideal approach for determining the mass balance of the WAIS involves complete coverage with repeat airborne and/or spaceborne laser altimeter surveys and a good distribution of SV stations for validation. Given the distribution of SV stations already in place in West Antarctica and the successful launch of ICESat, the glaciological community appears to be on the verge of resolving the mass balance of the WAIS. However, as of this writing results from GLAS have not been verified and it will take several years to calibrate the instrument, validate measurements, and interpret changes (Zwally *et al.*, 2002). In addition, accumulation variability is expected to introduce large uncertainties so there will need to be independent verification of GLAS results in regions where SV stations are lacking. Furthermore, the mission lifetime of GLAS is projected to be ~ 3 years, which may not be long enough to unambiguously detect changes in all regions.

The above discussion indicates that an alternative approach will provide both interim results and be useful for interpreting ICESat data when it becomes available. The flux-through-a-cell approach is used here because it is capable of revealing spatial patterns of change and it can be applied to small areas where reliable data are available.

Chapter 3

THE GIS APPROACH

3.1 The Geographical Information System

A GIS is made up of different input datasets that are all referenced to a common geographic grid. Each of these datasets comprises a “layer” in the GIS. New layers are either introduced as gridded datasets or created by comparing existing layers using mathematical functions. For this particular GIS, each layer corresponds with a variable in mass balance calculations. Each layer consists of evenly spaced grid cells whose center points are defined according to their x - and y - coordinates. A schematic diagram of a cell in a GIS system is presented in Figure 3.1. The coordinates used in this dissertation are based on a polar stereographic projection with an Earth radius of 6378.137 km, a central meridian of 0° , a standard parallel of 71° S, and an eccentricity of 0.08181881066. The grid spacing, W , used here is 1 km in both the x - and y - directions.

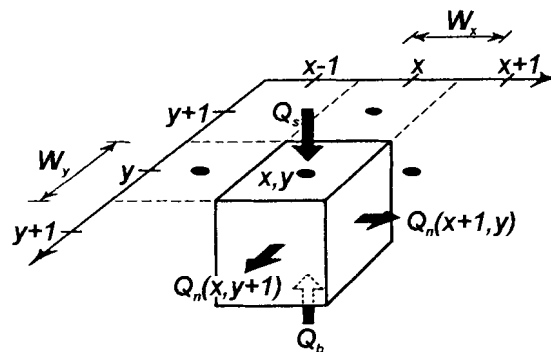


Figure 3.1. Schematic of the flux, Q , through a GIS grid cell at grid point (x,y) . Neighboring grid points are 1-km apart. Figure adapted from Bindschadler *et al.* (1993).

3.2 The Residual Flux Calculation

The equations used to calculate the net mass balance of each grid cell are adapted from those used in Bindschadler *et al.* (1993) and Joughin *et al.* (1999). The net mass balance, N , for any grid cell is computed as:

$$N = \rho \left[\sum_{n=x\pm\frac{1}{2}, y\pm\frac{1}{2}} Q_n + (Q_s + Q_b) \right] \quad 3.1$$

where ρ is the mean ice density (911.7 kg m^{-3} ; Whillans, 1977), $Q_n(x \pm \frac{1}{2}, y \pm \frac{1}{2})$ is the normal component of mass flux across each of the four vertical faces, and Q_s and Q_b are the two horizontal surfaces that correspond with the ice surface (subscript s) and the bed (subscript b) (Figure 3.1). The net mass balance is therefore equal to the residual flux within each grid cell. The flux through each vertical face is a product of ice thickness and horizontal depth-averaged velocity. Figure 3.2 illustrates how ice velocities, and therefore mass flux, can change through the ice column. The flux through the top of each cell is equal to the mass equivalent accumulation rate, \dot{b}_m , multiplied by the surface area of each cube ($W_x \cdot W_y$). The flux through the bed would involve basal melting or accretion, but in this study it is assumed to be zero.

To account for along-flow changes in ice thickness and velocity between adjacent cells, midpoint approximations are used to calculate the mass flux through each of the vertical faces:

$$Q_n(x \pm \frac{1}{2}, y) = \mp \frac{1}{4} [H(x \pm 1, y) + H(x, y)] \cdot [U_x(x \pm 1, y) + U_x(x, y)] \cdot W_y \quad 3.2$$

$$Q_n(x, y \pm \frac{1}{2}) = \mp \frac{1}{4} [H(x, y \pm \frac{1}{2}) + H(x, y)] \cdot [U_y(x, y \pm \frac{1}{2}) + U_y(x, y)] \cdot W_x \quad 3.3$$

where H is ice thickness, and U_x , and U_y are the components of velocity in the x - and y -directions. The positive x -axis is aligned with 90°E meridian, the positive y -axis is aligned with the 180° meridian, and the z -axis is positive upwards (away from the center of the earth). The components of velocity in the x - and y -directions are therefore calculated as:

$$U_x(x, y) = |\vec{U}(x, y)| \sin[\theta(x, y) + \varphi(x, y)] \quad 3.4$$

$$U_y(x, y) = |\vec{U}(x, y)| \cos[\theta(x, y) + \varphi(x, y)] \quad 3.5$$

where \vec{U} is the velocity vector, θ is the azimuth, and φ is the longitude of grid point (x, y) .

The net change in mass balance is reported throughout this dissertation as the rate of ice-equivalent thickness change, \dot{H} , which is not to be confused with the water equivalent (w.e.) values used in this dissertation for other variables such as snow accumulation rates. Quantities of \dot{H} are calculated by:

$$\dot{H} = \frac{N}{W_x \cdot W_x \cdot \rho} \quad 3.6$$

Equations 3.1 through 3.3 are substituted into Equation 3.6 to give:

$$\dot{H} = \frac{1}{4 \cdot W_x} \left\{ \begin{array}{l} [H(x-1, y) + H(x, y)] \\ \cdot [U_x(x-1, y) + U_x(x, y)] \\ - [H(x+1, y) + H(x, y)] \\ \cdot [U_x(x+1, y) + U_x(x, y)] \end{array} \right\} + \frac{1}{4 \cdot W_y} \left\{ \begin{array}{l} [H(x, y-1) + H(x, y)] \\ \cdot [U_y(x, y-1) + U_y(x, y)] \\ - [H(x, y+1) + H(x, y)] \\ \cdot [U_y(x, y+1) + U_y(x, y)] \end{array} \right\} + Q_x + Q_b \quad 3.7$$

which incorporates the gradients in flux in two orthogonal directions plus the net flux through the surface and the bed.

Each of the above equations are exact, and therefore do not introduce error. However, errors associated with the input data will propagate through each of these

equations. To estimate how these errors propagate through Equation 3.7, the law of propagation of variances can be used, so that:

$$\sigma_H^2 = \rho^{-2} \cdot (\rho^2 \cdot (4 \cdot \sigma_{Q_N}^2 \cdot \sigma_{Q_b}^2 \cdot \sigma_{Q_s}^2) + N^2 \cdot \sigma_\rho^2) + N^2 \cdot \rho^{-4} \cdot \sigma_\rho^2 \quad 3.8$$

where σ is the standard deviation of measurements. Equations 3.7 and 3.8 are used extensively in Chapter 5 to calculate the mass balance of grid cells and the associated uncertainties.

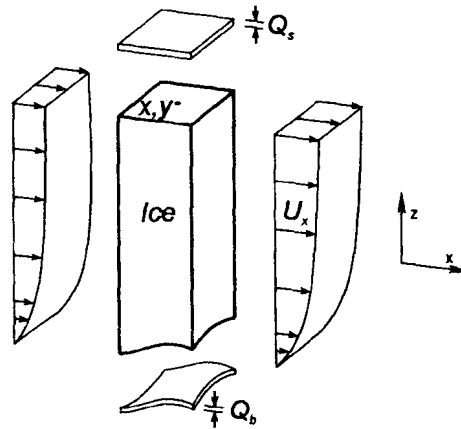


Figure 3.2 Diagram of a column through the ice thickness showing how mass flux can change with depth. For simplicity, the figure shows strain (in the form of longitudinal extension) in the along-flow (x-) direction, but does not show diverging or converging flow. Variables are defined in the text. This figure was adapted from Whillans (1977).

Chapter 4

LAYERS IN THE GIS

4.1 Introduction

Data necessary for estimating mass balance of the WAIS are presented in this chapter. These data include ice-sheet surface topography from the Radarsat Antarctic Mapping Project (RAMP) Digital Elevation Model (DEM) (Liu *et al.*, 1999), ice-sheet thickness from the BEDMAP compilation (Lythe *et al.*, 2000), and snow accumulation rates from the Vaughan *et al.* (1999a) compilation. Newly acquired ground-based measurements of ice-sheet surface elevation (Hamilton and Spikes, 2003; Spikes and Hamilton, 2003), ice-sheet thickness (Welch and Jacobel, 2003), and snow accumulation rate (Spikes *et al.*, 2003c) are also presented. In addition, measurements of ice surface (Bindschadler *et al.*, 1993) and depth-averaged (Whillans, 1979) velocity are described.

Most of the ground-based data presented in this chapter were collected during the United States contribution to the International Trans Antarctic Scientific Expedition (US ITASE). ITASE is a multi-national, multi-disciplinary program to understand the past ~200 years of environmental change in Antarctica (Mayewski, 2003). The U.S. component comprises four traverses, mainly in West Antarctica but also extending into East Antarctica (Figure 4.1). During the traverses ~5000 km of continuous ground penetrating radar (GPR) and global positioning system (GPS) data were recorded while traveling between sites where ice cores were collected and SV stations were installed.

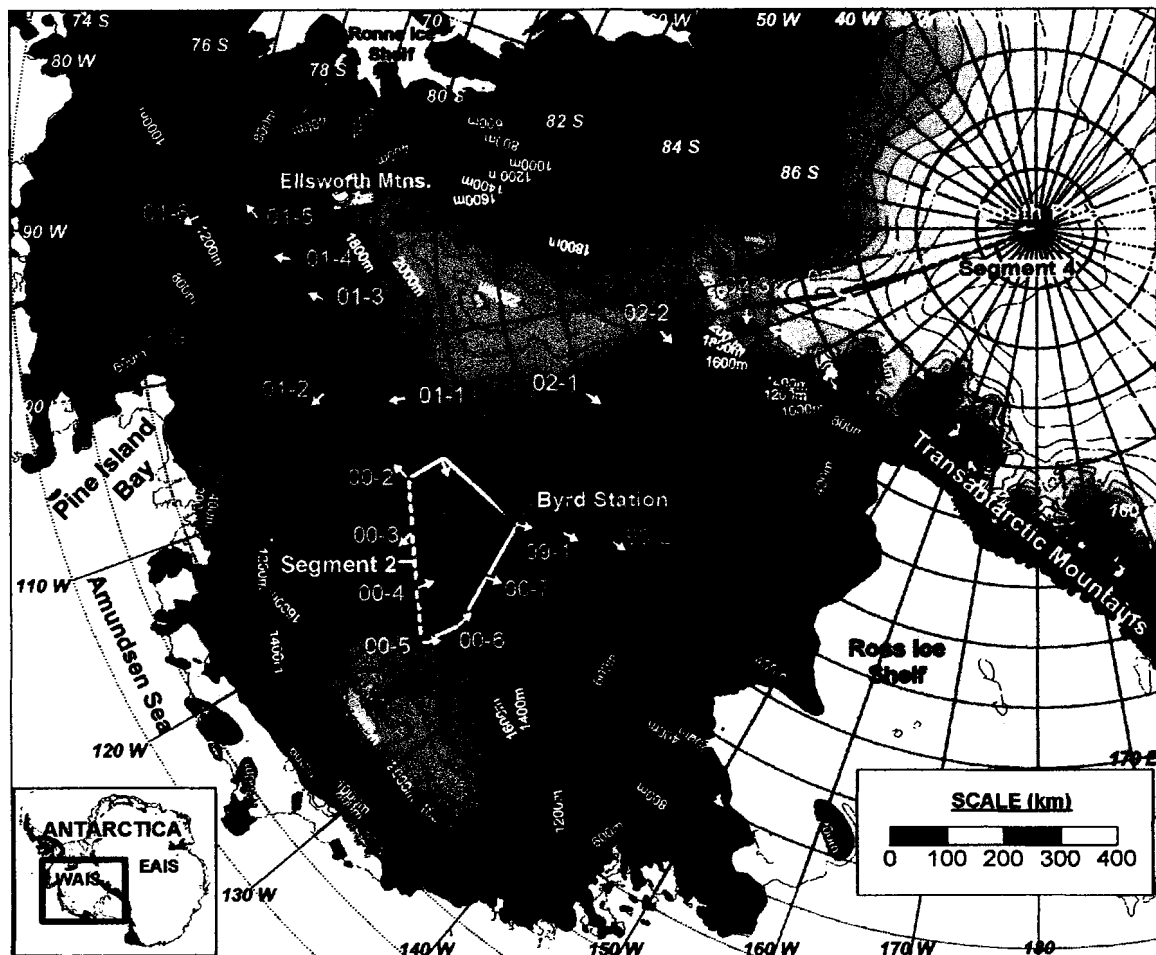


Figure 4.1 Map of US ITASE traverse routes superimposed on surface contours created using a 1-km version of the RAMP DEM (Liu *et al.*, 1999). Elevations are based on the WGS 84 ellipsoid. Red lines indicate 1999-2000 traverses. Blue lines indicate 2000-2001 traverses. Green lines indicate 2001-2002 traverses. Brown lines indicate 2002-2003 traverses. The dashed lines labeled “Segment 1, 2, 3, or 4” indicate profiles used to test the RAMP DEM (see Chapter 4.2.4). Yellow arrows indicate approximated ice flow directions derived from surface slopes. Each arrow corresponds with a US ITASE site where ice cores were collected and SV stations were installed.

Each dataset presented in this chapter is incorporated as an individual layer into the GIS described in Chapter 3.1. However, only the thickness, velocity, and accumulation data are required for residual flux calculations (Equation 3.7). Layers of surface and bed elevation are included in the GIS because they are used to interpret spatial variations in accumulation rate, ice flow (speed and direction), and mass balance.

The views provided for each of the GIS layers include two-dimensional profiles across portions of West Antarctica, three-dimensional maps covering all of West Antarctica (e.g. Figure 4.1), and three-dimensional maps covering a 100-km² grid centered on Byrd Station. The layers for the grid centered on Byrd Station are used in Chapter 5 to calculate the net mass balance of that region using the approach (summed up in Equation 3.7) discussed in Chapter 3.

The sections of this chapter are organized according to surface topography (Chapter 4.2), ice thickness (Chapter 4.3), accumulation rate (Chapter 4.4), and ice flow (Chapter 4.5). Chapter 4.2 begins with a description of the methods used to collect and process GPS data and is followed by a discussion of elevation models for the grid centered on Byrd Station. The GPS measurements are then used to evaluate the vertical accuracy and resolution of the RAMP DEM over different portions of the WAIS. In Chapter 4.3, the GPS data are coupled with ground-based measurements of ice thickness data collected by US ITASE colleagues (Brian Welch and Robert Jacobel, St. Olaf College, Northfield, MN) using low-frequency radar. These data are used to evaluate the BEDMAP compilation (Welch and Jacobel, 2003). In Chapter 4.4, GPS data are coupled with high-frequency radar and ice core data to determine historical snowfall rates along survey lines. The methods used to calculate accumulation rates from radar profiles are

presented in detail and analyses of the spatial and temporal variations in the continuous accumulation records are discussed. These GPR-derived accumulation rates are used to evaluate the Vaughan *et al.* (1999a) accumulation rate compilation. The ice velocity data presented in Chapter 4.5 were retrieved from several sources, including strain grids (Whillans, 1977; Bindshadler *et al.*, 1998), borehole tilting measurements (Whillans, 1979), an SV station (Hamilton *et al.*, 1998), and base station GPS surveys. Separate conclusions are drawn for each of these sections. Each section concludes with a summary of key points.

4.2 Ice Sheet Surface Topography

Surface elevation is important for many types of mass balance studies, including the SV technique (e.g. Hamilton *et al.*, 1998), repeat altimetry (e.g. Krabill *et al.*, 2000; Spikes *et al.*, 2003a), flux calculations along flowlines (e.g. Whillans, 1977), and in flux calculations of drainage basins (e.g. Joughin and Tulaczyk, 2002; Rignot and Thomas, 2002). The surface topography of the WAIS is discussed in detail here, because it is closely related to mass balance variables that are included in Equation 3.7. For example, spatial variations in ice flow can be identified based on subtle changes in surface slope, such as longitudinal streamlines in regions of enhanced ice sheet flow (Casassa and Whillans, 1994) or surface flattening where ice crosses the grounding line (Fricker *et al.*, 2000). Surface topography controls the katabatic wind field (Parish and Bromwich, 1987; Tzenko *et al.*, 1993), which in turn influences local snow accumulation rate gradients (Gow and Rowland, 1965; Whillans, 1975; Kreutz *et al.*, 1999, 2000). The surface topography of an ice sheet is a filtered representation of subglacial morphology, so that

with reasonable assumptions of ice flow and viscosity it is theoretically possible to invert surface shape to derive bedrock topography (Budd, 1970; Fastook *et al.*, 1995). Because of its relationship with each of these variables, surface topography is important in this study for interpreting mass balance results.

The global positioning system (GPS) was used to collect surface elevation data along the US ITASE traverse routes (Figure 4.1). The data were collected along continuous profiles up to 1500 km in length using kinematic surveying techniques. These data are used to provide an independent test of the leading Antarctic digital elevation model (DEM). These data are also used in support of other US ITASE programs, including radar profiling of firm stratigraphy (Chapter 4.4; Arcone *et al.*, 2003; Spikes *et al.*, 2003c) and bedrock topography (Chapter 4.3; Welch and Jacobel, 2003).

Dual-frequency phase-tracking GPS receivers were used throughout this study. One receiver operated for the duration of each field season as a reference station. A second receiver was mounted on one of the traverse sleds and operated in kinematic mode as the expedition moved across the ice sheet. Differential post-processing of the data yielded latitude, longitude and elevation for the moving receiver.

4.2.1 Static Positioning of GPS Reference Station

The reference station consisted of an unattended geodetic-quality Trimble 4000SSi receiver at Byrd Station, which served as the base of operations for all four US ITASE traverses (Figure 4.1) ($80^{\circ}00'51''S$, $119^{\circ}33'39''W$). A compact L1/L2 antenna was mounted approximately 2 m above the snow surface on an aluminum pole. The antenna pole was inserted ~1 m in the firm and stabilized using guy wires. As a further

precaution, the antenna ground plane was removed to minimize wind-induced motion. The antenna was mounted high enough that multipath effects from surrounding camp structures and the snow surface were likely to be insignificant. The receiver was housed inside a tent and powered by a bank of 12-volt batteries charged by a photovoltaic array. There were no power or data loss events during any of the 21-55 day field seasons.

Data were collected at 30-second intervals and saved to the receiver memory as individual day-of-year files. These data were post-processed using the GIPSY-OASIS II software package (Zumberge *et al.*, 1997), which incorporates Earth orientation, precise satellite orbit and clock solutions derived from NASA Jet Propulsion Laboratory's independent analysis of global fiducial stations, to yield daily precise point positions for the Byrd reference station. Formal 1- σ (rms) uncertainties for the daily solutions are typically better than 0.01 m for each of the three components of position. The daily solutions are referenced to the ITRF96 global reference frame using the WGS84 ellipsoidal model.

Two positional trends are observed in the time series of daily solutions for surveys covering all four seasons. One trend results from the location of the Byrd reference station on the moving ice sheet. The horizontal trend in the daily solutions gives an ice velocity of 11.49 m a⁻¹ at an azimuth of 220° (2002-2003 season) which is consistent with an earlier determination of ice velocity of 11.83 m a⁻¹ at an azimuth of 221° (Hamilton *et al.*, 1998) at a nearby (~3 km) site derived from repeat GPS surveys. A second, vertical trend results from firn compaction beneath the antenna mount (Figure 4.2), with a very small vertical contribution due to down-slope flow. The antenna mount is anchored in snow reworked by station activities and therefore does not represent a

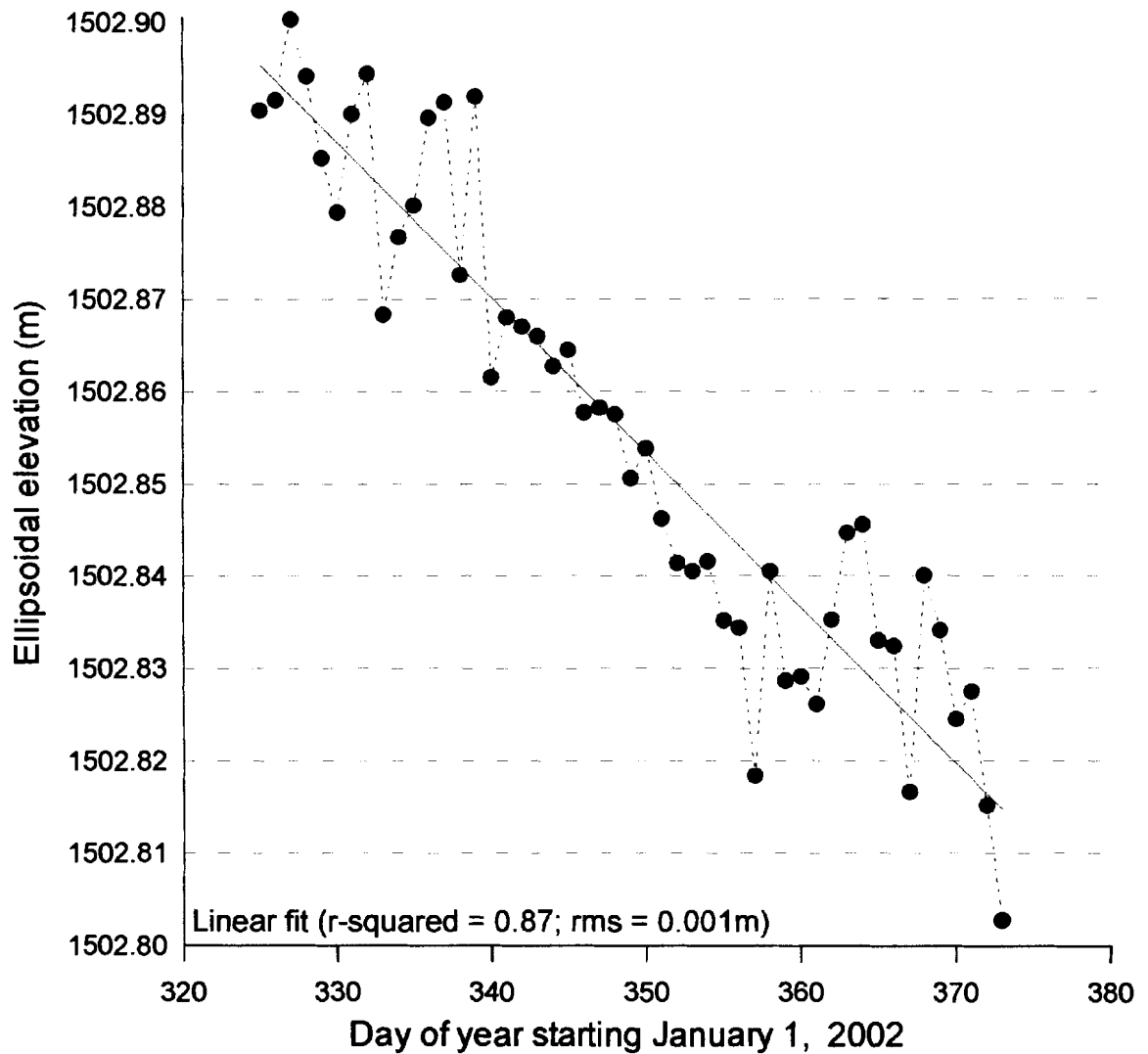


Figure 4.2 Example of the daily trend in the vertical coordinate for the Byrd base station during the 2002-2003 field season. Trends for other seasons are similar.

natural firm compaction time series. However, the trend in vertical position indicates a steady lowering of the near-surface firm during each austral summer field season. A linear regression for the daily solutions (Figure 4.2) was used to provide a position for the Byrd reference because it removes a small amount of scatter in the vertical component of the reference station (Figure 4.2).

4.2.2 Kinematic Positioning Along Survey Lines

Kinematic GPS data were collected by a second receiver (Trimble 4000SSi) and antenna carried on one of the traverse vehicles. The antenna (a compact L1/L2 antenna with ground plane removed) was mounted on a short pole attached securely to the roof of a sled structure. Multipath effects are considered to be negligible because the structure was fabricated predominantly from wood and also because the antenna was mounted higher than any surrounding objects (3.8 m above the snow surface). Data were collected at a 30 s rate, corresponding to an approximate along track distance between points of 60–90 m based on typical traverse speeds ($\sim 2\text{--}3\text{ m s}^{-1}$). Each kinematic survey was typically 100–200 km in length.

The kinematic survey data are processed differentially to the reference station at Byrd. The baseline processing engine in Trimble's GPSurvey® software suite and precise ephemeris products obtained from the International GPS Service for Geodynamics (<http://igsceb.jpl.nasa.gov/>) were used to calculate static and kinematic solutions for each data file. This same processing procedure was used successfully to obtain kinematic solutions over baselines of several hundred km during airborne survey work in West Antarctica (Spikes *et al.*, 2003b).

Baseline lengths used in this study range from 0-1100 km. Each kinematic GPS survey began and ended with long-duration static occupations. Static initializations lasted a minimum of 8 hr, but were usually 18 – 24 hr for distant baselines. The use of two static occupations (beginning and end) allowed for forward and backward processing of the kinematic data in the event of problems. Fixed-integer, ionospherically-corrected kinematic solutions were obtained for > 90% of the data. For a few cases (not used in the present study), fixed-integer solutions were not possible because of “loss-of-lock” events due to excessive antenna motions during travel (instantaneous accelerations) or poor dilution of precision (DOP) of the satellite constellation during short survey periods. In these cases, positions were recovered using float solutions or C/A code data.

Uncertainties in the kinematic solutions are very acceptable given the long distances from the reference station at Byrd. Maximum uncertainties in the vertical component of position never exceed 0.2 m (rms). Horizontal position uncertainties are considerably smaller. These results show that it is possible to reliably determine position and elevation data using kinematic GPS techniques with large separation distances from a reference station. This technique offers the potential for detailed mapping of other remote locations in Antarctica and elsewhere using ground-based and airborne surveys.

4.2.3 High-resolution Mapping of Three-dimensional Grids

Kinematic GPS surveys were used to produce local topographic maps for each of the twenty-two locations where the US ITASE stopped to collect ice cores and install SV stations. The sampling rate of these surveys was increased to 5 s to accommodate the faster travel speed of the snowmobile used to carry the GPS equipment, resulting in an

along-track spacing of ~25 m between consecutive measurements. These surveys generally consist of concentric rings or crossing patterns that cover an area that is ~15 km². These maps serve several purposes. Derived surface slopes are required for mass balance calculations using SV stations (Hulbe and Whillans, 1994; Hamilton *et al.*, 1998). The maps are also coupled with ice flow rates and used to interpret the effects of topography and ice flow on accumulation rates derived from ice cores (Kaspari *et al.*, 2003) and GPR surveys (Spikes *et al.*, 2003c).

More extensive mapping in three-dimensional grids was performed at two sites, Byrd Station and 02-3 (Figures 4.3 and 4.4). The sites will be used to determine the ranging accuracy of GLAS (discussed in Chapter 2.2) on board ICESat. The map for Byrd Station is also used to evaluate the RAMP DEM (see Chapter 4.2.4). The grid at Byrd Station is 10 x 10 km and the grid at 02-3 is 5 x 5 km (Figure 4.3).

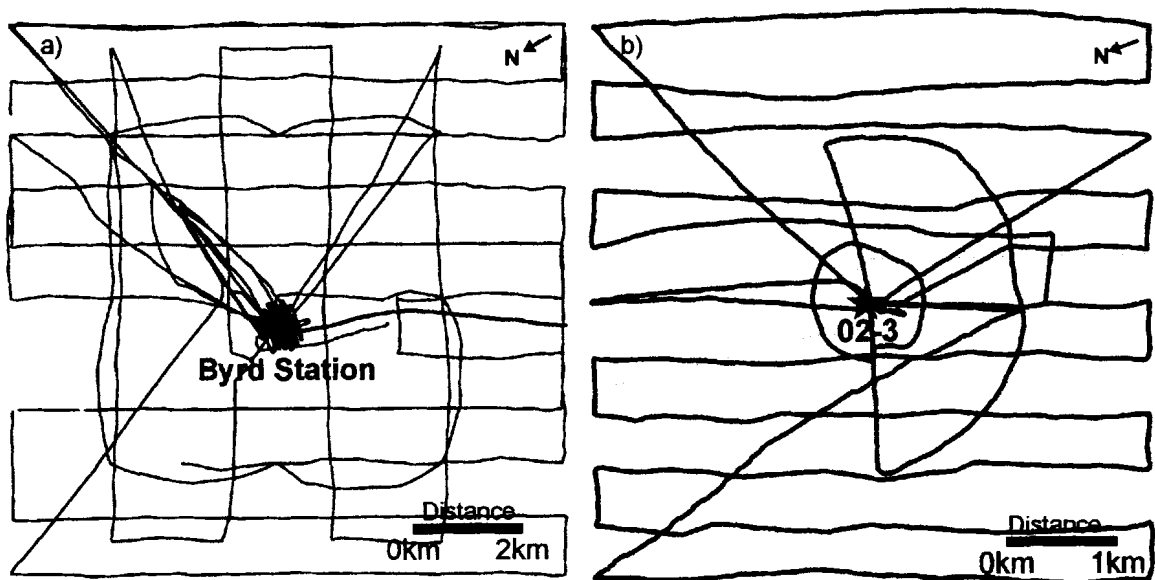


Figure 4.3 Tracks of GPS surveys around Byrd Station (a) and 02-3 (b). Stars locate the GPS base stations. Note that each map has a different scale bar.

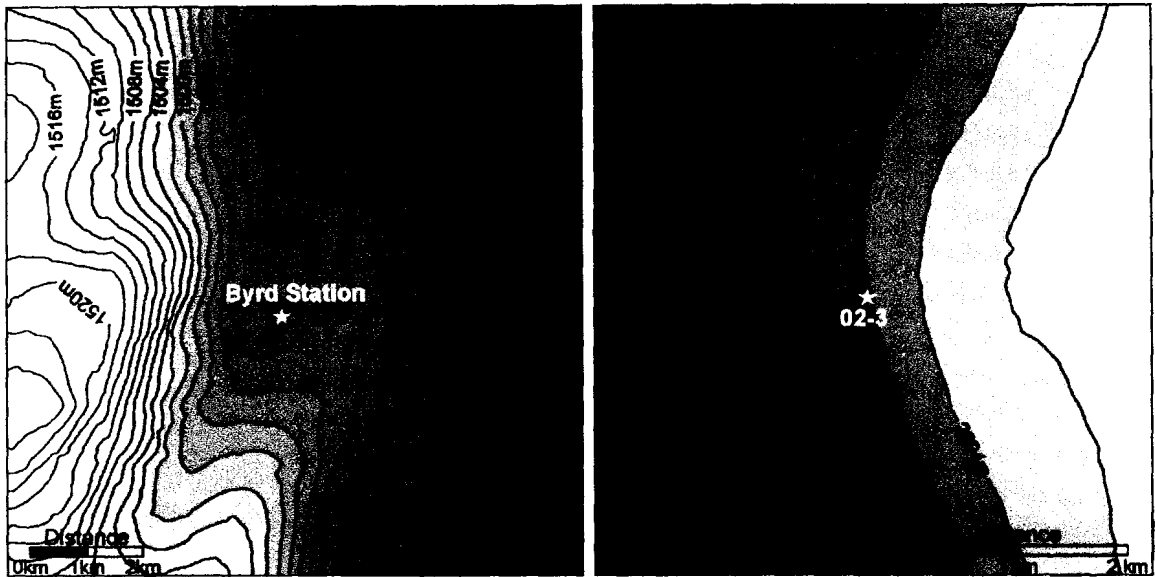


Figure 4.4 Interpolated contours of ice sheet surface topography around Byrd Station (a) and 02-3 (b). Stars locate the GPS base stations. Note that each map has a different scale bar.

Using a combination of pre-planned routes and semi-random surveys an even distribution of measurements was obtained within each grid (Figure 4.3). The overall spacing between measurements varies from <1 m to ~ 1 km. Topographic maps of each site were produced by kriging (e.g. Isaaks and Srivastava, 1989) the data to 100-m grid spacing (Figure 4.4).

There are a number of points within each grid where nearly coincident (<2 m separation distance) measurements occurred. These points are used to estimate uncertainties in measured elevations related to GPS errors and surface roughness (Figure 4.5), although no attempt is made here to separate these two components. Analyses of these points revealed average uncertainties in elevation of 0.030–0.11 m for 02-3 and Byrd Station, respectively. The small uncertainties at 02-3 are attributed to the minimal

separation distance (≤ 3.5 km) between the roving and base station receivers. The relatively large errors at Byrd Station are attributed to the larger separation distance between receivers (≤ 7 km), and to the greater number of independent surveys used to map this site (6 surveys at Byrd Station versus 2 surveys at 02-3).

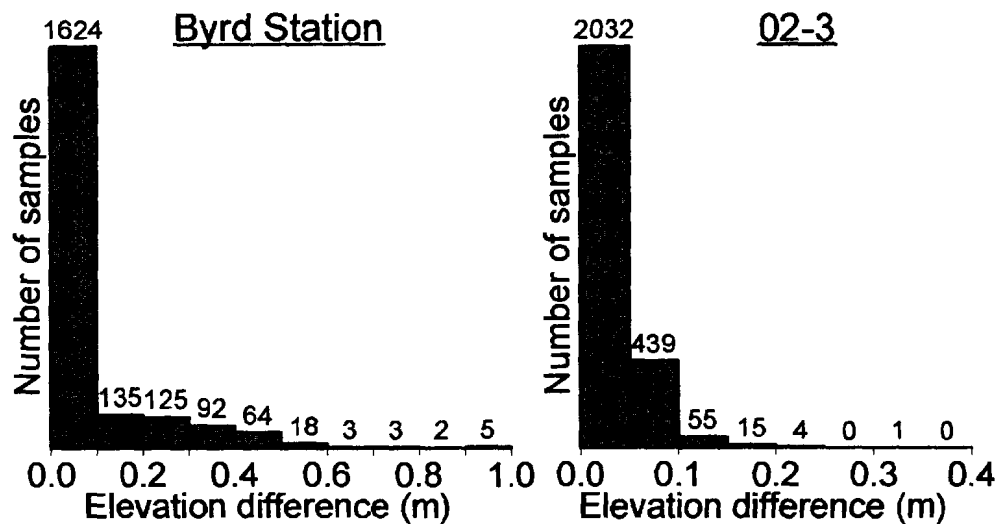


Figure 4.5 Distribution of uncertainties in the elevation component of GPS positions around Byrd Station and 02-3. Uncertainties are based on the elevation difference between nearly coincident survey (< 2 m separation distance) points.

4.2.4 Evaluation of the RAMP DEM

The RAMP DEM represents the best available compilation of Antarctic surface topography (Liu *et al.*, 1999; Jezek *et al.*, 1999). This DEM was constructed to guide the geometric rectification and continental mosaicking of radar imagery collected by Radarsat (Liu *et al.*, 1999; Jezek, 1999). The foundation for the DEM is ERS-1 altimeter data collected in the mid-1990s, augmented where available with other mapping and

survey information. This DEM represents an improvement over older terrain models by incorporating ancillary mapping information from ground-based and photogrammetric surveys, as well as rigorous GIS based interpolation and error detection techniques. The RAMP DEM, available from the National Snow and Ice Data Center (NSIDC), is being widely used in a variety of glaciological studies.

Because of well-documented uncertainties in the way that altimeter waveforms interact with the surface layers of an ice sheet (e.g., Davis and Moore, 1993), as well the performance of altimeter re-tracking algorithms over regions of relatively steep slopes (Bamber, 1994), there is the potential for errors to be introduced into the RAMP DEM. During the initial compilation of the DEM, Liu *et al.* (1999) conducted validation exercises using existing terrestrial survey data. However, the spatial resolution of most of those surveys was not optimized for studying the fine-scale (< 10 km) morphology of Antarctica. Therefore it is desirable for additional independent tests to assess how well the DEM describes the detailed surface topography of the ice sheet. These tests can also provide quantitative estimates of the DEM's resolution.

Here, GPS data collected continuously along several profiles 150-320 km long in West and East Antarctica are used to independently evaluate how well the RAMP DEM (Version 2 with 1-km grid spacing) describes the shape of the ice sheet surface. Kinematic GPS techniques have been used in validation tests of other, regional-scale satellite altimeter-derived Antarctic DEMs (e.g. Phillips *et al.*, 1997). For the purposes of the present analysis, four segments (Figure 4.1) have been selected that are typical of different ice sheet regimes contained in the RAMP DEM. Segment 1 covers characteristic undulating topography in the ice sheet interior, Segment 2 crosses a major West Antarctic

flow and drainage divide, Segment 3 approximately follows a flow line to an onset region of enhanced flow, and Segment 4 represents an interior ice sheet profile across a region where the RAMP DEM is poorly constrained by altimeter data. In addition, the 100-km² grid centered on Byrd Station (Figures 4.1 and 4.4) is used to assess the detailed three-dimensional topography in the RAMP DEM. Because these data were collected after the release of the RAMP DEM and were not used in its compilation, they constitute a valuable independent test of the DEM's performance. Ellipsoidal elevations in both datasets are used in the following comparisons, so errors in geopotential heights are not important.

Segment 1 is located in the upper drainage basin of Thwaites Glacier (Figure 4.1). The profile extends 150 km down glacier from a point close to the ice divide. There is a 500 m elevation decrease along the profile. The ice sheet surface in this region is relatively smooth (Figure 4.6a). The GPS and DEM profiles agree very well over the relatively smooth sections of Segment 1 (Figure 4.6a). The rms of elevation differences between the two profiles is less than 5 m in these regions. The largest differences in elevation occur in rugged sections of the GPS profile. Horizontal smoothing (using a running average) of the GPS profile, which dampens the amplitude of the undulations, reduces the elevation differences. The rms of the elevation differences between profiles reaches a minimum if an 8 km horizontal smoothing is used for the GPS profile (Figure 4.6a), implying that the true horizontal resolution of the DEM is coarser than the original estimate of 5 km (Liu *et al.*, 1999).

Segment 2 is a 320 km long profile that crosses two local ice divides before climbing to the crest of the major ice divide in central West Antarctica (Figure 4.1). The

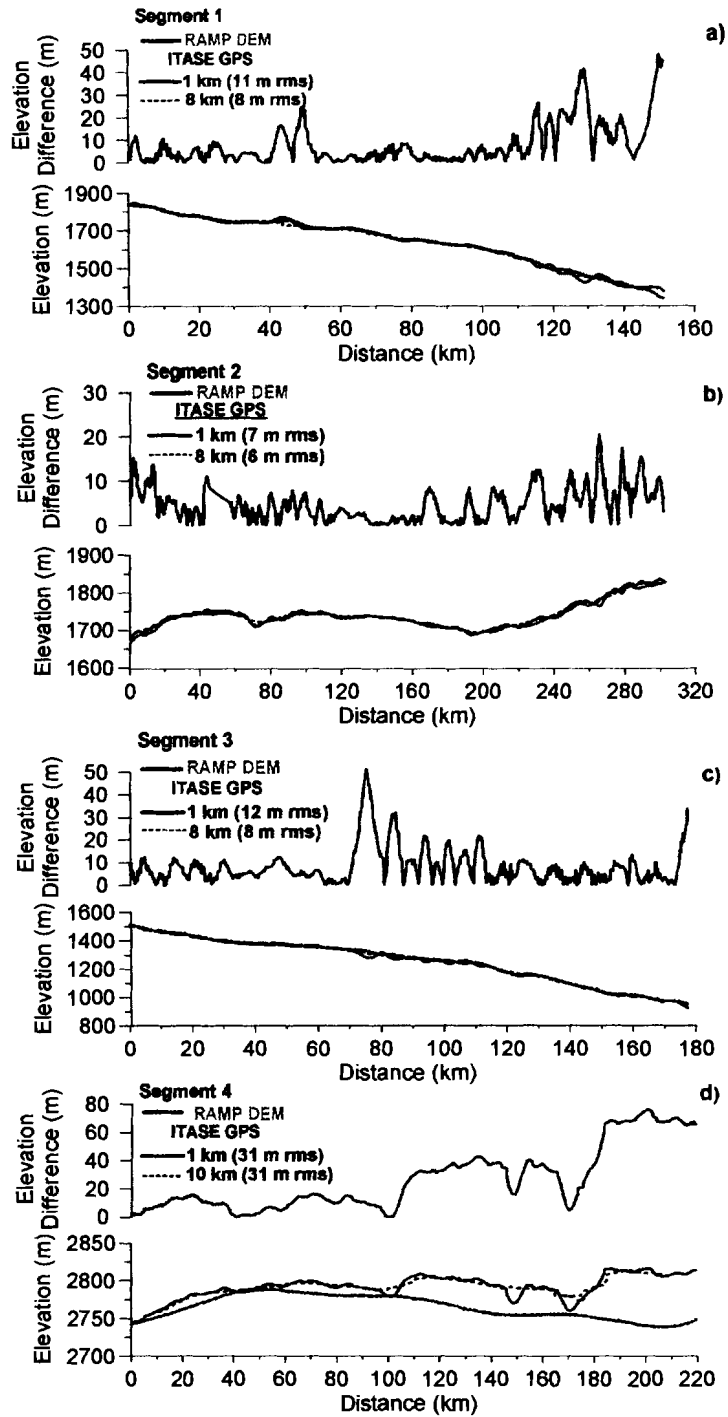


Figure 4.6 Differences between GPS and RAMP DEM along two-dimensional profiles. A) Segment 1 – traverse from 01-1 to 01-2. B) Segment 2 – traverse from 00-2 to 00-5. C) Segment 3 – traverse from Byrd Station to 99-2. D) Segment 4 – traverse from 02-5 to South Pole. For all segments, the black line is the GPS data smoothed to a 1 km horizontal resolution, the gray line is the DEM surface, and the dashed line is the GPS data smoothed to 8 km horizontal resolution. The locations of each segment are shown on Figure 4.1.

total elevation gain along the profile is slightly less than 200 m (Figure 4.6b). The profile derived from the DEM captures nearly all these large-scale features, although most of the smaller-scale roughness in the GPS profile is missing. Overall, the rms of elevation differences between the two profiles is reasonable, although this agreement is partly due to the small amplitude of the features not captured by the DEM surface. There was no substantial improvement between the two profiles, as defined by a reduction in the rms of elevation differences, when the GPS data were smoothed to an 8 km horizontal resolution (Figure 4.6b).

Segment 3 was collected along an approximate flow line leading from Byrd Surface Camp to the onset region of streaming flow in the upper portion of Bindschadler Ice Stream (formerly Ice Stream D) (Figure 4.1). There is an almost monotonic decrease in elevation of 550 m along the 177 km profile (Figure 4.6c). A comparison of the GPS and DEM surface profiles shows good agreement in relatively smooth sections of the segment (Figure 4.6c). However, the DEM profile does not capture the series of undulations in the ice stream onset region. In this section of the segment, elevation differences between the two profiles are as large as 50 m (Figure 4.6c). The agreement between the two profiles is improved substantially by smoothing the GPS profile with an 8 km horizontal spacing. There is no significant improvement if the smoothing distance is increased beyond 8 km. The implication of this smoothing analysis is that the horizontal resolution of the DEM is on the order of 8 km, which is substantially coarser than the 5 km estimated by Liu *et al.* (1999). This coarser estimate of spatial resolution is noteworthy if the DEM is being used to map features characteristic of enhanced ice flow.

Segment 4 is located on the interior East Antarctic Ice Sheet close to South Pole

(Figure 4.1). In this region of the continent, the RAMP DEM is poorly constrained by mapping data (Liu *et al.*, 1999). Because satellite altimeter measurements do not extend south of 82°S, the DEM in the central portion of Antarctica is constructed from isolated airborne survey data. Therefore large errors might be expected in the way the DEM describes ice sheet topography in this region. Differences in elevation between the two profiles along this segment are relatively large (31 m rms). The rms of elevation differences does not improve when a relatively long smoothing distance of 10 km is used for the GPS profile (Figure 4.6d). This result is not unexpected, because the smoothed GPS surface maintains the broad morphology of the finer-resolution profile, including an upland plateau that is missing in the DEM (Figure 4.6d). The spacing of survey flight lines in this region was probably coarser than the dimensions of the plateau, explaining why it is absent in the DEM data. Liu *et al.* (1999) estimate the resolution of the DEM in this region to be about 10 km, but this analysis suggests that the horizontal resolution is probably closer to 50 km.

The segments described above are one-dimensional profiles across the ice sheet surface. It is also important to understand how well the RAMP DEM describes three-dimensional topography at the scale of typical ice sheet surface features (about 2-10 km), because these features exert strong local control on snow accumulation. The detailed map of the surface topography around Byrd Station is used to investigate this issue (Chapter 4.2.3; Figure 4.4). This grid is located within the region of the DEM that is well constrained by satellite altimeter data. The GPS-derived topography displays three facets. A steep sloping section dominates the grid west portion of the map (Figure 4.4). The central region is relatively flat and the grid east portion displays a gentle slope. Byrd

Surface Camp is located on a small but prominent ~10 m high bump (Figure 4.4) formed by sustained preferential accumulation of snow around the station structures. The surface topography constructed from the RAMP DEM does not contain the same amount of detail as the GPS-derived map (Figure 4.7a). There are no distinct facets and the DEM omits the bump at Byrd Surface Camp. There is an elongated, wide, flat ridge on the grid west section of the map, but otherwise the slope decreases evenly from grid west to grid east across the map. A plot of the elevation offsets between the two maps shows a zone of maximum differences just to the grid west of Byrd Surface Camp, on the relatively steep section of the GPS map (Figure 4.7b).

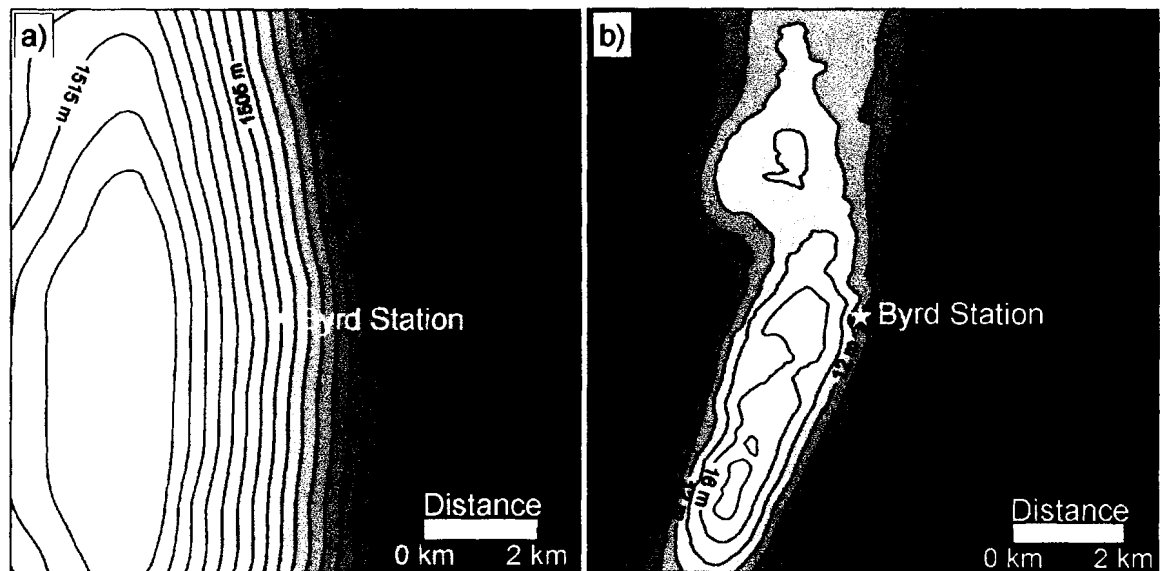


Figure 4.7 Differences between GPS and RAMP DEM in the vicinity of Byrd Station. Crosses indicate GPS base at Byrd Station. a) Topography from RAMP DEM. b) Elevation differences between GPS measurements (see Figure 4.4) and the RAMP DEM. GPS survey tracks are shown in Figure 4.3a.

4.2.5 Discussion

According to Liu *et al.* (1999), the horizontal resolution of this DEM is 5 km in the ice sheet interior, where satellite altimeter data were used in the compilation, and ~10 km in the central portion where altimeter data are not available (Liu *et al.*, 1999). Based on the present analysis, the horizontal resolution is found to be closer to 8 km in the better-constrained regions of the DEM and substantially coarser than 10 km (probably close to 50 km) in the data-sparse central portion. This means that the RAMP DEM performs very well at describing the first order topography of the Antarctic Ice Sheet. North of 82°S, the DEM correctly describes the principal surface slopes and drainage divides (although beyond this latitudinal limit there are large errors in the ice sheet surface shape and important topographic maxima are missing). The most noticeable difference between the GPS and DEM profiles is the way in which small-scale (2-10 km) surface roughness is characterized. Surface roughness in the DEM is either absent, attenuated, or offset in location relative to the GPS profiles. Therefore the rms differences in elevation between the GPS and DEM profiles (~10 m for the regions north of 82°S) are biased by large discrepancies in areas of rugged topography not captured by the DEM. If these sections are excluded, rms differences are closer to 2 m. This level of agreement is acceptable, considering uncertainties in GPS vertical positioning and a potential, but unknown, depth of penetration of the altimeter signal into the surface firn (e.g. Davis and Moore, 1993).

It is unlikely that these differences are the result of the two datasets being compiled at different times. The RAMP DEM is based primarily on ERS-1 satellite altimeter data collected in the early 1990s whereas the GPS data were collected between

1999 and 2003. Bumps and undulations on an ice sheet evolve through processes of infilling by snow and upglacier migration (Budd, 1970), although on short timescales these features can be assumed to be time-invariant. These two processes therefore should not have any detectable effect on the comparison of profiles collected only a few years apart.

4.2.6 Conclusions

The horizontal resolution of the leading Antarctic DEM has important implications for several glaciological studies. Because most of the 2-10 km scale surface roughness is omitted, the DEM is limited in its ability to characterize local variability in snow accumulation rates resulting from changes in surface gradient (Chapter 4.4.2.2). The use of the DEM to identify features based on a topographic signature, such as flat surfaces indicative of subglacial lakes, or streamlines indicating regions of enhanced flow, will be limited to features substantially larger than the 8 km horizontal resolution of the data. In the central portion of the DEM (south of 82° S), the positions of drainage divides might be wrongly located which will affect mass balance calculations. Finally, experiments aimed at inverting the ice surface topography contained in the DEM to obtain maps of subglacial bedrock will result in missing valleys and mountains ranges.

4.3 Ice Thickness

Ice thickness is a key variable in calculations of depth-averaged horizontal ice velocity and mass balance. Also, ice thicknesses are subtracted from surface elevations to produce bedrock elevations. Unlike surface topography which has been measured using a

variety of ground-based, airborne, and satellite techniques (Chapter 4.2), ice thickness measurements are considerably more limited. Low frequency radio-echo sounding (RES) is the most common and the most reliable approach to measuring ice thickness. These surveys can be conducted from ground-based (e.g. Welch and Jacobel, 2003) and airborne (e.g. Retzlaff *et al.*, 1993; Blankenship *et al.*, 2001) platforms. Ground-based seismic reflection surveys have also been used to map ice thickness and bedrock topography (e.g. Lythe *et al.*, 2000).

4.3.1 Maps of Bedrock Topography and Ice Thickness

The only continent-scale dataset of Antarctic ice thickness is the BEDMAP compilation of ground-based and airborne radio-echo sounding (RES) surveys (Lythe *et al.*, 2000). Bedrock elevations included in this compilation are a product of RAMP surface elevations minus BEDMAP ice thickness values. A 5-km gridded version of this compilation is available from the British Antarctic Survey (<http://www.antarctica.ac.uk/aedc/bedmap/>). The errors associated with this dataset are highly variable, because there are large areas of Antarctica that have not been surveyed (Lythe *et al.*, 2000). In these areas, interpolation is used to estimate bedrock elevations.

Kriging was used to generate an interpolated grid (e.g. Isaaks and Srivastava, 1989) of BEDMAP ice thickness data covering West Antarctica and the South Pole region (Figure 4.8). A bedrock elevation map (Figure 4.9) was created by subtracting the BEDMAP ice thickness values in Figure 4.8 from the RAMP ice surface elevations in Figure 4.1 using a GIS approach. The map of bedrock elevations (Figure 4.9) shows that most of West Antarctica is below sea level.

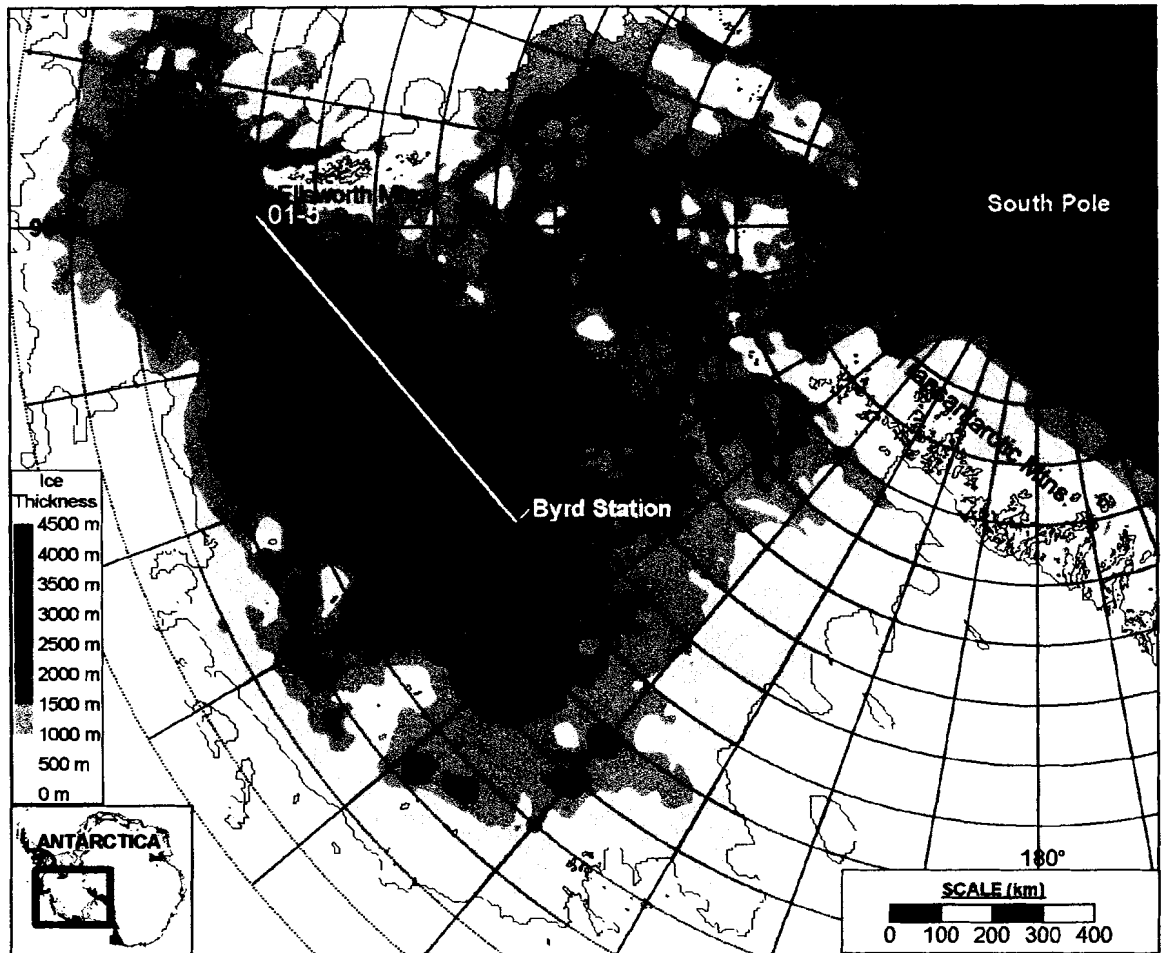


Figure 4.8 Map of ice sheet thickness for West Antarctica and the South Pole region (Lythe *et al.*, 2000). The dashed red lines are the US ITASE traverse routes. The white line locates the profile used to test the accuracy of BEDMAP (Figure 4.11).

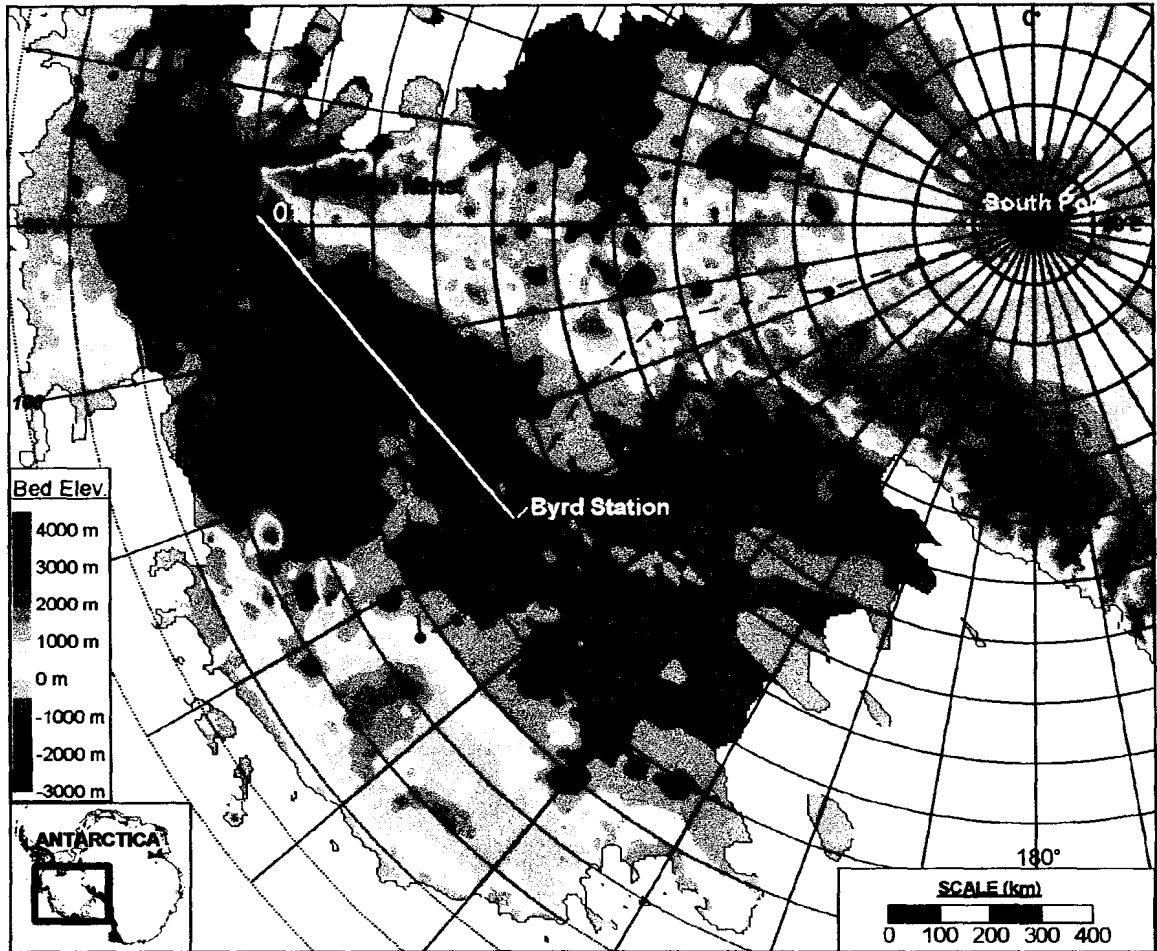


Figure 4.9 Map of bedrock topography for West Antarctica and portions of East Antarctica (Lythe *et al.*, 2000). Elevations are based on the WGS 84 ellipsoid. The dashed red lines are the US ITASE traverse routes. The white line locates the profile used to test the accuracy of BEDMAP (Figure 4.11).

Using the same approach, local maps of bedrock topography and ice thickness centered on Byrd Station were created (Figure 4.10). The bedrock map (Figure 4.10a) shows a steep gradient from left to right across this area, which corresponds with a subglacial peak that has been observed in several studies (e.g. Whillans, 1979; Welch and Jacobel; 2003).

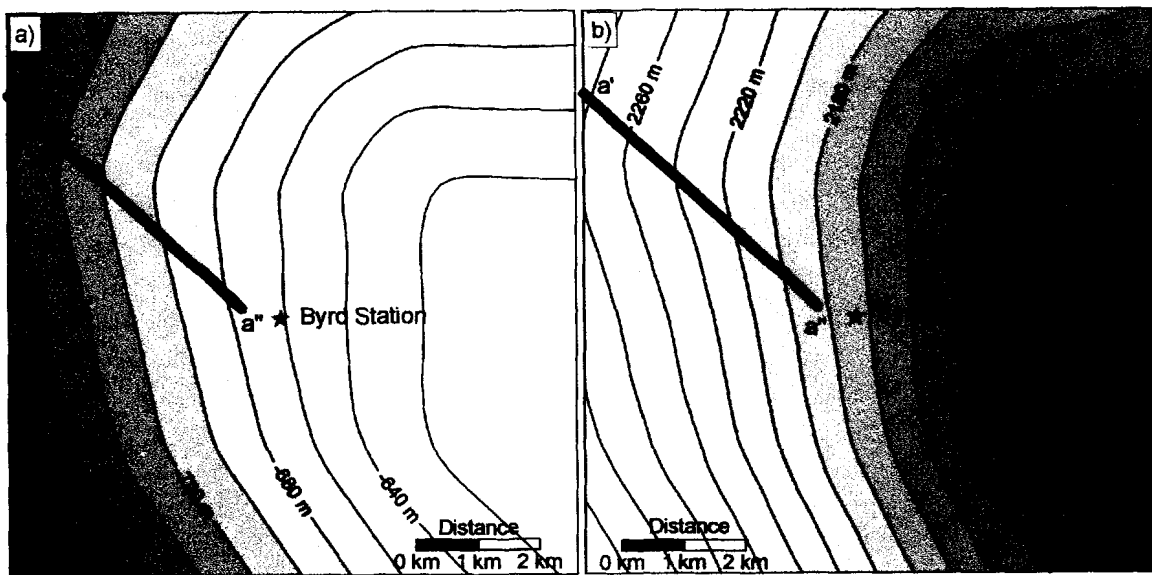


Figure 4.10 Maps of bedrock topography and ice thickness for the 100-km² grid centered on Byrd Station. Profile a' – a'' corresponds with the Welch and Jacobel (2003) survey presented in Figure 4.11.

4.3.2 Evaluation of BEDMAP

Along the US ITASE traverse routes, ice thickness was measured using a 3-MHz short-pulse transient type radar (Welch and Jacobel, 2003). The 3-MHz measurements are geolocated using simultaneously recorded GPS data (Chapter 4.2.2). Results from

GPS and 3-MHz radar surveys along a 737-km linear cross-section of the WAIS stretching from Byrd Station to 01-5 (Figure 4.8) are shown in Figure 4.11. Welch and Jacobel (2003) used these data to determine the range of errors contained in the BEDMAP compilation (Figure 4.11). They found that ice thickness errors in the BEDMAP compilation along this profile vary from 0 to 1200 m (avg. deviation is ~15% of ice thickness) (Figure 4.11a). A portion of the data presented in Figure 4.11 was recorded along line **a' – a''** in Figure 4.10. This short profile shows that the average error in the BEDMAP compilation is ~70 m in the vicinity of Byrd Station (Figure 4.12).

4.3.3 Conclusions

The BEDMAP compilation of ice thickness measurements can be a source of uncertainty when incorporated into glaciological studies. A standard error of $\pm 15\%$ translates to a mean error of 240 m, given the mean thickness of the WAIS is ~1600 m (Lythe *et al.*, 2000). This has important implications for calculations of driving stress, balance velocity, and basal stresses (normal and shear). Here, ice thickness is incorporated into estimates of ice flux through 1-km grid cells. The typical errors observed in the BEDMAP compilation (Figure 4.11) exceed the typical bedrock gradients observed in the US ITASE 3-MHz radar (avg. gradient = 40 m km^{-1}) and BEDMAP (avg. gradient = 10 m km^{-1}) profiles by a factor of 6 and 24, respectively. These gradients indicate that the difference in ice thickness between adjacent 1-km grid cells is typically smaller than the error associated with each BEDMAP ice thickness value.

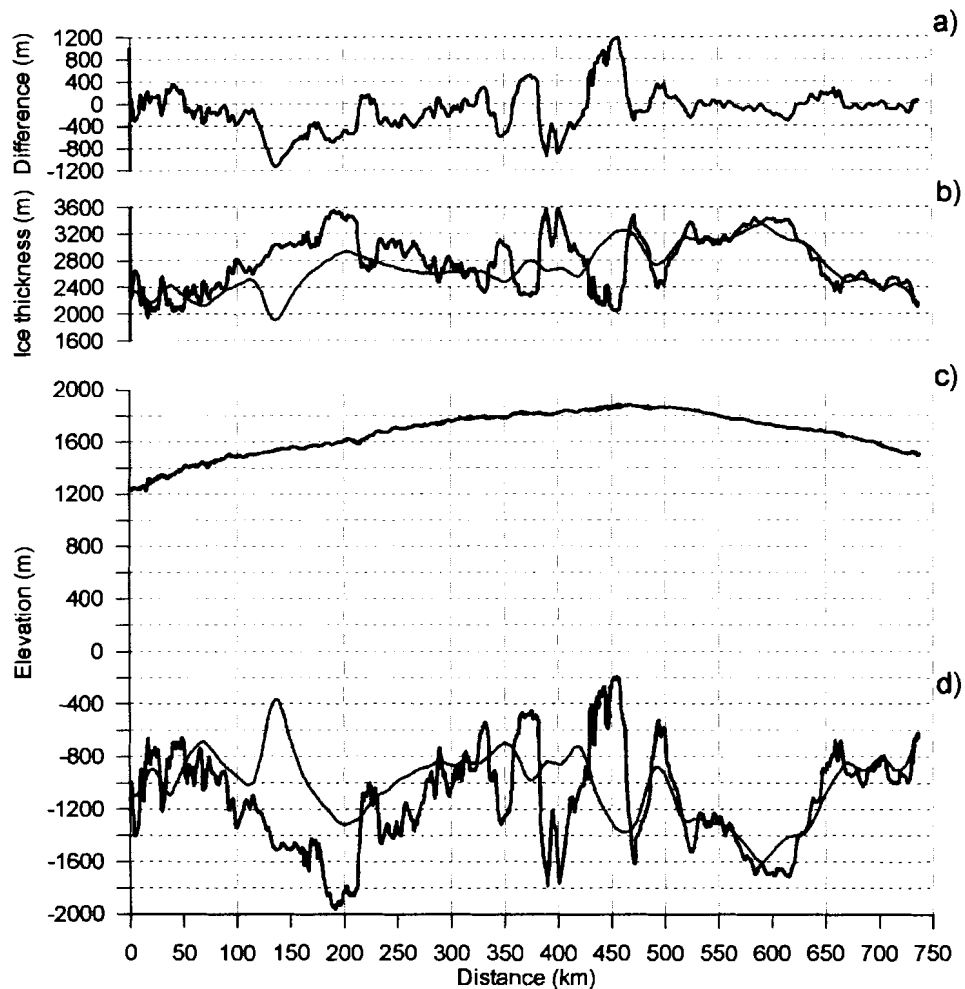


Figure 4.11 WAIS cross-section between Byrd Station and 01-5 (see Figure 4.8). Black lines indicate ground-based measurements from US ITASE. Blue lines indicate data from continent-scale data compilations. Red lines correspond with profile $a' - a''$ in Figures 4.10 and 4.12 (a'' is on the far right). a) Difference between US ITASE and BEDMAP ice thickness values. b) Ice thickness from US ITASE 3-MHz radar surveys and the BEDMAP compilation. c) Ice surface topography (based on the WGS 84 ellipsoid) from US ITASE GPS surveys and the RAMP DEM. d) Bedrock topography from US ITASE 3-MHz radar surveys and the BEDMAP compilation.

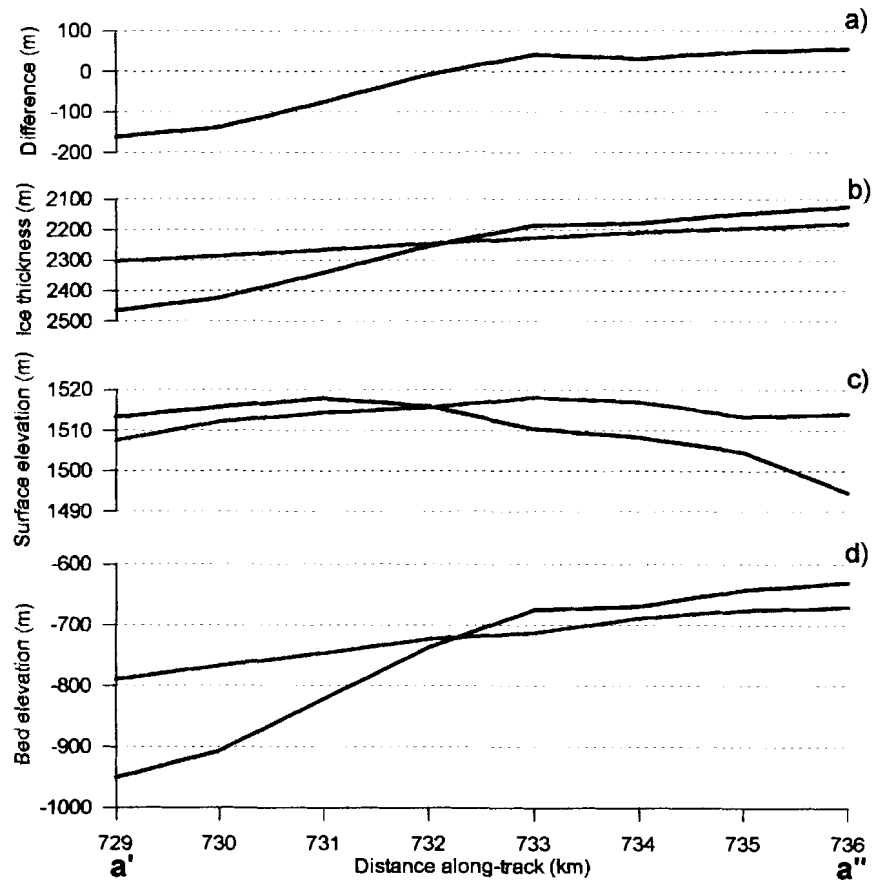


Figure 4.12 WAIS cross-section along profile a' – a'' in Figures 4.10 and 4.11. Black lines indicate ground-based measurements from US ITASE traverses. Blue lines indicate data from continent-scale data compilations. a) Difference between US ITASE and BEDMAP ice thickness values. b) Ice thickness from US ITASE 3-MHz radar surveys and the BEDMAP compilation. c) Ice surface topography from US ITASE GPS surveys and the RAMP DEM. d) Bedrock topography from US ITASE 3-MHz radar surveys and the BEDMAP compilation.

4.4 Snow Accumulation Rates

Snow accumulation rates on the Antarctic ice sheet are known to be highly variable over short distances (e.g. Black and Budd, 1964; Gow and Rowland, 1965; Whillans, 1975, Richardson *et al.*, 1997; Kreutz *et al.*, 1999, 2000; Richardson and Holmlund, 1999; Vaughan *et al.*, 1999b) and over short time intervals (e.g. Moseley-Thompson *et al.*, 1999, Kaspari *et al.*, 2003). However, accumulation rates in Antarctica are not well characterized, because they have generally been assessed using compilations of widely spaced point measurements and low-resolution (~25 km) passive microwave data (e.g. Vaughan *et al.*, 1999a; Giovinetto and Zwally, 2000), neither of which capture the full range of accumulation variability, and may not produce an accurate spatial mean (e.g. Richardson *et al.*, 1997; Richardson and Holmlund, 1999). This observation has important implications for studies of ice sheet mass balance and sea level rise, because accumulation of snow is a key quantity for mass balance calculations (e.g. Shabtaie and Bentley, 1987; Hamilton *et al.*, 1998; Wingham *et al.*, 1998; Joughin and Tulaczyk, 2002; Rignot and Thomas, 2002).

Preservation of snowfall on ice sheets provides a stratigraphic record that can be used to determine how rates of snow accumulation have changed over time. These records can be interrupted by wind erosion and melt events, and they can also be distorted by ice flow. Ice cores provide chemical and isotopic records that can be used to determine depth to age relationships in the ice and identify gaps in the record. However, ice cores recovered even a few kilometers apart can give very different values as a result of changes in ice flow and topographic influences on snow accumulation. Over larger distances (>50km) differing climatic regimes tend to dominate the accumulation record.

To parameterize spatial variability in accumulation, ground-penetrating radar (GPR) was used to fill in the gaps between distant ice cores.

Continuous horizons can be traced in radar profiles for hundreds of kilometers along US ITASE routes (Arcone *et al.*, 2003). The confirmation that these horizons are isochronal (Chaper 4.4.1; Spikes *et al.*, 2003c) makes it possible to fill in the gaps between US ITASE ice cores and quantitatively determine how snow deposition changes spatially as well as temporally for large areas of West Antarctica.

4.4.1 Isochronal Nature of Continuous Radar Reflections

Internal layers in ice sheets, tracked as radar horizons, are assumed to represent isochronal events (e.g. Kohler *et al.*, 1997; Richardson *et al.*, 1997; Richardson and Holmlund, 1999; Vaughan *et al.*, 1999b; Eisen *et al.*, 2003a; Kanagaratnam *et al.*, 2001). This assumption does not distinguish between events that occurred over a period of days (melt events, storms, etc.) or a few years (volcanic eruptions). Several studies show evidence that continuous radar reflections in firn are caused by dielectric permittivity fluctuations related to density (Arcone *et al.*, 2003), and not by dielectric or conductivity variations related to chemistry (Eisen *et al.*, 2003b; Fujita *et al.*, 1999). It seems plausible that the same synoptic-scale weather systems that control ion deposition over large regions of Antarctica (Kreutz and Mayewski, 1999) could also control the density fluctuations that cause isochronal radar reflections in firn. Regardless of the cause, the key issue is the accuracy of tracking the spatial continuity of a single isochrone and, therefore, the accuracy to which these horizons can be used to understand the historical records preserved within the stratigraphy of ice sheets. Despite their use in previous

studies of accumulation rate variability (e.g. Kohler *et al.*, 1997; Richardson *et al.*, 1997; Richardson and Holmlund, 1999; Vaughan *et al.*, 1999b), radar layers have never been dated at multiple locations over long distances to reliably determine their isochronal accuracy. Here, data are presented from a 100-km transect in West Antarctica (Figure 4.13). Along this profile, continuous horizons consisting of single, 35 cm resolution pulses are tracked between dated ice cores collected at sites 00-4 and 00-5. The isochronal accuracy for this particular pulse is <1 year.

4.4.1.1 Simplifying the Radar Pulse

The radar pulse (Figure 4.14a) is a transient, 1.5 cycle waveform lasting about 3.8 ns with a dominant spectral frequency near 400 MHz. In firm of dielectric constant $\epsilon = 2.4$ (typical average value for dry polar firm) this pulse duration provides a layer interface separation resolution of approximately 35 cm. This spacing is generally greater than the separation of annual layers at depth in polar firm. The radar profile discussed here reveals numerous events represented by pulse shapes similar to that in Figure 4.14a, which are most likely responses to one or more closely-spaced thin layers spanning a thickness of 10 cm or less (Arcone *et al.*, 2003). To simplify the appearance of the profile horizons and improve their resolution, the profile was deconvolved (spiked) before applying a Hilbert magnitude transform, as shown in Figure 4.14a. The consistency of the phase structure of this pulse shape before Hilbert transformation of the profile in Figure 4.14b provides evidence that the leading edge of an isochronal event or series of events has been tracked.

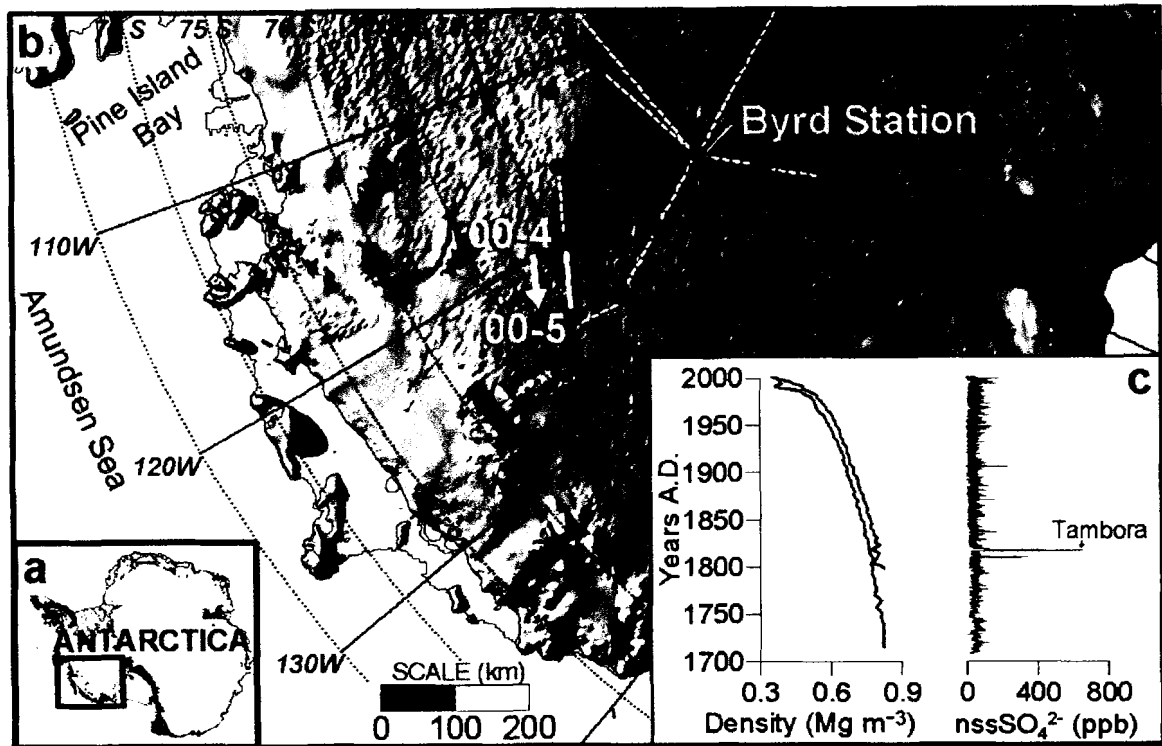


Figure 4.13. Location maps and ice core data. a) Continent-scale map of Antarctica. b) Portion of West Antarctica (boxed region in a) showing some of the US ITASE traverse routes (white lines). Red circles indicate where ice cores were collected. The solid white line represents the transect along which the radar profile was collected between 00-4 and 00-5. The white arrow indicates the direction of travel during data acquisition. The shaded relief map was generated from a digital elevation model (Liu *et al.*, 1999), which was also used to estimate ice flow directions at 00-4 and 00-5 (black arrows). c) Ice core density and chemistry (nssSO_4^{2-}) profiles for 00-4 (blue) and 00-5 (red).

4.4.1.2 Defining the Depth-Age Relationship

Ice cores collected at 00-4 and 00-5, analyzed for soluble major ion content (Dixon *et al.*, 2003) and density, were used to determine the relationship between depth and age at each end of the radar profile. High resolution chemical analysis (30–50 measurements per meter) was used to define each core-chemistry year on the basis of a winter-spring peak in Na^+ , Cl^- , Ca^+ , Mg^{2+} and K^+ , and combined with a spring-summer peak in both NO_3^- and excess non sea salt (nss) SO_4^{2-} (Whitlow *et al.*, 1992; Legrand and Mayewski, 1997). Extreme events, such as the 1815 A.D. Tambora volcanic eruption provide absolute age constraints within each core that are easily identified in nssSO_4^{2-} profiles (Figure 4.13c). The dimensions and mass of individual core sections (~1 m) were measured in the field to develop a density profile for each site (Figure 4.13c).

The round-trip travel time of each returned radar pulse (maximum of 741 ns) was converted to depth using the density profiles and the well-known relationship between firm density and the real part of the dielectric constant, ϵ' , which determines the radio wave velocity, c , through polar firm (e.g. Richardson and Holmlund, 1999). This relationship can be expressed with the empirical equation (Kovacs *et al.*, 1995),

$$\epsilon' = (1 + 0.845\rho_s)^2 \quad 4.1$$

where ρ_s represents the specific gravity (i.e. density relative to that of water). The quantity c is then calculated from:

$$c = c_0 / \sqrt{\epsilon'} \quad 4.2$$

where c_0 is the electromagnetic wave speed through a vacuum. These procedures allow us to plot the depth and age of each ice core sample against its corresponding radar horizon (e.g. Figure 4.14b).

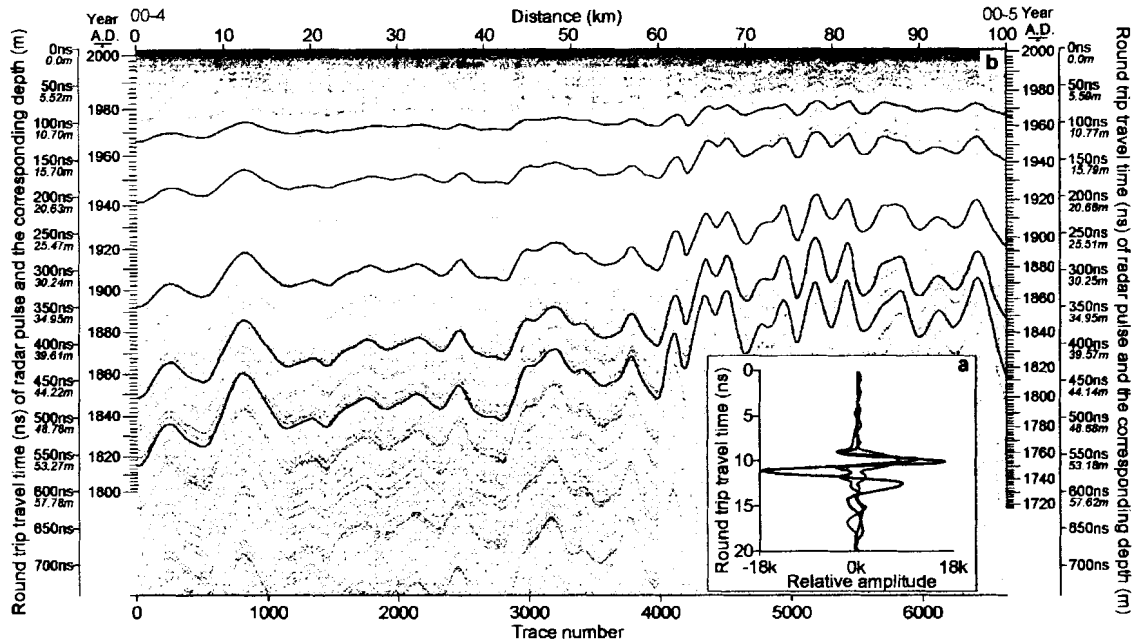


Figure 4.14 Radar data collected between US ITASE sites 00-4 and 00-5. a) 400-MHz pulse shape as reflected by a high-density layer in firn (black line). The pulse was deconvolved with a spiking routine (blue line) before performing a Hilbert magnitude transform (red line). b) Radar profile after deconvolution and Hilbert transformation. The darkened horizons are tracked (black lines) to illustrate isochronal continuity between core sites. The deepest visible horizon at Site 00-4 has been tracked the entire distance (~550 km along-track) to Byrd Station. Signal fading related to surface undulations is apparent beyond 60 km. Round trip travel time (ns) shown on the vertical axes, is also given in meters of depth and was determined from the core density profiles.

4.4.1.3 Tests of Isochronal Accuracy

Five horizons were selected on the basis of their prominence and relative spacing from one another, and have been darkened to show their continuity (Figure 4.14b). Each of these horizons was tested for isochronal accuracy by tracking their leading edge from one dated core to the other. The maximum age difference found for all the horizons tested is <1 year, including the deepest horizon that dates to 1815 A.D. This high degree of isochronal accuracy suggests that there is little or no error induced by layer variations, which is attributed to the trace acquisition rate (~1 trace/15 m), traverse speed (~3 m/s), and stacking rate during data collection. Each of the traces in the final profile represents a stack of approximately 150 traces so that layer variations are well averaged.

It is unlikely that the procedure used for depth calibration introduces any significant error, despite the 1-m core lengths used for density calculations. For example, if the average density of a 1-m core section is 600 kg m^{-3} , the round-trip delay of the radar signal is 10.051 ns. Assuming an exaggerated inhomogeneity of 550 kg m^{-3} for the top half and 650 kg m^{-3} for the bottom half of the core, the error in time delay through each meter of core is only -0.002 ns. The cumulative error at 60 m depth would be 0.12 ns (~1 cm) within the >600 ns record. In addition, it is assumed that the top two meters are at the same density as the third meter (~ 400 kg m^{-3}) because the density profiles generally begin at a depth of 2 m. An actual density of 300 kg m^{-3} for the top two meters would give a time delay error of 1.1 ns (~10 cm), which corresponds to less than one year at a depth of 50 m.

A more likely source of error is related to difficulties in tracking some of the deeper layers in regions where the ice sheet surface undulations are more pronounced.

The continuity of the horizons is most evident within 60 km of site 00-4 (Figure 4.14b), where the ice sheet surface is relatively smooth (Figure 4.15, *top right*). Beyond 60 km, surface undulations affect the local accumulation rate, as noted in previous studies (Black and Budd, 1964; Gow and Rowland, 1965; Whillans, 1975; Mosley-Thompson *et al.*, 1995; Venteris and Whillans, 1998; Vaughan *et al.*, 1999b). The folded appearance of the radar horizons indicates that more snow accumulates in depressions than on hills. As the apparent folding becomes amplified with depth, the incidence angle (stratigraphic dip) between radar pulses and stratigraphic layers increases. An incidence angle of only 0.4 degrees, which is typical for this profile, provides a round-trip phase delay of almost half a wavelength between consecutively recorded traces. Therefore, such a delay reduces return strengths by causing destructive interference which, in turn, makes it more difficult to track an individual horizon. Given this effect, the discernable leading edges that are tracked may represent one of a few closely spaced historical events.

4.4.2 Accumulation Rates from GPR Profiling

The isochronal accuracy of tracking the 400-MHz horizons enables the determination of historical accumulation rates at any point along the profile. Each of the darkened radar horizons in Figure 4.14b was digitized according to trace number (1-6641) and round-trip travel time (0-741 ns). Each trace was post-processed for position and elevation using simultaneously recorded GPS data (Hamilton and Spikes, 2003) that were recorded as the expedition moved across the ice sheet at $\sim 3 \text{ m s}^{-1}$. Maximum uncertainties in the GPS positions never exceed 0.2 m (Hamilton and Spikes, 2003). Based on the time when GPR data collection began (obtained from the kinematic GPS

receiver) and the trace acquisition rate, we estimated the time when each trace was acquired and then we interpolated the GPS data to each of these times. Density profiles for all 6641 traces between the two core sites were estimated using linear interpolation, which is appropriate because the density profiles for each site are similar.

Accumulation rates for each trace were calculated as follows. The interpolated density profiles and round-trip travel times were used to calculate the water equivalent (w.e.) depth to each horizon, which is divided by the age of the horizon in years to yield the time-averaged yearly accumulation rate since that layer was deposited. This calculation was performed for all 6641 traces that make up each of the five horizons (Figure 4.14b) to produce the along-track accumulation rate for each horizon at each trace. A long-term accumulation rate is calculated using the deepest digitized horizon, which corresponds to an age of 1815 A.D. The same calculation scheme is used to calculate accumulation rates for the intervals between consecutive horizons.

The uncertainties associated with each calculated accumulation rate vary with depth. Estimated uncertainties are based on three components: layer thinning due to ice advection (0 at surface, 1 cm at 60 m firm depth), the cumulative uncertainty introduced by our procedure for depth calibration (10 cm at 2 m firm depth, 11 cm at 60 m firm depth), and the isochronal accuracy of each horizon (1 year for all depths). All possible combinations of these uncertainties were used in sensitivity tests to determine how calculated accumulation rates vary with depth. Results indicate that uncertainties at a firm depth of 10 m are ~3.8% of the calculated accumulation rate. The uncertainties decrease to ~0.5% at a firm depth of 60 m. Spatially averaging the calculated accumulation rates further reduces the associated uncertainties.

4.4.2.1 Continuous Versus Point Measurements

Accumulation rates derived from each of the digitized horizons (Figure 4.14) are presented in Figure 4.15 (*center right*). The maximum spatial variability of long-term accumulation rates along this 100-km transect is 32% (std. dev. = 18%), when comparing the range of \bar{b}_r (0.098 to 0.195 m a⁻¹ w.e.) to the profile average of 0.144 m a⁻¹ w.e. (Figure 4.15, *center right*). The standard deviation of accumulation rates from the linear fit in Figure 4.15 (*center right*) is 9%. The radar-derived accumulation rates agree perfectly with the core-derived accumulation rates at core sites 00-4 (0.192 m a⁻¹ w.e.) and 00-5 (0.145 m a⁻¹ w.e.) (Figure 4.15, *left*), because the ice cores are used to calibrate the radar technique. However, the average accumulation rate of 0.169 m a⁻¹ w.e., based on the two ice cores, is 17% higher than the radar-derived average for the 100-km transect. These results are consistent with Richardson *et al.* (1997) and Richardson and Holmlund (1999), who indicate that widely spaced point measurements do not capture the wide range of spatial variability in accumulation rate, nor do they produce an accurate spatial mean.

4.4.2.2 Topographic Influence

The largest component of the spatial variability in accumulation rate (Figure 4.15, *center right*) appears to be related to ice sheet surface topography. The large-scale trend of decreasing accumulation rate (linear fit = -0.07 cm a⁻¹ km⁻¹) may be an orographic effect due to the steady 140 m rise in elevation from 00-4 to 00-5 (gradient = 1.4 m km⁻¹) (Figure 4.15), but it could also be related to geographic differences between the two sites. For example, 00-4 is located on a relatively flat portion of the ice sheet that is within

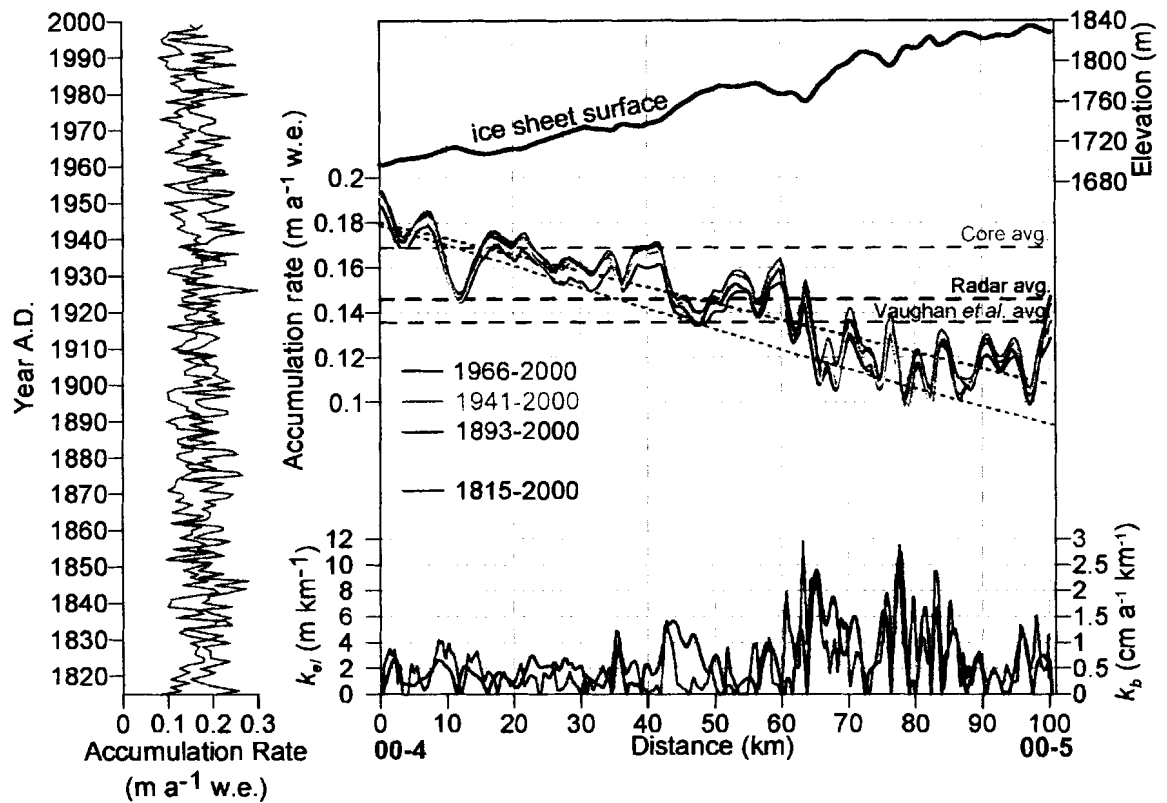


Figure 4.15 Spatial variability of accumulation rates from ice cores and GPR profiling. *Left*: Core-derived annual accumulation rates for 00-4 (orange) and 00-5 (gray). *Top right*: Surface topography. *Center right*: Calculated accumulation rates for each digitized horizon shown in Figure 4.14b (see *legend*). The sloping black line (short dashes) is the fit through the long-term accumulation rates based on the 1815 horizon. The sloping purple line is based on the Vaughan *et al.* (1999) compilation. The mean accumulation rates derived from ice cores (dashed orange line), radar (dashed black line), and the Vaughan *et al.* (1999) compilation (dashed purple line) are labeled accordingly. *Bottom right*: Gradients along the elevation profile (black line) (*top right*) and the 1966-2000 accumulation rate profile (blue line) (*center right*).

20 km of an ice divide, and 00-5 is situated on the leeward flank of an ice ridge that could partially block the supply of moisture from the ocean. Superimposed on the regional trend are local variations in accumulation rate that are related to surface undulations (e.g. Black and Budd, 1964; Gow and Rowland, 1965; Whillans, 1975, Richardson *et al.*, 1997; Richardson and Holmlund, 1999; Vaughan *et al.*, 1999b), which is supported by the observation that local accumulation rates are highest in basins and lowest on peaks (Figure 4.15, *top and center right*).

In Figure 4.15 (*bottom right*), the gradients along the accumulation rate curve, k_b , indicate that accumulation varies by up to $3 \text{ cm a}^{-1} \text{ km}^{-1}$ (std. dev. = $0.55 \text{ cm a}^{-1} \text{ km}^{-1}$) while gradients along the elevation curve, k_{el} , have a maximum of 11 m km^{-1} (std. dev. = 2 m km^{-1}). These gradients were calculated according to changes in each variable measured over a distance of $\sim 150 \text{ m}$ (± 5 traces). Both k_b and k_{el} are presented as absolute values in Figure 4.15 (*bottom right*) to demonstrate the strong correlation between these two variables. The sign of the correlation coefficients in Table 4.1 show that accumulation rate and surface undulations are out of phase when both positive and negative gradients are considered. The k_b curve based on the most recent interval (1966-2000) is presented in Figure 4.15 (*bottom right*), because it has the best correlation with k_{el} (Table 4.1).

The strength of the correlations in Table 4.1 could depend upon the orientation of the radar profile with regard to dominant wind direction. For example, Black and Budd (1964) suggest that the highest accumulation rate should occur on the windward flanks of surface undulations, but their study was nearly parallel with the dominant wind direction. In contrast, our profile is nearly perpendicular to the dominant wind direction, and we

observe the highest accumulation rates near the middle of basins (e.g. Whillans, 1975). However, the orientation of the profile does not explain the reduction in correlation between k_b and k_{el} with increasing interval age (Table 4.1), which is likely related to ice advection, because the older layers were deposited farther up-glacier of the radar transect where the topographic influences are presumably different.

Table 4.1 Correlation between along-track gradients in accumulation rate and surface slope (Figure 4.15, *bottom right*). Negative correlations indicate that large accumulation rates are typically associated with topographic depressions and small accumulation rates are associated with crests/flanks. The correlations are best for the youngest strata, because these have been least affected by advection through a series of undulations.

<i>Interval (Years A.D.)</i>	<i>Correlation coefficient</i>
1815-2000	-0.39
1848-2000	-0.47
1893-2000	-0.49
1941-2000	-0.51
1966-2000	-0.50
1941-1966	-0.42
1893-1941	-0.36
1848-1893	-0.32
1815-1848	-0.26

4.4.2.3 Resolving Climatic Influence

The accumulation rate data in Figure 4.16 reveal that the largest amount of variability is observed on annual time-scales. Because accumulation rates in this region are less than the vertical resolution of our radar system, annual variability must be addressed using the high-resolution ice cores (e.g. Kaspari *et al.*, 2003). The annual accumulation rate at core sites ranges from 5% to 65% (std. dev. = 22%) when calculated

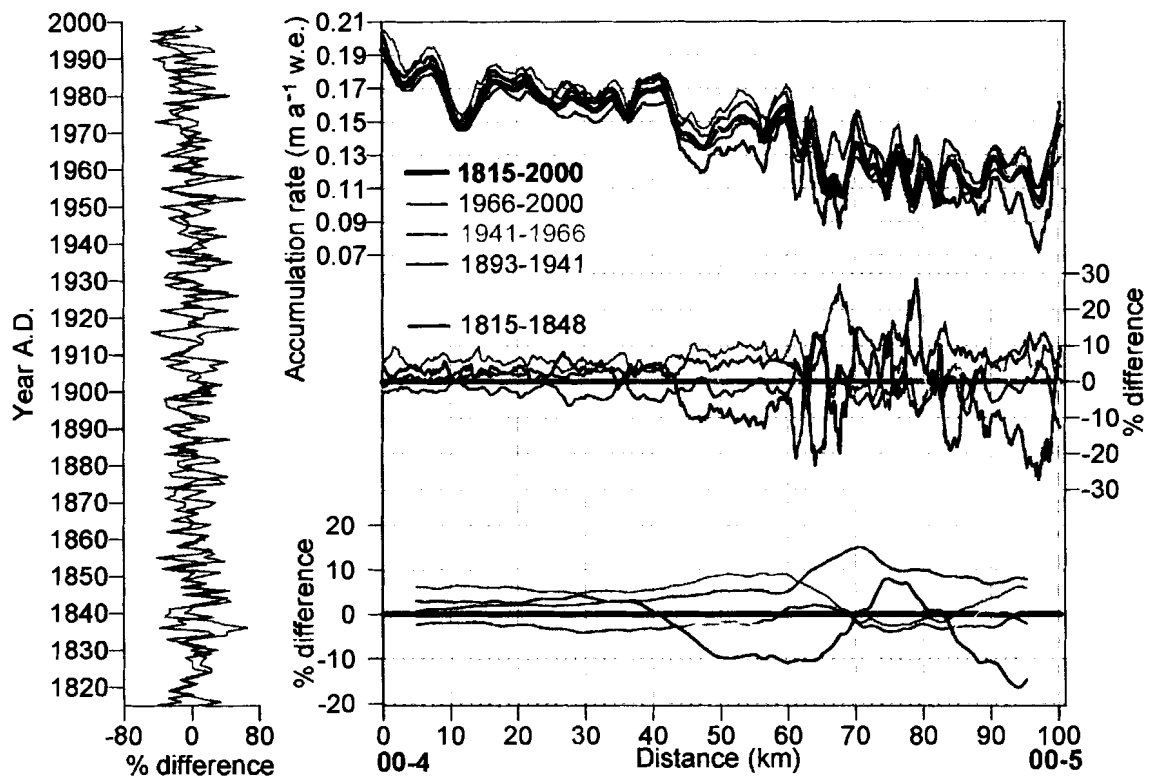


Figure 4.16 Temporal variability in accumulation rates from ice cores and GPR profiling. *Left:* Percent difference from the core-derived average accumulation rates for 00-4 (orange) and 00-5 (gray). *Top right:* Calculated accumulation rates for each interval (see *legend*). The thick black line represents the long-term accumulation rate (1815-2000). *Center right:* Percent difference from the long-term accumulation rates for each horizon (see *legend*). *Bottom right:* Accumulation rate profiles (*center right*) after being smoothed. The 10-km smoothing clips the ends from each profile (see *legend*).

as the percent difference from each core-derived average (Figure 4.16, *left*). This high degree of variability is regarded as significant because it often exceeds 16%, which is the estimated uncertainty introduced by sastrugi (Whillans, 1978; Venteris and Whillans, 1998). Longer-term trends (on the order of decades to centuries) in the annual accumulation rate records related to topography and ice advection have also been considered (Kaspari *et al.*, 2003). These high-resolution records show that annual snowfall rates in this region have decreased since 1970.

Accumulation variability on multi-decadal time-scales (25 to 48 years) is determined for intervals between consecutive radar horizons (Figure 4.16, *top right*). Standard deviations for each of these intervals vary between 14.1 and 21.1% (Table 4.2), and the maximum deviation is 29% (Figure 4.16, *center right*). Percent changes in accumulation rate for each point along-track are determined using the long-term accumulation rate (1815-2000) as a reference interval (Figure 4.16, *center right*). Much of the variability in Figure 4.16 (*center right*) is related to surface undulations and ice flow, which complicates the search for climate signals within each accumulation record.

Table 4.2 Multi-decadal accumulation rates expressed as the 100-km mean for each interval, the percent difference between the interval mean and the long-term regional mean (0.144 m a^{-1}). Each of these means comprises 6641 measurements, which greatly reduces the 2σ uncertainties. The final column is the standard deviation of accumulation rates for each interval, which is calculated relative to the long-term regional mean.

<i>Interval (Years A.D.)</i>	<i>Avg. accumulation rate (m a^{-1} w.e.)</i>	<i>Percent difference (%)</i>	<i>Standard deviation (%)</i>
1966-2000	0.141 ± 0.0016	-2.2 ± 1.2	15.6
1941-1966	0.151 ± 0.0008	5.1 ± 0.6	19.1
1893-1941	0.151 ± 0.0004	5.1 ± 0.34	14.1
1848-1893	0.137 ± 0.0003	$-4.8 \pm .2$	16.8
1815-1848	0.142 ± 0.0002	-1.7 ± 0.16	21.1

A clearer picture of changes related to climate emerges when the short-scale spatial variations are smoothed to length-scales that are comparable to surface undulations, which are generally less than 10 km. Using a 10-km running average, multi-decadal variability identified near 00-4 is found to be consistent over distances of ~50 km (Fig 4, *bottom right*). The smoothed profiles also suggest more variable climate conditions beyond the 50-km mark (Fig 4, *bottom right*), although a portion of the remaining variability may be related to larger-scale topographic, orographic, and geographic effects.

Further isolation of a climate signal may be achieved by calculating the mean accumulation rate for each interval, which also reduces the uncertainties to $<2 \text{ mm a}^{-1}$ w.e. for all intervals (Table 4.2). Table 4.2 shows that typical changes between the means of adjacent intervals are on the order of ~5% ($\sim 0.007 \text{ m a}^{-1}$ w.e.) of the regional mean. The largest increase was 9.9% ($\sim 0.014 \text{ m a}^{-1}$ w.e.) of the regional mean, which occurred between the 1848-1893 (45-years) and 1893-1941 (48-years) intervals. The largest decrease was 7.8% ($\sim 0.011 \text{ m a}^{-1}$ w.e.) of the regional mean, which occurred between the 1941-1966 (25-years) and 1966-2000 (34-years) intervals. This result is consistent with results from the analyses of annual accumulation records (Kaspari *et al.*, 2003), which show that this region has experienced a 2 – 9% (00-4 and 00-5, respectively) decrease in accumulation rate since 1970.

4.4.2.4 Accumulation Rates Near Byrd Station

To determine the spatial distribution of snowfall around Byrd Station, GPR data were collected along three-dimensional survey lines. The parallel lines are separated by

~2 km (Figure 4.17). These GPR data were collected during one of the GPS surveys used to create the high-resolution topographic map of Byrd Station (Figure 4.4).

The continuous GPR profile (Figure 4.18) begins and ends at the same ice core site (Figure 4.17). Each of the traces in this profile represents a stack of approximately 75 traces. The RIDS-C ice core (Kreutz and Mayewski, 1999) provided the depth-age profiles for Figure 4.18. This core was collected in 1995 while the US ITASE GPR survey was conducted in 2002. For the age-depth calibration, the ages from the RIDS-C ice core have been shifted to account for the 7-year difference in the survey times. For example, what used to be the 1995 horizon in the RIDS-C core is now 2002 in Figure 4.18. Errors associated with this shift should not exceed ± 2 years.

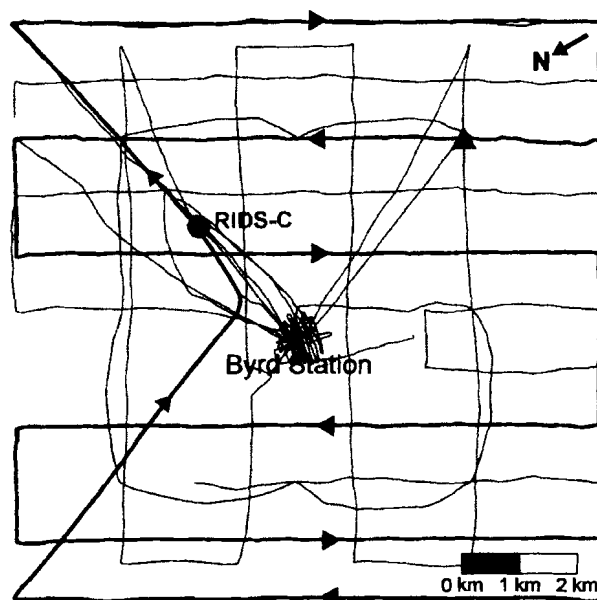


Figure 4.17 Geophysical surveys conducted within the 100-km² grid centered on Byrd Station. Symbols are used to indicate the GPS base station (star), RIDS-C ice core (solid circle), and the Byrd SV station (triangle; Table 2.1). Gray lines indicate GPS surveys. Black lines indicate simultaneous GPS and GPR surveys. Black arrowheads indicate the direction of travel during data collection.

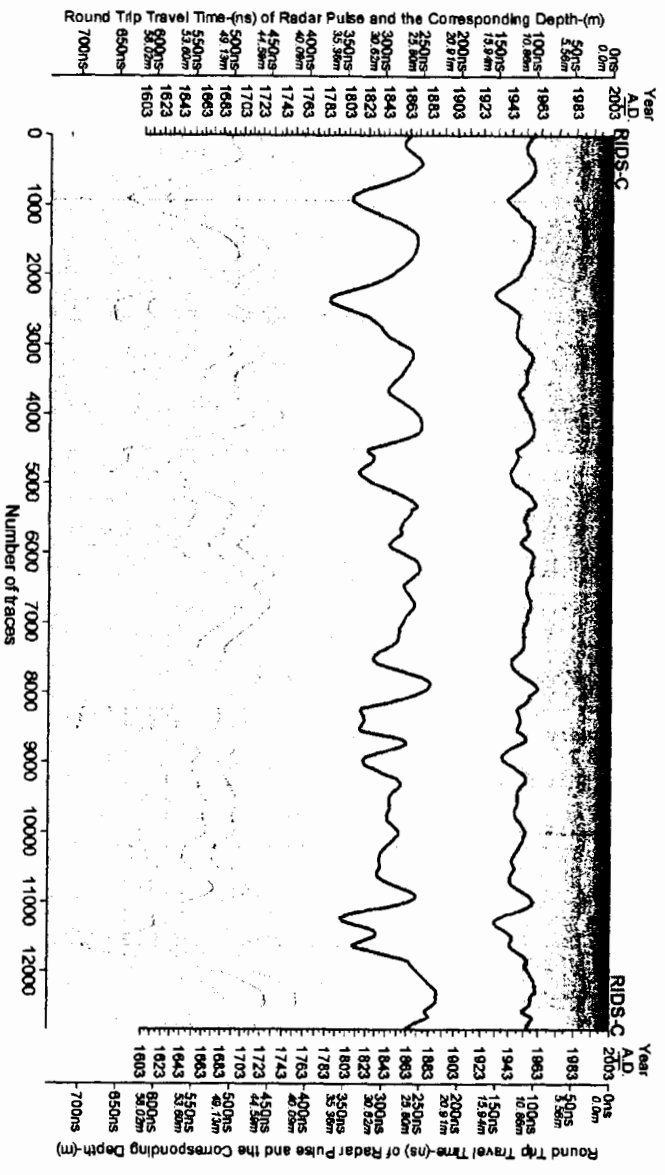


Figure 4.18 Radar profile collected along the three-dimensional survey lines around Byrd Station (Figure 4.17). The depth-age scales on each end of the profile are from the same RIDS-C ice core, and are therefore identical. Each of the darkened horizons (black lines) illustrates isochronal continuity. These horizons are used to calculate accumulation rates (Figure 4.19b).

Two horizons in Figure 4.18 have been traced to illustrate their isochronal continuity. The age of each horizon is exactly the same at both ends of the radar profile. This agreement indicates that the horizons are continuous and isochronal despite any error in the absolute age of each horizon.

The accumulation rates presented in Figure 4.19 are based on the horizons in Figure 4.18 dating to 1957 and 1863 A.D. These horizons were digitized and coupled with GPS and ice core data using the same approach discussed in Chapter 4.4.2. Based on the radar data, accumulation rates near Byrd Station vary between 0.08 – 0.18 m a⁻¹ w.e. (Figure 4.19). The mean accumulation rates for the time intervals examined here are 0.116 m (1863-2003 m a⁻¹ w.e.), 0.127 m a⁻¹ w.e. (1957-2003), and 0.11 m a⁻¹ w.e. (1957-1863). The average for the most recent 46-year interval is ~15% higher than the previous 94-year interval (using 0.116 m a⁻¹ w.e. as a median value).

The map of accumulation rates presented in Figure 4.20 is based on the shallowest horizon in Figure 4.18, which dates to 1957 A.D. Local gradients in snow accumulation can be observed in Figure 4.20a. In other studies (Black and Budd, 1964; Gow and Rowland, 1965; Whillans, 1975), accumulation variability over short distances has been attributed to the interaction of katabatic winds and surface topography. This effect can be seen in Figure 4.20b where the dominant wind direction, and the surface elevation contours have been superimposed over measured accumulation rates. The dominant wind direction and velocity (6.8 m s⁻¹) are the means of measurements recorded every 3-hours over a 5-month period in 1999 by a University of Wisconsin weather station (<http://uwamrc.ssec.wisc.edu/aws>).

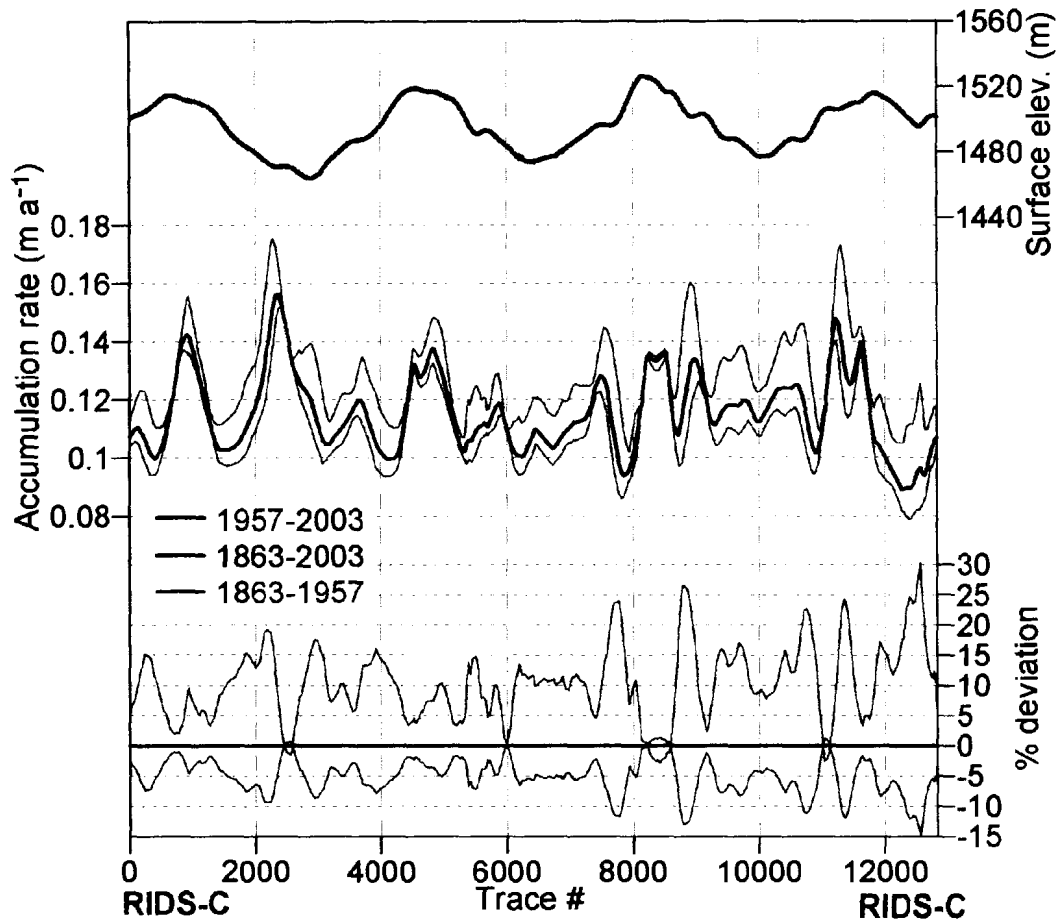


Figure 4.19 Snow accumulation rates from three-dimensional GPR profiling around Byrd Station. *Top*: Surface topography derived from GPS surveys. *Middle*: Accumulation rates derived from the upper two horizons in Figure 4.18. *Bottom*: Changes in accumulation rate through time expressed as the deviation of each interval from a reference interval, which in this case is 1863-2003 A.D.

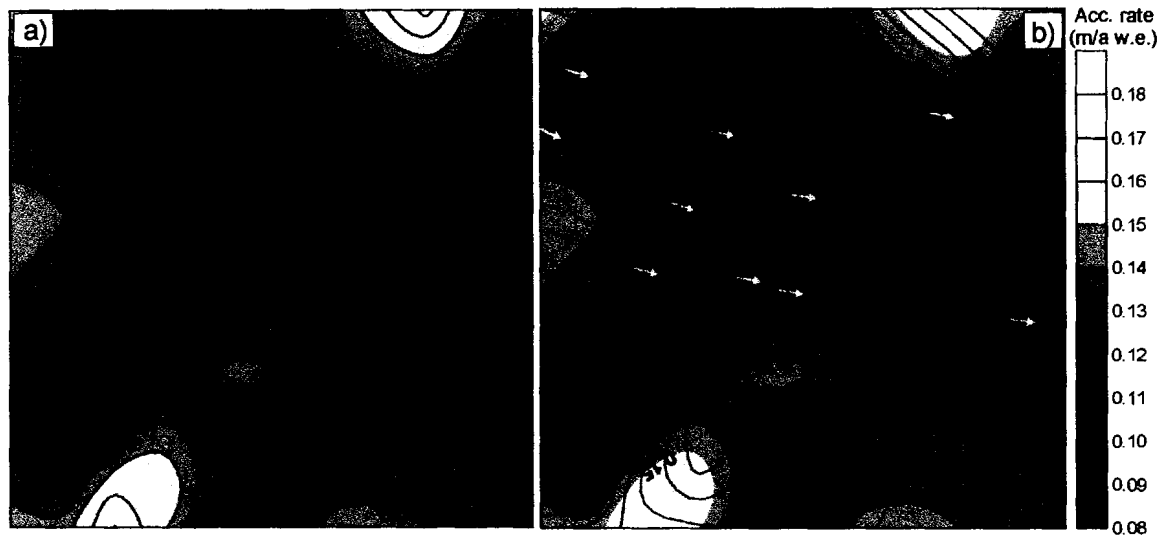


Figure 4.20 Map of accumulation rates for the 100-km² grid centered on Byrd Station. Symbols are used to indicate the GPS base station (star), RIDS-C ice core (solid circle), and the SV station (triangle). a) Gridded version of the accumulation rates presented in Figure 4.19. b) Topography (black contours) from GPS surveys (Figure 4.4) superimposed on map of accumulation rates. The dominant wind direction (green arrow) is based on data from the University of Wisconsin weather station (<http://uwamrc.ssec.wisc.edu/aws>). The yellow arrows are ice velocity vectors (Whillans, 1977; Bindshadler *et al.*, 1997; Hamilton *et al.*, 1998). Accumulation rates are lowest on peaks and down-wind slopes and are highest in valleys and on up-wind slopes.

4.4.3 Tests of a Widely Used Compilation of Antarctic Accumulation Rates

The two most commonly used compilations of Antarctic snow accumulation rates are the Vaughan *et al.* (1999a) (Figure 4.21) and Giovinetto and Zwally (2000) datasets. Each compilation has been used to estimate mass balance for portions of the WAIS (e.g. Joughin and Tulaczyk, 2002; Rignot and Thomas, 2002). Both compilations incorporate low-resolution (~25 km) passive microwave radiometer data, which has been calibrated using ~1,800 point measurements distributed throughout Antarctica. The point measurements are comprised of annual and decadal averages from ice cores and snow pits spanning the 1950s to the 1990s. The resolution of these compilations is too coarse to capture the spatial variations of accumulation rates caused by surface undulations (Richardson *et al.*, 1997; Richardson and Holmlund, 1999), which suggests that these compilations may not be accurate over larger regions. Uncertainties in both compilations are estimated to be $\pm 5\%$ of the reported values (Vaughan *et al.*, 1999a; Giovinetto and Zwally, 2000). Because the two compilations give similar results, only the Vaughan *et al.* (1999a) compilation is evaluated in detail here

Accumulation rates measured with GPR along the traverse from 00-4 to 00-5 (Figure 4.21) and within the 100-km² grid centered on Byrd Station are used for the comparison. The average long-term accumulation rate from the continuous measurements (1815-2001, 0.144 m a⁻¹ w.e., Table 4.2) compares favorably with the Vaughan *et al.* (1999a) average (0.137 m a⁻¹ w.e.) along the 00-4 to 00-5 profile (Figure 4.15, *center right*). The difference between these measurements is ~5%. If the average radar-derived accumulation rate from the most recent interval (1966-2003, 0.141 m a⁻¹ w.e., Table 4.2)

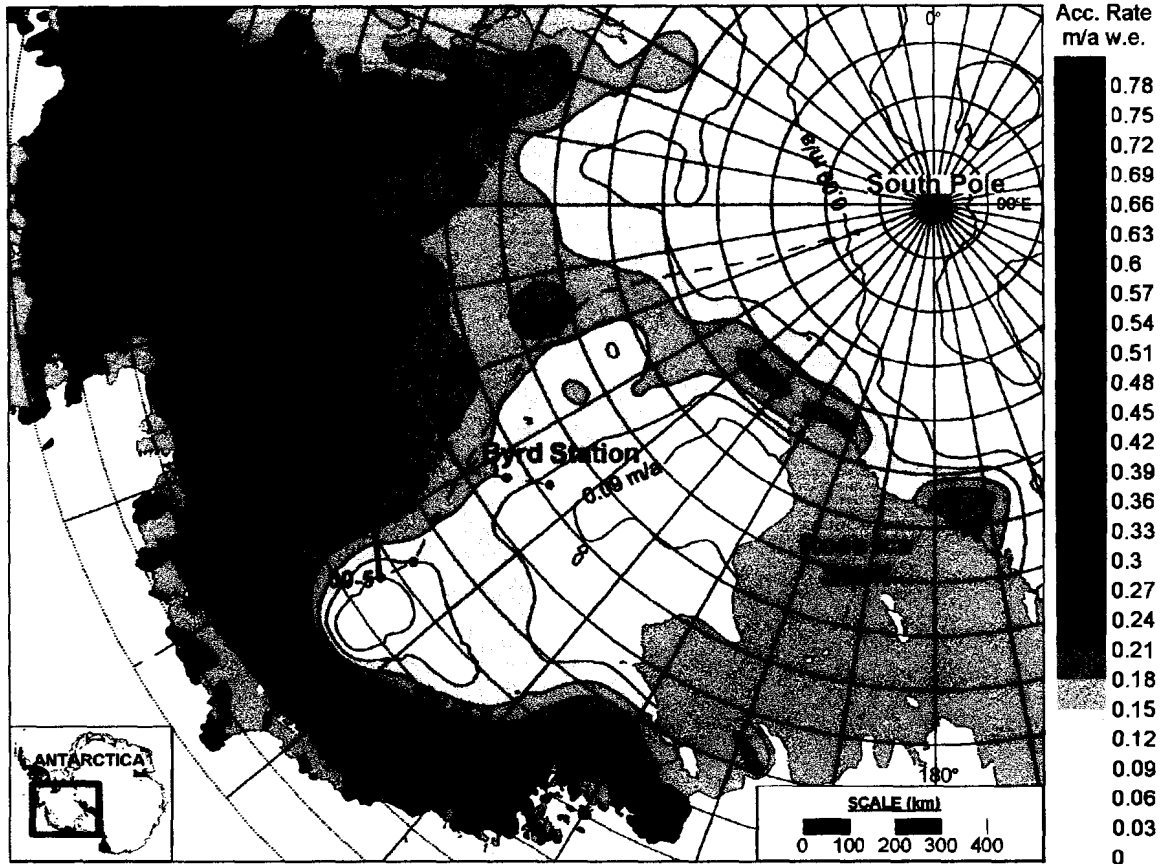


Figure 4.21 West Antarctic accumulation rates from the Vaughan *et al.* (1999a) compilation. Accumulation rates along the transect between 00-4 and 00-5 (thick red line) and at Byrd Station were compared to GPR-derived accumulation rates.

is used, the agreement is slightly better (~3%). At Byrd Station, the Vaughan *et al.* (1999a) compilation gives an accumulation rate of 0.162 m a⁻¹ w.e. (Figure 4.22a), which is ~40% higher than the long-term average from the continuous measurements (1863-2003, 0.116 m a⁻¹ w.e., Figure 4.19). If the average from the more recent time interval (1957-2003, 0.127 m a⁻¹ w.e., Figure 4.19) is used, the average difference between the two datasets is 0.035 m a⁻¹ w.e. or ~28% (Figure 4.22b). It is likely that the agreement between these datasets improves when the more recent time interval is used, because the Vaughan *et al.* (1999a) compilation is comprised of data spanning a similar time period.

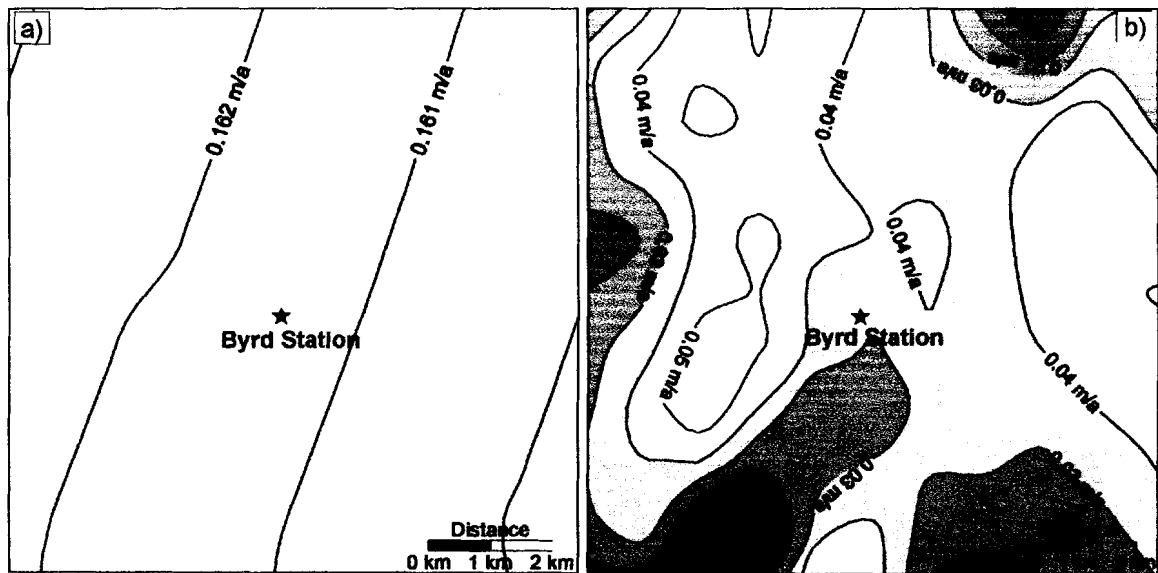


Figure 4.22 Test of the Vaughan *et al.* (1999a) compilation near Byrd Station. a) Accumulation rates at Byrd Station from the Vaughan *et al.* (1999a) compilation. b) Difference between radar-derived accumulation rates at Byrd Station (Figure 4.20a) and the Vaughan *et al.* (1999a) compilation.

4.4.4 Conclusions

Continuous radar profiling along a 100-km transect reveals that accumulation rates on the West Antarctic plateau can vary by up to 3 cm a^{-1} over a distance of 1 km, although they typically vary at a rate of $0.55 \text{ cm a}^{-1} \text{ km}^{-1}$. Wind redistribution of snow around surface undulations is the leading cause of this variability, which is consistent with other studies (e.g. Black and Budd, 1964; Gow and Rowland, 1965; Whillans, 1975; Richardson *et al.*, 1997; Richardson and Holmlund, 1999; Vaughan *et al.*, 1999b). Further characterization of the spatial distribution of snow accumulation on the Antarctic plateau will require additional continuous measurements of the kind presented here.

The three-dimensional map of snow accumulation surrounding Byrd Station provides a useful lesson for those interpreting accumulation rate records from ice cores. This map clearly shows that surface features affect snow deposition rates. Therefore ice that flows through surface features contains both the climatic and ice dynamic accumulation histories of the flow line leading to the drill site. Depending on local ice speeds and the length of the accumulation record, an ice core site might have flowed through one or more surface undulations. Therefore, ice dynamic effects need to be deconvolved from the accumulation rate record before accurate climate interpretations can be made. Measurements of ice flow and topography around drill sites are part of some ice core field programs, but there are numerous archival records that are not accompanied by these field data.

It is evident from these analyses that continent-scale compilations (e.g. Vaughan *et al.*, 1999a) based on widely-space point measurements and satellite remote sensing data do not capture the spatial variability of accumulation rates related to surface

undulations. Over a large distance (100 km), the Vaughan *et al.* (1999a) compilation performed well, producing differences as low as ~3%. Within a small grid (100-km²) the compilation was found to have much larger errors ($\geq 28\%$). These mixed results indicate that the accuracy of this compilation is spatially variable.

These results have different implications for the various approaches to estimating mass balance. For point measurements using the submergence velocity technique, the spatially representative long-term average accumulation rate is required, so topographic influences on core-derived estimates need to be taken into account (Hamilton *et al.*, 1998). For studies that track elevation changes through time using radar or laser altimetry, the effects of short-term temporal (few years) and medium-scale spatial (<20 km) variability in snowfall can introduce large uncertainties, and therefore must be considered when converting measured elevation changes to estimates of ice equivalent thickness change (e.g. Spikes *et al.*, 2003b). For large-scale flux calculations, small errors in basin-wide average accumulation rates contribute large uncertainties, and therefore the full range of accumulation variability within the study region needs to be understood or the error estimates must be scaled accordingly. For the GIS approach used here, the effects of temporal variability may introduce uncertainties when trying to put the calculated changes into a long-term perspective, but spatial variability in snowfall will only introduce error if omitted from the input data.

4.5 Ice Velocity

Ice flow is the remaining key variable in studies of ice sheet mass balance. Ice velocity is used directly in the residual flux calculation (Equation 3.7). The term for the

velocity vector, \bar{U} , represents the depth-averaged velocity, meaning it takes into account any changes in horizontal ice velocity with depth. Equations for calculating the depth-averaged velocity can be found in Hooke (1998) and Paterson (1994). Calculating \bar{U} is difficult however, because horizontal velocity decreases with depth as a result of many factors. These factors include surface slope, ice thickness, ice temperature, crystal orientation, and basal friction. Different combinations of these variables produce different horizontal velocity profiles, and therefore different depth-averaged velocities. The simplest case is when ice velocity at the bed, U_b , is equal to the velocity at the surface, U_s . This situation is commonly observed in areas where there is a lack of basal friction due to the presence of basal water (e.g. Alley *et al.*, 1986; Alley *et al.*, 1987; Engelhardt *et al.*, 1990; Ridley *et al.*, 1993; Engelhardt and Kamb, 1997). The opposite case is when the ice sheet is frozen to the bed, which makes $U_b = 0$.

In this study, depth-averaged velocities are presented for the 100-km² grid centered on Byrd Station. These velocities are estimated using the borehole tilting studies (Garfield and Ueda, 1976; Gow and Williamson, 1976; Whillans, 1979) and surface velocities measured using static GPS surveys (Bindschadler *et al.*, 1997; Hamilton *et al.*, 1998).

4.5.1 Surface Velocities at Byrd Station

Ice surface velocities can be measured using various geophysical approaches including traditional surveying techniques (e.g. Whillans, 1977), static GPS positioning (e.g. Bindschadler *et al.*, 1993; Hamilton *et al.*, 1998), and remote sensing techniques such as feature tracking (e.g. Scambos *et al.*, 1992) and SAR interferometry (e.g. Joughin

et al., 1999; Joughin and Tulaczyk, 2002, Rignot and Thomas, 2002). The largest collection of measured ice velocities available for Antarctica is the VELMAP compilation distributed by the NSIDC (<http://www-nsidc.colorado.edu/data/velmap/>). Unlike the surface topography, ice thickness, and snow accumulation compilations discussed earlier, VELMAP is largely restricted to specific sites in West Antarctica.

Byrd Station is covered in the VELMAP compilation. The data covering Byrd Station consist of ice flow vectors obtained from repeat GPS surveys. These vectors are part of a large strain grid used by Bindschadler *et al.* (1997) to extend the BSSN (Whillans, 1977, 1979) into the tributaries of the Bindschadler Ice Stream (formerly Ice Stream D). Results from both of these strain grids show that ice in this region is longitudinally extensive. However, the measured velocities along the BSSN reach a maximum of 12.7 m a^{-1} at Byrd Station (Whillans, 1977), which is $\sim 1.5 \text{ m a}^{-1}$ faster than velocities from the Bindschadler *et al.* (1997) strain grid and the GPS base station (Chapter 4.2.1) for approximately the same location. The ice flow direction is consistent for all the surveys. The discrepancy in measured velocities may be related to a decrease in ice velocity for this region since the BSSN was surveyed in the 1970s, or it could be error associated with the pre-GPS surveying techniques used to determine ice velocities along the BSSN.

The contoured map of ice surface velocities presented in Figure 4.23 was created using velocities from Bindschadler *et al.* (1997), the SV station at Byrd (Hamilton *et al.*, 1998), and the US ITASE GPS base station. Velocities from the BSSN are not included in this compilation because of the large uncertainties associated with those measurements. Several Bindschadler *et al.* (1997) velocity vectors located just outside of

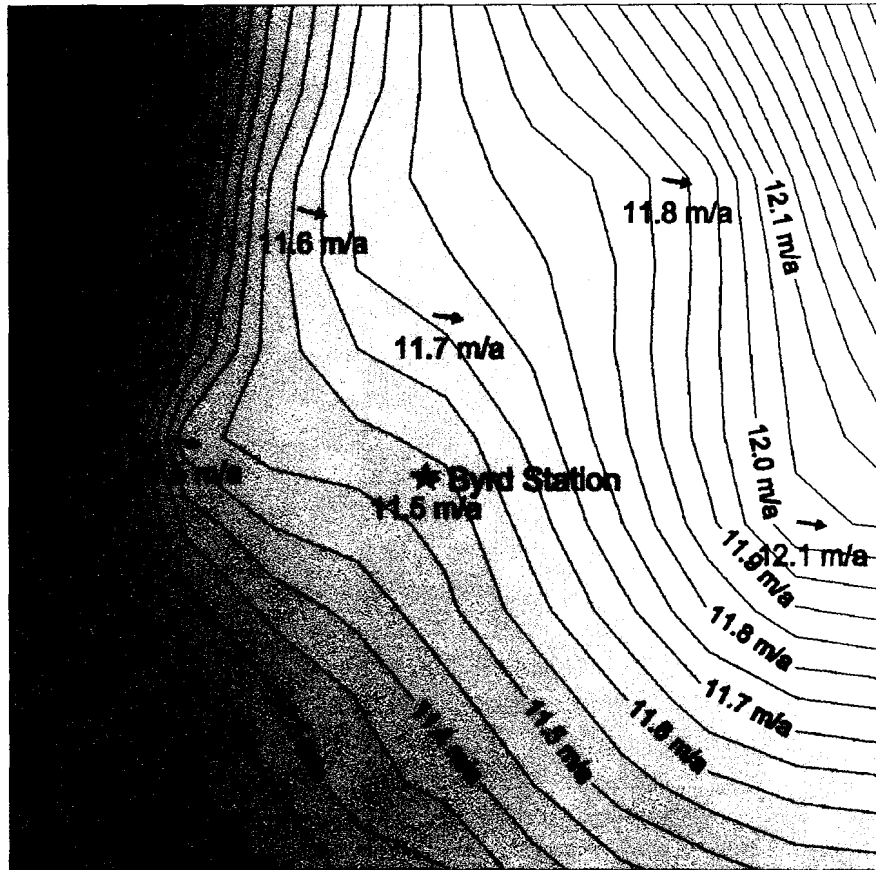


Figure 4.23. Contoured map of ice surface speed for the 100-km² grid centered on Byrd Station. The vectors (blue arrows) are derived from GPS surveys of markers installed on the ice sheet surface (Bindschadler *et al.*, 1997; Hamilton *et al.*, 1998; Hamilton and Spikes, 2003)

the region shown in Figure 4.23 were also considered when producing these contours. Errors for each of these velocity measurements range from 0.01 m a^{-1} (Hamilton *et al.*, 1998; Hamilton and Spikes, 2003) to 0.1 m a^{-1} (Bindschadler *et al.*, 1997). The errors introduced by the interpolation routine are estimated to be $<0.2 \text{ m a}^{-1}$.

The contours and vectors in Figure 4.23 show that ice velocities increase steadily from grid-west to grid-east, although the variable spacing of the contour lines suggest that strain rates within this grid are variable. The most complicated pattern of contours is present in the upper left quadrant of Figure 4.23. In this quadrant, ice velocities increase rapidly for $\sim 3 \text{ km}$, then remain steady for a few km, and eventually return to lower rate of extension. This pattern of velocity change is indicative of ice flow over a bedrock obstacle (e.g. Budd, 1970). The 3-MHz short-pulse radar survey presented in Figure 4.12 shows that there is a bedrock obstacle at precisely this location. The directional components of the vectors presented in Figure 4.23 show that the ice turns toward grid-east at a rate of $\sim 0.5^\circ \text{ km}^{-1}$ as it moves through this grid.

4.5.2 Depth-Averaged Velocities at Byrd Station

Whillans (1979) calculated how the horizontal velocity, U , at Byrd Station changes with depth, z , based on borehole deformation studies by Garfield and Ueda (1976) and Gow and Williamson (1976), so that:

$$U_z = U_s - (U_s \cdot \psi) \quad 4.3$$

where ψ is a shape factor ($\psi = 8 \times 10^{-8} z^2$) based on a linear fit through the borehole tilting measurements.

The velocity profile for each cell in the Byrd Station grid has been calculated using Equation 4.3. The mean of each profile equals the depth-averaged velocity, \bar{U} . An example of one of these profiles is shown in Figure 4.24. This profile shows that the ice sheet is sliding along its bed at a rate of $\sim 7 \text{ m a}^{-1}$ in this region. In Figure 4.24, \bar{U} is $\sim 10 \text{ m a}^{-1}$, which is $\sim 1.5 \text{ m a}^{-1}$ slower than U_s . Whillans (1977, 1979) attributes this internal deformation to the strongly oriented crystal fabric described by Gow and Williamson (1976).

This approach has been used to calculate \bar{U} for each $1 \text{ km} \times 1 \text{ km}$ cell in the Byrd Station grid. These results are presented in Figure 4.25. The general patterns of surface (Figure 4.23), bed (Figure 4.25a), and depth-averaged (Figure 4.25b) velocities are similar in that the fastest velocities are always observed in the upper right of each figure and the slowest velocities are observed in the lower right of each figure. However, the flow field in Figures 4.23 and 4.25 becomes more simplified with depth, suggesting that most of the adjustment in ice velocity is made within the ice column rather than at the bed.

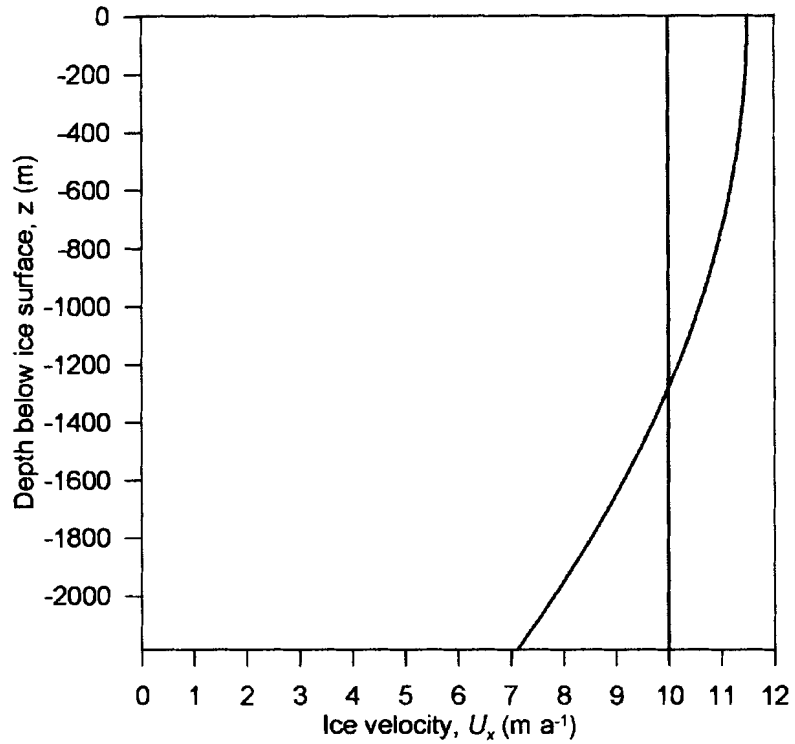


Figure 4.24 The horizontal velocity profile at Byrd Station. The profile shown corresponds with a central grid cell (star in Figure 4.23) where the surface velocity is 11.5 m a^{-1} and the ice thickness is 2184 m. The blue line is the horizontal ice velocity in the principal flow direction at depth z . This curve is a linear fit based on borehole tilting data presented in Whillans (1979).

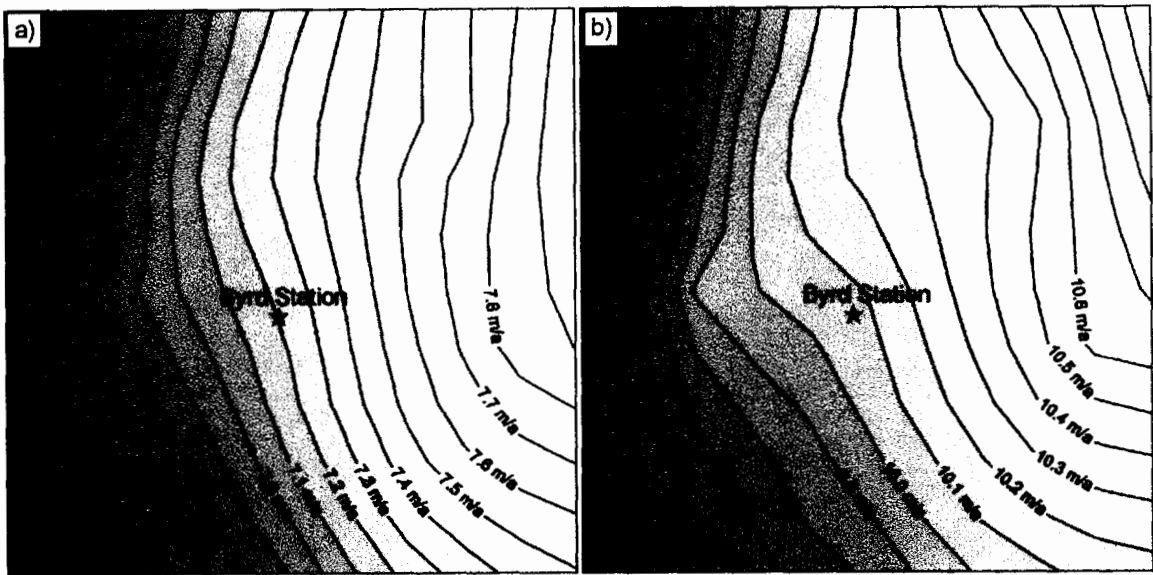


Figure 4.25. Contoured maps of bed (a) and depth-averaged (b) velocities for the 100-km² grid centered on Byrd Station.

Chapter 5

ESTIMATING ICE SHEET MASS BALANCE FOR THE BYRD STATION GRID

5.1 Results

Sufficient data are available to apply the GIS approach to calculate the mass balance of the 100-km² grid centered on Byrd Station using the residual flux calculation (Equation 3.7) and interpret the results. The GIS layers available for this calculation include ice thickness (Figure 4.10b), depth-averaged velocity (Figure 4.25b), and snow accumulation rates from two sources (Figures 4.20a and 4.22a). This calculation is performed twice, once for each set of accumulation rates.

Results from these calculations are illustrated in Figure 5.1. The results obtained using the accumulation rates derived from GPR profiling are shown in Figure 5.1a. The mean value of \dot{H} in Figure 5.1a is +0.009 m a⁻¹. The results produced when using the Vaughan *et al.* (1999a) accumulation rates are presented in Figure 5.1b. The mean value of \dot{H} in Figure 5.1b is +0.045 m a⁻¹. The difference between these mean values is 0.036 m a⁻¹. This result is not surprising, because it directly reflects the measured differences between the accumulation rates derived from GPR profiling and the Vaughan *et al.* (1999a) compilation (Figure 4.22b).

The residual flux calculation was selected for this study because it is capable of resolving the spatial variability of mass balance. Bindschadler *et al.* (1993) describe net thinning of an ice sheet as the result of along-flow increases of ice thickness and velocity,

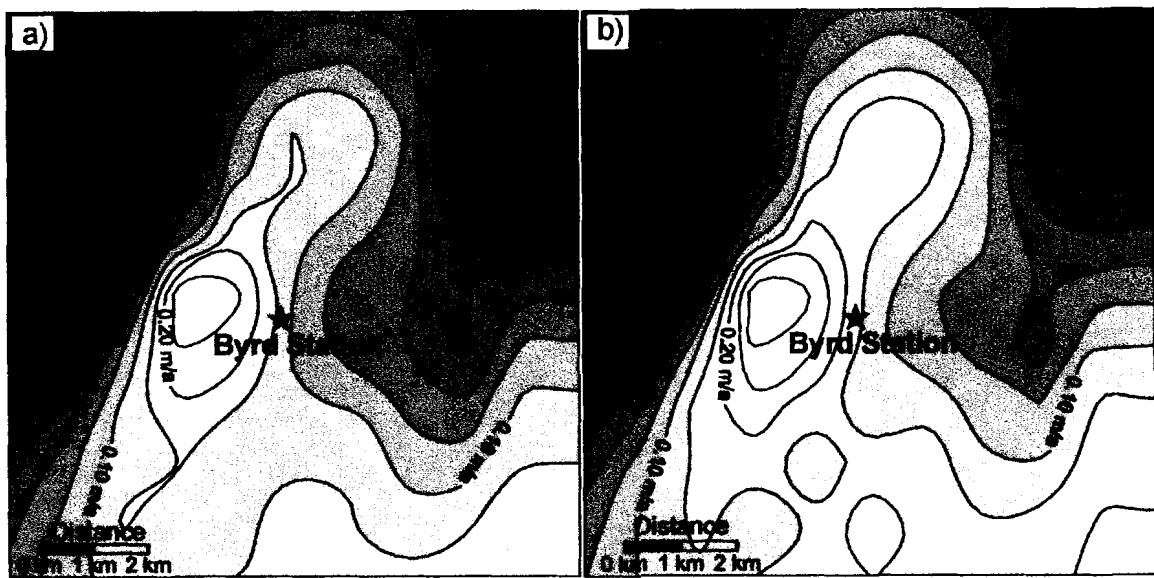


Figure 5.1 Calculated mass balance of the 100-km² grid centered on Byrd Station. a) Mass balance results using the accumulation rates derived from GPR profiling (Figure 4.20a). b) Mass balance results using the accumulation rates from the Vaughan *et al.* (1999a) compilation (Figure 4.22a). Contour interval of \dot{H} in both figures is 0.05 m a⁻¹ of ice equivalent thickness change. Dashed white line indicates locations where $\dot{H} = 0$.

decreases of accumulation rate, or flow divergence. Net thickening could be the result of any of the opposite effects. Net ablation at the ice/bed interface is assumed to have a negligible effect. The results presented in Figure 5.1 show that there is spatial variability in mass balance over short distances. Potential causes of this variability are discussed in Chapter 5.3.

5.2 Error Estimates

The formal errors associated with the mass balance results presented in Figure 5.1 are calculated according to law of propagation of variances (Equation 3.8), which requires error estimates for each variable. The following error estimates are provided for the grid centered on Byrd Station. The average error associated with BEDMAP ice thickness data is ± 74 m (Chapter 4.3.2). The average error of the accumulation rates in the Vaughan *et al.* (1999a) compilation is 0.035 m a^{-1} (Chapter 4.4.3). The errors for individual ice velocity measurements are $<0.1 \text{ m a}^{-1}$ (Hamilton *et al.*, 1998; Bindschadler *et al.*, 1997; Hamilton and Spikes, 2003), but because these data have been interpolated throughout the grid, this estimate is doubled to 0.2 m a^{-1} . Given the estimated accuracy of the core-derived depth-age scale (± 2 years; Chapter 4.4.2.5) and the small errors contributed by variations in the density profile (<1 year; Chapter 4.4.1.3), the maximum errors in the radar-derived accumulation rates are approximately $\sim 0.005 \text{ m a}^{-1}$. And finally, the error of the mean density value (911.7 kg m^{-3}) is expected to be $<0.001 \text{ kg m}^{-3}$, because this quantity is based on density measurements recorded through the entire ice thickness (Gow and Williamson, 1976; Whillans, 1977). Based on these individual error components, the standard error for each grid cell is $\sim 4 \text{ m a}^{-1}$. Because the errors

associated with the ice thickness data are so large and dominant, this formal error is approximately the same for all grid cells, regardless of which accumulation rate is used for the calculation. This formal error estimate represents the overall precision of the calculated results, which provides a useful estimate of the associated uncertainties, but it does not necessarily describe the accuracy of the results presented in Figure 5.1.

One advantage of applying this approach at Byrd Station is that this region is known to be in balance or slowly thinning from previous studies. The continuity study along the Byrd surface strain network (Chapter 2.3) indicated a thinning rate of 0.03 m a^{-1} (Whillans, 1977). The Byrd SV station gives a point mass balance estimate of $-0.004 \pm 0.022 \text{ m a}^{-1}$ (Hamilton *et al.*, 1998). Therefore, the results presented in Figure 5.1 are consistent with the previous estimates of mass balance for this region.

The calculated mean thickness change agrees very well with the SV station when using the accumulation rates derived from GPR profiling (Figure 5.1a). However, the results produced using the Vaughan *et al.* (1999a) accumulation rates are biased towards thickening, because the compilation overestimates thickness in this region. All of the mass balance results discussed here show less thinning than the continuity study, but this discrepancy may be attributed to the fact that the Whillans (1977) study ends at Byrd Station and therefore represents changes that are occurring upglacier.

The SV station also provides the opportunity to check the accuracy of mass balance results for individual grid cells. In Figure 5.2, the location of the SV station corresponds with a grid cell that is thinning at a rate of $\sim 0.05 \text{ m a}^{-1}$. Considering the amount of variability in the calculated mass balance results, this comparison confirms that the approach used here accurately portrays the spatial variability of mass balance.

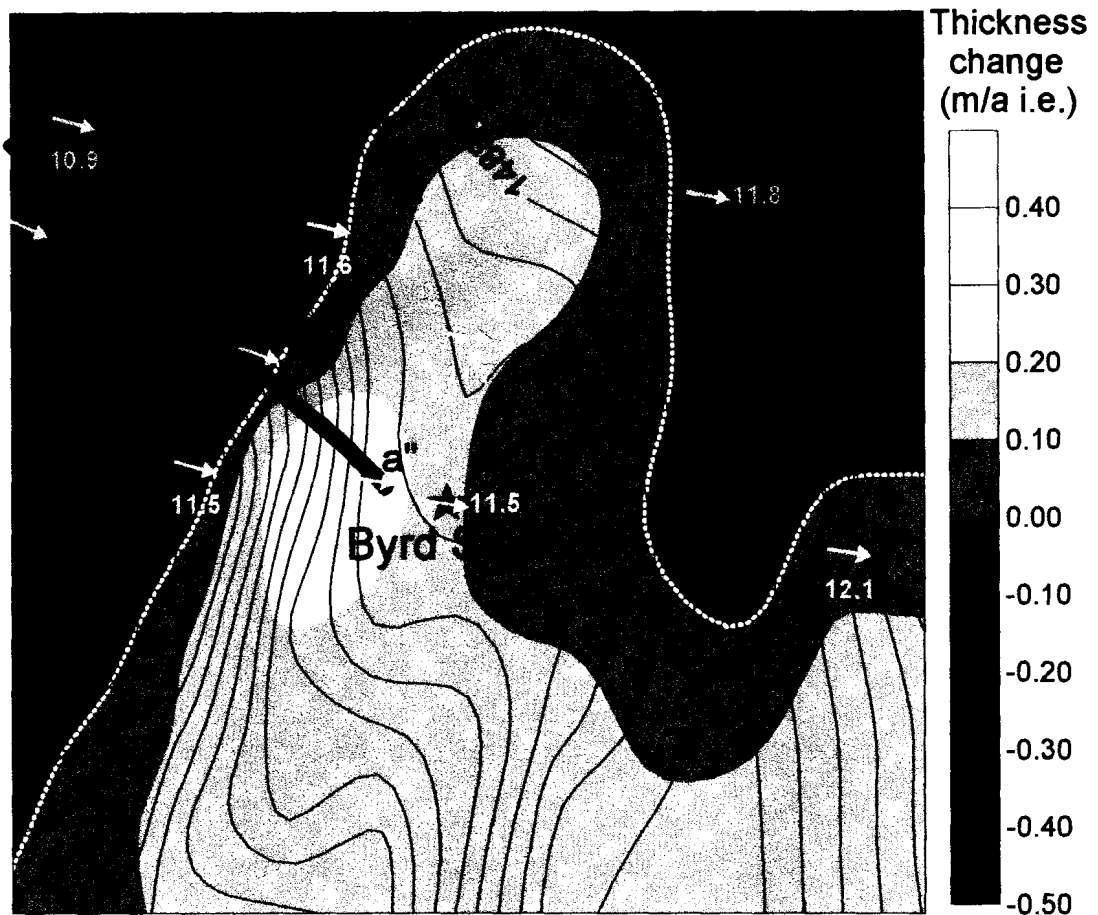


Figure 5.2 Mass balance variables used to interpret thickness change estimates within the 100-km² grid centered on Byrd Station. Ice surface elevation contours (black lines), ice velocity vectors (yellow), a wind vector, and the locations of various points of interest including the Byrd SV station (red triangle) are superimposed on calculated rates of ice sheet thickness change. Dashed white line indicates locations where $\dot{H} = 0$. The black line corresponds with the 3-MHz radar profile $a' - a''$ in Figure 4.12, and is included here for reference.

5.3 Discussion

Each of the anomalies in Figure 5.2 can be attributed to either along-flow changes in ice velocity, accumulation rate, changes in ice thickness, or errors in ice thickness. Conveniently, all of these effects can be observed along 3-MHz radar profile **a' – a''** (Figures 4.10, 4.11, and 4.12). According to measured bedrock elevations (Figure 4.12), ice thickness along this profile increases rapidly in the along-flow direction. This sudden change in ice thickness forces the ice to speed up (Figure 4.23), which increases the rate of extension and leads to thinning. As it reaches the plateau in the bedrock topography (Figure 4.12), it slows down (Figure 4.23), which reduces the rate of extension and causes the ice to thicken. These changes in ice thickness and ice velocity also have an effect on local surface topography (Figure 5.2), which in turn has an effect on snow accumulation rates (Figure 4.20b).

A comparison between the spatial pattern of accumulation rates along profile **a' – a''** (Figure 4.20b) with the spatial pattern of mass balance show that where the ice is thinning most rapidly, the accumulation rates are relatively low, and in areas where the ice is rapidly thickening, accumulation rates are relatively high. However, because the changes in accumulation rate along this profile are relatively small, this effect is somewhat overshadowed by the other effects, including errors in ice thickness estimates.

The effect of ice thickness errors on calculated \dot{H} along profile **a' – a''** is remarkable. Near **a'** the ice thickness estimate from BEDMAP reaches a maximum (Figure 4.12), which corresponds to the cell with the fastest rate of ice sheet thinning (Figure 5.2). Likewise, near **a''** errors in ice thickness estimates from BEDMAP are also large (Figure 4.12). However, at the approximate midpoint along profile **a' – a''**, ice

thickness estimates from BEDMAP and the US ITASE 3-MHz radar survey are nearly the same (Figure 4.12). Now consider how the calculated thickness changes correspond with these errors. Near **a'** ice thickness is underestimated by BEDMAP (Figure 4.12), so there is not enough ice being advected into each grid cell to compensate for the increase in ice velocity (Figure 5.2). Near **a''** ice thickness is overestimated by BEDMAP (Figure 4.12), so there is too much ice being advected into each grid cell, considering the decrease in ice velocity at that point (Figure 5.2). And finally, close to the point where the BEDMAP compilation and the 3-MHz radar profile agree (Figure 4.12), the ice sheet appears to be in balance (Figure 5.2).

5. 4 Applying the Uncertainties to the West Antarctic Ice Sheet

Although there are currently not enough ice velocity measurements to perform the calculation, it is worthwhile examining how the errors in mass balance reported above might propagate if the residual flux calculation were applied to the entire WAIS. Using the average (~240 m) and maximum (>1200 m) uncertainties identified in the BEDMAP compilation (Chapter 4.3.2; Welch and Jacobel, 2003), the formal uncertainties of calculated \dot{H} increase to 31 and 738 m, respectively. These enormous uncertainties reinforce the conclusion that ice thickness compilations need to be improved before they are used in calculations of mass balance using flux-type computation schemes.

It is also useful to extrapolate the uncertainties identified in the Vaughan *et al.* (1999a) compilation beyond the grid at Byrd Station to determine how they might affect other estimates of mass balance. Byrd Station resides within the boundaries of the drainage basin for the Bindschadler Ice Stream. The results described by Joughin and

Tulaczyk (2002) and Rignot and Thomas (2002), which incorporate data from Vaughan *et al.* (1999a), suggest that this entire basin is thickening at a rate of 0.029 m a^{-1} . Given that uncertainties observed in the Vaughan *et al.* (1999a) compilation within the grid at Byrd Station are 0.035 m a^{-1} , and that biases in accumulation rate are transferred directly into mass balance results (Chapter 5.2), this entire basin could actually be thinning. This analysis demonstrates the need for caution in interpreting mass balance results.

Chapter 6

CONCLUSIONS

Several of the measurement techniques presented in this dissertation represent advances in the way ice sheets are studied. One advance is the use of long-baselines for kinematic GPS positioning, which offers the potential for detailed mapping of other remote locations using large separation distances from a reference station. The use of GPR profiling to extend historical accumulation records from ice cores for hundreds of km is a major advance, because other techniques do not reveal how snowfall varies over short distances. The final advance is the simultaneous collection of GPS, GPR, and 3-MHz radar data, which is useful for interpreting how surface topography, snow accumulation, and ice thickness are influenced by one another.

This study is significant because Byrd Station is the only site in Antarctica where detailed measurements of surface elevation and snow accumulation rate have been coupled with measurements of ice velocity, ice thickness, density, and wind direction to calculate and interpret changes in mass balance. The detail in the maps covering Byrd Station make it possible to infer how wind redistributes snow around surface undulations. When interpreting mass balance results, the abundance of data at this site also make it possible to distinguish between the effects of changes in ice velocity and accumulation rate from errors in ice thickness. The results provided valuable insight for issues relating to spatial variability of ice sheet mass balance, and the measurement thereof.

There are many ways to improve the current estimates of WAIS mass balance, but all of them involve additional measurements of the key quantities discussed in this dissertation. Further improvements can be made to the RAMP DEM by incorporating more ground, airborne, and satellite-based measurements of surface elevation, although this might be unnecessary because a higher-resolution, more accurate DEM will be compiled using laser altimeter data from ICESat (Zwally *et al.*, 2002). The most reliable way to improve the BEDMAP compilation is to incorporate more measurements like the US ITASE 3-MHz radar data (Welch and Jacobel, 2003). However, a new method involving the inversion of surface topography derived from a satellite derived digital elevation model (DEM) could potentially be used to improve the BEDMAP compilation. This technique, first discussed in Budd (1970), was used by Fastook *et al.* (1995) to calculate the locations of bedrock peaks and valleys in regions of the fast-flowing Jakobshavns Isbrae, Greenland without any prior knowledge of bedrock topography. The most reliable way to improve continent-scale compilations of accumulation rate is to incorporate continuous measurements from GPR profiling, such as the data presented here. The current compilation of Antarctic ice velocities can be significantly improved by incorporating data derived from satellite-based SAR interferometry and feature tracking. This approach has already been used estimate velocities over large portions of West Antarctica (e.g. Scambos *et al.*, 1992; Joughin *et al.*, 1999; Joughin and Tulaczyk, 2002; Rignot and Thomas, 2002).

The data introduced here are only a small portion of the US ITASE mass balance dataset. Ongoing ice core analyses will produce additional depth-age profiles that can be used to calculate accumulation rates from the remaining GPR profiles. It may take a year

or more to complete this process. When completed, the entire dataset will be incorporated into a new continent-scale compilation of Antarctic accumulation rates. By that time, a more accurate Antarctic surface DEM should have been compiled using GLAS data (Zwally *et al.*, 2002), the ice velocity measurements from interferometric studies (e.g. Joughin *et al.*, 1999; Joughin and Tulaczyk, 2002; Rignot and Thomas, 2002) will be available, and BEDMAP (Lythe *et al.*, 2000) will have been updated with at least the US ITASE 3-MHz radar surveys (Welch and Jacobel, 2003). These improved compilations can then be used to calculate the mass balance of the WAIS with much greater confidence than is currently possible.

REFERENCES

- Alley, R., Blankenship, D., Bentley, C., and Rooney, S., 1986, Deformation of till beneath Ice Stream B, West Antarctica, *Nature*, v. 322, p. 57-59.
- Alley, R., Blankenship, D., Rooney, S., and Bentley, C., 1987, Till beneath Ice Stream B, 3, Till Deformation: Evidence and implications, *Journal of Geophysical Research*, v. 92, p. 8921-8929.
- Alley, R., and Bindschadler, R., 2001, The West Antarctic ice sheet and sea level change. *Antarctic Research Series 77*, American Geophysical Union, Washington, D.C. p.1-11.
- Anandakrishnan, S., Voigt, D.E., Alley, R.B., and King, M.A., 2003, Ice stream D flow speed is strongly modulated by the tide beneath the Ross Ice Shelf, *Geophysical Research Letters*, v. 30, p. 1361.
- Arcone, S.A., Spikes, V.B., Hamilton, G.S., and Mayewski, P.A., 2003, Stratigraphic continuity in 400-MHz short-pulse radar profiles of firn in West Antarctica, *Annals of Glaciology*, v. 39, in press.
- Bamber, J.L., 1994, A digital elevation model of the Antarctic Ice Sheet derived from ERS-1 altimeter data and comparison with terrestrial measurements, *Annals of Glaciology*, v. 20, p. 4854.
- Bindschadler, R., Vornberger, P., and Shabtaie, S., 1993, The detailed net mass balance of the ice plain on Ice Stream B, Antarctica: a geographic information system approach, *Journal of Glaciology*, v. 39, no.133, p. 471-482.
- Bindschadler, R.A., Chen, X., and Vornberger, P.L., 1997, Surface Velocity and Strain Rates at the Onset of Ice Stream D West Antarctica. *Antarctic Journal of the United States*, v. XXXII, no. 5, p. 41-43.
- Bindschadler, R.A., King, M.A., Alley, R.B., Anandakrishnan, S., and Padman, L., 2003, Tidally controlled stick-slip discharge of a West Antarctic ice stream, *Science*, v. 301, no. 5636, p. 1087-1089.
- Black, H.P., and Budd, W., 1964, Accumulation in the region of Wilkes, Wilkes Land, Antarctica, *Journal of Glaciology*, v. 5, p. 3-16.
- Blankenship, D., Morse, D., Finn, C., Bell, R., Peters, M., Kempf, S., Hodge, S., Studinger, M., Behrendt, J., and Brozena, J., 2001, Geologic controls on the initiation of rapid basal motion for West Antarctic Ice Streams: A geophysical perspective including new airborne radar soundings and laser altimetry results, *Antarctic Research Series 77*, American Geophysical Union, Washington, D.C., p. 105-121.

- Budd, W.F., 1970, Ice flow over bedrock perturbations, *Journal of Glaciology*, v. 9, no. 55, p. 29-48.
- Casassa, G., and Whillans, I.M., 1994, Decay of surface topography on the Ross Ice Shelf, Antarctica. *Annals of Glaciology*, v. 20, p. 249-253.
- Christensen, L., Reeh, N., Forsberg, R., Hjelm, J., Skou N., and Woelders, K., 2000, A low-cost glacier-mapping system, *Journal of Glaciology*, v. 46, no. 154, p. 531-537.
- Church, J.A., Gregory, J.M., Huybrechts, P., Kuhn, M., Lambeck, K., Nhuan, M.T., Qin, D., and Woodworth, P.L., 2001, *Climate change 2001: The scientific basis*. Intergovernmental Panel on Climate Change, Cambridge University Press, UK, p. 359-405.
- Csatho, B., Schenk, T., Thomas R., and Krabill, W., 1996, Remote sensing of polar regions using laser altimetry, *International Archives of Photogrammetry and Remote Sensing*. v. XXXI, no. B1, p. 42-47.
- Cuffey, K., 2001, Interannual variability of elevation on the Greenland ice sheet: effects of firn densification, and establishment of a multi-century benchmark. *Journal of Glaciology*, v. 47, no. 158, p. 369-377.
- Davis, C.H., and Moore, R.K., 1993, Combined surface- and volume-scattering model for ice sheet radar altimetry, *Journal of Glaciology*, v. 39, no. 133, p. 675-686.
- Dixon, D.A., Mayewski, P.A., Kaspari, S., Sneed S., and Handley, M., 2003, 200-year sub-annual record of sulfate in West Antarctica, from 16 ice cores, *Annals of Glaciology*, v. 39, in press.
- Eisen, O., Wilhelms, F., Nixdorf, U., and Miller, H., 2003a, Identifying isochrones in GPR profiles from DEP-based forward modeling, *Annals of Glaciology*, v. 37, in press.
- Eisen, O., Wilhelms, F., Nixdorf, U., and Miller, H., 2003b, Revealing the nature of radar reflections in ice: DEP-based FDTD forward modeling, *Geophysical Research Letters*, v. 30, no. 5, p. 1218-1221.
- Engelhardt, H., Humphrey, N., Kamb, B., and Fahnestock, M., 1990, Physical conditions at the base of a fast moving Antarctic ice stream, *Science*, v. 248, no. 4951, p. 57-59.
- Engelhardt, H., and Kamb, B., 1997, Basal hydraulic system of a West Antarctic ice stream: Constraints from borehole observations, *Journal of Glaciology*, v. 43, no. 144, p. 207-230.

- Fastook, J.L., Brecher, H.H., and Hughes, T.J., 1995, Derived bedrock elevations, strain rates, and stresses from measured surface elevations and velocities: Jakobshavns Isbrae, Greenland, *Journal of Glaciology*, v. 41, no. 137, p. 161-173.
- Fricker, H.A., Hyland, G., Coleman, R., and Young, N.W., 2000, Digital elevation models for the Lambert Glacier–Amery Ice Shelf system, East Antarctica, from ERS-1 satellite radar altimetry, *Journal of Glaciology*, v. 46, no. 155, p. 553-560.
- Fujita S., Maeno, H., Uratsuka, S., Furukawa, T., Mae, S., Fujii, Y., and Watanabe, O., 1999, Nature of radio-echo layering in the Antarctic ice sheet detected by a two-frequency experiment, *Journal of Geophysical Research*, v. 104, no. B6, p. 13013-13124.
- Garfield, D.E., and Ueda, H.T., 1976, Resurvey of the Byrd Station, Antarctica drill hole. *Journal of Glaciology*, v. 17, no. 75, p. 29-34.
- Garvin, J., and Williams, R., 1993, Geodetic airborne laser altimetry of Breidamerkurjökull and Skeidarárjökull, Iceland, and Jakobshavns Isbræ, West Greenland, *Annals of Glaciology*, v. 17, p. 379-385.
- Giovinetto, M., and Zwally, J., 2000, Spatial distribution of net surface accumulation on the Antarctic ice sheet, *Annals of Glaciology*, v. 31, no. 171, p. 171-178.
- Gow, A. J., and Rowland, R., 1965, On the relationship of snow accumulation to surface topography at “Byrd Station,” Antarctica, *Journal of Glaciology*, v. 5, no. 42, p. 843-847.
- Gow, A.J., and Williamson, T.C., 1976, Rheological implications of the internal structure and crystal fabrics of the West Antarctic ice sheet as revealed by deep core drilling at Byrd Station, *Geological Society of America Bulletin*, v. 87, no. 12, p. 1665-1667.
- Hamilton, G.S., Whillans, I.M., and Morgan, P., 1998, First point measurements of ice sheet thickness changes in Antarctica, *Annals of Glaciology*, v. 27, p. 125-129.
- Hamilton, G.S., 2002. Mass balance and accumulation rate across Siple Dome, West Antarctica, *Annals of Glaciology*, v. 35, p. 102-106.
- Hamilton, G.S., and Spikes, V.B., 2003, Assessing the performance of a satellite-altimeter derived digital elevation model of Antarctica using precise kinematic GPS profiling, *Global and Planetary Change*, in press.
- Hooke, R., 1998, *Principles of Glacier Mechanics*, Prentice Hall, New Jersey, p. 48-50.
- Hulbe, T., and Whillans, I., 1994, A method for determining ice thickness change at remote locations using GPS, *Annals of Glaciology*, v. 20, p. 263-268.

- Isaaks, E.H., and Srivastava, R.M., 1989, *An Introduction to Applied Geostatistics*, Oxford University Press, New York, p. 561.
- Jacobs, S., 1992, Is the Antarctic Ice Sheet growing, *Nature*, v. 360, p. 29-32.
- James, T., and Ivins, E., 1998, Predictions of Antarctic crustal motions driven by present-day ice sheet evolution and by isostatic memory of the last glacial maximum, *Journal of Geophysical Research*, v. 103, no. B3, p. 4993-5017.
- Jezeq, K.C., 1999, Glaciological properties of the Antarctic Ice Sheet from RADARSAT-1 synthetic aperture radar imagery, *Annals of Glaciology*, v. 29, p. 286-290.
- Jezeq, K.C., Liu, H., Zhao, Z., and Li, B., 1999, Improving a digital elevation model of Antarctica using radar remote sensing and GIS techniques, *Polar Geography*, v. 23, no. 3, p. 185-200.
- Joughin, I., Gray, L., Bindschadler, R., Price, S., Morse, D., Hulbe, C., Karim, M., and Werner, C., 1999, Tributaries of West Antarctic ice streams by RADARSAT interferometry, *Science*, v. 286, no. 5438, p. 283-286.
- Joughin, I., and Tulaczyk, S., 2002, Positive mass balance of the Ross Ice Streams, *Science*, v. 295, no. 5554, p. 476-480.
- Kanagaratnam, P., Gogineni, S.P., Gundestrup, N., and Larsen, L., 2001, High-resolution radar mapping of internal layers at NGRIP, *Journal of Geophysical Research*, v. 106, no. D24, p. 33,799-33,811.
- Kaspari, S., Mayewski, P.A., Dixon, D.A., Spikes, V.B., Sneed, S.B., Handley, M.J., Hamilton, G.S., 2003, Climate variability in West Antarctica derived from annual accumulation rate records from ITASE firn/ice cores, *Annals of Glaciology*, v. 39, in press.
- Kohler, J., Moore, J., Kennett, M., Engeset, R., and Elvehøy, H., 1997, Using ground-penetrating radar to image previous years' summer surfaces for mass balance measurements, *Annals of Glaciology*, v. 24, p. 355-360.
- Kostecka, J.M., and Whillans, I.M., 1988, Mass balance along two transects of the west side of the Greenland ice sheet, *Journal of Glaciology*, v. 34, no. 116, p. 31-39.
- Kovacs, A., Gow, A.J., and Morey, R., 1995, A reassessment of the in-situ dielectric constant of polar firn, CRREL Report 93-26, 22 p., U. S. Army ERDC Cold Regions Research and Engineering Laboratory, Hanover, NH.
- Krabill, W., Thomas, R., Martin, C., Swift, R., and Frederick, E., 1995, Accuracy of airborne laser altimetry over the Greenland ice sheet, *International Journal of Remote Sensing*, v. 16, no. 7, p. 1211-1222.

- Krabill, W., Frederick, E., Manizade, S., Martin, C., Sonntag, J., Swift, R., Thomas, R., Wright, W., and Yungel, J., 1999, Rapid thinning of parts of the southern Greenland ice sheet, *Science*, v. 283, p. 1522-1524.
- Krabill, W., Abdalati, W., Frederick, E., Manizade, S., Martin, C., Sonntag, J., Swift, R., Thomas, R., Wright, W., and Yungel, J., 2000, Greenland Ice Sheet: High-Elevation Balance and Peripheral Thinning, *Science*, v. 21, p. 428-430.
- Kreutz, K.J., and Mayewski, P.A., 1999, Spatial variability of Antarctic surface snow glaciochemistry: Implications for paleoatmospheric circulation reconstructions, *Antarctic Science*, v. 11, no. 1, p. 105-118.
- Kreutz, K.J., Mayewski, P.A., Meeker, L.D., Twickler, M.S., and Whitlow, S.I., 2000, The effect of spatial and temporal accumulation rate variability in West Antarctica on soluble ion deposition, *Geophysical Research Letters*, v. 27, no. 16, p. 2517-2520.
- Legrand, M., and Mayewski, P.A., 1997, Glaciochemistry of polar ice cores: A review, *Reviews of Geophysics*, v. 35, p. 219-243.
- Liu, H., Jezek K., and Li, B., 1999, Development of an Antarctic digital elevation model by integrating cartographic and remotely sensed data: A geographic information system based approach, *Journal of Geophysical Research*, v. 104, no. 10, p. 23199-23213.
- Lythe, M.B., Vaughan, D.G., and the BEDMAP Consortium, 2000, BEDMAP - bed topography of the Antarctic. 1:10,000,000 scale map. BAS (Misc) 9. Cambridge, British Antarctic Survey.
- Mayewski, P.A., 2003. Antarctic oversnow traverse-based southern hemisphere climate reconstruction, *Eos (Transactions of the American Geophysical Union)*, v. 84, no. 22, p. 205-210.
- McConnell, J.R., Arthern, R. J., Mosley-Thompson, E., Davis, C.H., Bales, R.C., Thomas, R., Burkhard, J.F., and Kyne, J.D., 2000, Changes in Greenland ice sheet elevation attributed primarily to snow accumulation variability, *Nature*, v. 406, p. 877-879.
- Mosley-Thompson, E., Thompson, L.G., Paskievitch, J.F., Pourchet, M., Gow, A.J., Davis, M.E., and Kleinman, J., 1995, Recent increase in south pole snow accumulation. *Annals of Glaciology*, v. 21, p. 131-138.
- Parish, T., and Bromwich, D., 1987, Surface windfield over the Antarctic Ice Sheet. *Nature*, v. 328, no. 6125, p. 51-54.

- Paterson, W.S.B., 1994, *Physics of glaciers* (3rd ed.), New York, Pergamon Press, p. 206-210, 251, 255.
- Phillips, H.A., Hyland, G., Morgan, P.J., Coleman, R., and Young, N.W., 1997, Comparison of ERS altimeter and GPS heights on the Amery Ice Shelf, East Antarctica, Proceedings of the 3rd ERS scientific symposium, Florence, 17-21 March 1997, ESA Publication ESA SP-414, v. 2, p. 899-904.
- Price, S., and Whillans, I., 2001, Crevasse patterns at the onset to Ice Stream B, West Antarctica, *Journal of Glaciology*, v. 47, no. 156, p. 29-36.
- Retzlaff, R., and Bentley, C., 1993, Timing of stagnation of Ice Stream C, West Antarctica, from short-pulse radar studies of buried surface crevasses, *Journal of Glaciology*, v. 39, no. 133, p. 553-561.
- Retzlaff, R., Lord, N., and Bentley, C., 1993, Airborne-radar studies: Ice Streams A, B and C, West Antarctica, *Journal of Glaciology*, v. 39, no. 133, p. 495-506.
- Richardson, C., Aarholt, E., Hamran, S.E., Holmlund, P., and Isaksson, E., 1997, Spatial distribution of snow in western Dronning Maud Land, East Antarctica, mapped by a ground-based snow radar, *Journal of Geophysical Research*, v. 102, no. B9, p. 20,343-20,353.
- Richardson, C., and Holmlund, P., 1999, Spatial variability at shallow snow-layer depths in central Dronning Maud Land, East Antarctica, *Annals of Glaciology*, v. 29, p. 10-16.
- Ridley, J.K., Cudlip, W., and Laxon, S.W., 1993, Identification of subglacial lakes using the ERS-1 radar altimeter, *Journal of Glaciology*, v. 39, p. 625-634.
- Rignot, E., and Thomas, R.H., 2002, Mass balance of polar ice sheets, *Science*, v. 297, p. 1502-1506.
- Scambos, T.A., and Haran, T., 2002, An image-enhanced DEM of the Greenland Ice Sheet, *Annals of Glaciology*, v. 34, p. 291-298.
- Shabtaie, S., and Bentley, C., 1987, West Antarctic ice streams draining into the Ross Ice Shelf: configuration and mass balance, *Journal of Geophysical Research*, v. 92, no. 2, p. 1311-1336.
- Shepherd, A., Wingham, D.J., and Mansley, J.A.D., 2002, Inland thinning of the Amundsen Sea sector, West Antarctica, *Geophysical Research Letters*, v. 29, no. 10, doi:10.1029/2001GL0141873.

- Spikes, V.B., Csatho, B., Hamilton, G.S., and Whillans, I.M., 2003a. Thickness changes on Whillans Ice Stream and Ice Stream C, West Antarctica, derived from laser altimeter measurements, *Journal of Glaciology*, v. 49, no. 165, in press.
- Spikes, V.B., Csatho, B., and Whillans, I., 2003b, Laser profiling over West Antarctic ice streams: methods and accuracy, *Journal of Glaciology*, v. 49, no. 165, in press.
- Spikes, V.B., Hamilton, G.S., Arcone, S.A., Kaspari, S., and Mayewski, P., 2003c, Variability in Accumulation Rates from GPR Profiling on the West Antarctic Plateau, *Annals of Glaciology*, v. 39, in press.
- Spikes, V.B., and Hamilton, G.S., 2003, GLAS calibration-validation sites established on the West Antarctic Ice Sheet. *International Archives on Remote Sensing of the Environment*, Honolulu, HI, in press.
- Thomas, R.H., 1976, Thickening of the Ross Ice Shelf and equilibrium state of the West Antarctic ice sheet, *Nature*, v. 259, no. 5540, p. 180-183.
- Thomas, R.H., 1979, The dynamics of marine ice sheets, *Journal of Glaciology*, v. 24, no. 90, p. 167-177.
- Tzengo, R., Bromwich, D.H., and Parish, T.R., 1993, Present-day Antarctic climatology of the NCAR community climate model version 1, *Journal of Climate*, v. 6, no. 2, p. 205-226.
- Van der Veen, C.J., 1993, Interpretation of short-term ice-sheet elevation changes inferred from satellite altimetry, *Climatic Change*, v. 23, no. 4, p. 383-405.
- Van der Veen, C., and Bolzan, J. 1999, Interannual variability in net accumulation on the Greenland ice sheet: observations and implications for mass balance measurements. *Journal of Geophysical Research*, v. 104, no. D2, p. 2009-2014.
- Vaughan, D.G., Bamber, J.L., Giovinetto, M., Russell, J., and Cooper, A.P., 1999a, Reassessment of net surface mass balance in Antarctica, *Journal of Climate*, v. 12, p. 933-946.
- Vaughan, D.G., Corr, H.F., Doake, C.S., and Waddington, E.D., 1999b, Distortion of isochronous layers in ice revealed by ground-penetrating radar, *Nature*, v. 398, p. 323-326.
- Venteris, E., and Whillans, I., 1998, Variability of accumulation rate in the catchments of Ice Streams B, C, D, and E, Antarctica, *Annals of Glaciology*, v. 27, p. 227-230.
- Welch, B.C., and Jacobel, R.W., 2003, Analysis of deep-penetrating radar surveys of West Antarctica, US-ITASE 2001, *Geophysical Research Letters*, v. 30, no. 8, p. 1444.

- Whillans, I.M., 1975, Effect of inversion winds on topographic detail and mass balance on inland ice sheets, *Journal of Glaciology*, v. 14, no. 70, p. 85-90.
- Whillans, I.M., 1977, The equation of continuity and its application to the ice sheet near Byrd Station, Antarctica, *Journal of Glaciology*, v. 18, no. 80, p. 359-371.
- Whillans, I.M., 1978, Surface mass-balance variability near Byrd Station, Antarctica, and its importance to ice core stratigraphy, *Journal of Glaciology*, v. 20, no. 83, p. 301-310.
- Whillans, I.M., 1979, Ice flow along the Byrd Station strain network, Antarctica, *Journal of Glaciology*, v. 24, no. 90, p. 15-28.
- Whillans, I., and Bindshadler, R., 1988, Mass balance of Ice Stream B, West Antarctica, *Annals of Glaciology*, v. 11, p. 187-193.
- Whillans, I., and Van der Veen, C.J., 1993, New and improved determinations of velocity of Ice Streams B and C, West Antarctica, *Journal of Glaciology*, v. 39, no. 133, p. 483-490.
- Whitlow, S., Mayewski, P.A., and Dibb, J.E., 1992, A comparison of major chemical species input timing and accumulation at South Pole and Summit Greenland, *Atmospheric Environment*, v. 26A, no. 11, p. 2045-2054.
- Wingham, D.J., Ridout, A.J., Scharro, R., Arthern, R.J., and Shum, C.K., 1998, Antarctic elevation change from 1992 to 1996, *Science*, v. 282, p. 456-458.
- Wingham, D.J., 2000, Small fluctuations in the density and thickness of a dry firn column, *Journal of Glaciology*, v. 46, no. 154, p. 399-411.
- Zumberge, J.F., Heflin, M.B., Jefferson, D.C., Watkins, M.M., and Webb, F.H., 1997, Precise point positioning for the efficient and robust analysis of GPS data from large networks, *Journal of Geophysical Research*, v. 102, p. 5005-5017.
- Zwally, H.J., Schutz, B., Abdalati, W., Abshire, J., Bentley, C., Brenner, A., Bufton, J., Dezio, J., Hancock, D., Harding, D., Herring, T., Minster, B., Quinn, K., Palm, S., Spinhirne, J., and Thomas, R.H., 2002, ICESat's laser measurements of polar ice, atmosphere, ocean, and land, *Journal of Geodynamics*, v. 34, no. 3-4, p. 405-445.

BIOGRAPHY OF THE AUTHOR

Vandy Blue Spikes was born in Lakin, Kansas on January 4, 1975. He spent most of his formative years in western Kansas, although he also resided in eastern Colorado and northeastern Oklahoma. He graduated from Garden City High School in 1993. In 1997, he received a Bachelor of Science degree in Earth Science from Emporia State University. Blue was first introduced to the field of Glaciology while working at the Byrd Polar Research Center in Columbus, Ohio. In 2000, he received a Master of Science degree in Geology from the Ohio State University. Since the beginning of 2001, Blue has been working as a research assistant for the Climate Change Institute at the University of Maine.

After completing graduate school, Blue will begin his own consulting business on the south shores of Lake Tahoe, CA/NV. Blue is a candidate for the Doctor of Philosophy degree in Geological Sciences from The University of Maine in December, 2003.